Integrated Fiber Grating Couplers in Silicon Photonics

vorgelegt von
Dipl.-Ing.
Benjamin Wohlfeil
geboren in Berlin

von der Fakultät IV - Elektrotechnik und Informatik
der Technischen Universität Berlin
zur Erlangung des akademischen Grades

Doktor der Ingenieurwissenschaften
- Dr.-Ing. -

genehmigte Dissertation

Promotionsausschuss:

Vorsitzender:	Prof. Dr.-Ing. Wolfgang Heinrich
Gutachter:	Prof. Dr.-Ing. Klaus Petermann
Gutachter:	Prof. Dr.-Ing. Manfred Berroth
Gutachter:	Prof. Dr.-Ing. Rolf Schuhmann

Tag der wissenschaftlichen Aussprache: 30. März 2015

Berlin 2015

Contents

Introduction

With the ever increasing demand in bandwidth driven by new applications and by an increase in computational capability, that is dependent on high data rates, electronic communication devices are becoming increasingly insufficient to handle large loads. Solutions based on optics offer the necessary bandwidth, that is required to handle massive amounts of data and are already commonly used for long distance applications such as fiber optic submarine or metropolitan networks down to rack to rack interconnects employed in high performance computing systems. However, for a continuation of Moore's Law even higher data rates and optical communication on a much shorter distance - in particular on-chip - is required to provide for the increasing performance. Silicon photonics is a prime candidate to bring the advantages of optical communication to chip level and thus enabling dense integration of optical devices, that is also necessary for multi-channel transceiver systems with advanced modulation formats. Especially the Silicon on Insulator (SOI) platform has moved to the focus of much research in recent years [1], as silicon exhibits excellent optical properties in the near-infrared spectrum for this purpose and the technology capitalizes from mature processes developed by the integrated electronics industry. Co-integrating photonic devices with integrated circuits gives rise to novel optical interconnects and other applications, that can be easily and economically mass-fabricated, for systems in years to come.

The possibility of hybrid integration makes up for the shortcomings of silicon, when it comes to active devices. Since silicon itself is a very inefficient light source, devices made from other materials - mostly III-V semiconductors such as GaAs and InP - are employed and integrated with the SOI platform. For the detection of light photo-diodes made from germanium, which does exhibit absorption in the wavelength region, where silicon is transparent, offer great integrability, as being in the same group of the periodic system as silicon, the two materials can be grown on each other without a large mismatch between their crystal lattices.

The properties of silicon have been subject to extensive investigation, rendering it to one of the world's best known elements. Being an abundant material (approximately 14% of the earth's crust is silicon) and easily accessible together with the mature processes developed by the integrated electronics industry allows for cheap and reliable mass production of complex devices based on this material system. Its high refractive index qualifies it as a basis for dense integration of optical devices, however, at the cost of easy interfacing with external components: Silicon waveguides exhibit a large phase mismatch with low index contrast waveguides such as silica fibers, that are used in optical communication links everywhere. Additionally, their small size of only a few hundred nanometers compared to the large diameter of a silica fiber core results in a low field overlap between the guided modes in each waveguide resulting in difficult and very inefficient fiber chip coupling. The scope of

this thesis is to examine this problem and offer solutions to fiber chip coupling based on grating couplers. Existing designs are examined and improved upon and completely new grating layouts are offered for very high efficiency fiber chip interfaces. In addition a novel approach to exciting higher order fiber modes will be presented as well as a device for polarization conversion, all based on the SOI platform and compatible to existing technology.

The thesis is organized in the following way: First the problem of fiber chip coupling is outlined in more detail. Chapter 2 portrays the theoretical background used for the description of gratings in general and shows numerical methods employed for the simulation of devices analyzed, followed by a illustration of the fabrication and measurement outfit used for the realization characterization of the structures presented. Chapter 4 focuses on one dimensional grating couplers, while chapter 5 shows two dimensional grating couplers, that in contrast to one dimensional gratings inherently treat both polarization states. The last device presented is a novel way of coupling several higher order fiber modes between a few mode fiber and integrated waveguides.

Chapter 1

Fiber-Chip Coupling

Driven by the prospect of dense integration of photonic components and co-integration with electronic circuits, miniaturization of photonic integrated circuits (PICs) has been the focus of much research in recent years. Due to its high refractive index contrast the Silicon on Insulator (SOI) material system allows for the realization of optical devices, which are only a few wavelengths in size. Over the years, waveguides have shrunk from $10\mu m$ in height down to only 220nm. This drastic down scaling however brought several disadvantages with it: In addition to higher losses, higher polarization dependency and the need for more sophisticated fabrication technology, interfacing waveguides with the external world became increasingly difficult. To illustrate this problem, this chapter gives a short description of guided modes in dielectric waveguides such as optical fibers and photonic integrated waveguides and an overview over the available coupling schemes between these two waveguide types is presented in the second section of this chapter.

1.1 Waveguides & Materials

The waveguides and consequently all other devices used in this work are all based on the Silicon-On-Insulator (SOI) platform, which is commonly used on a large scale for integrated electronics and is very well suited for optical applications in the near infra red region due to its high index contrast and low absorption. A thin silicon layer is placed on an insulating SiO_2 layer (buried oxide or BOX for short), which provides optical and electrical insulation from the silicon substrate of several hundred

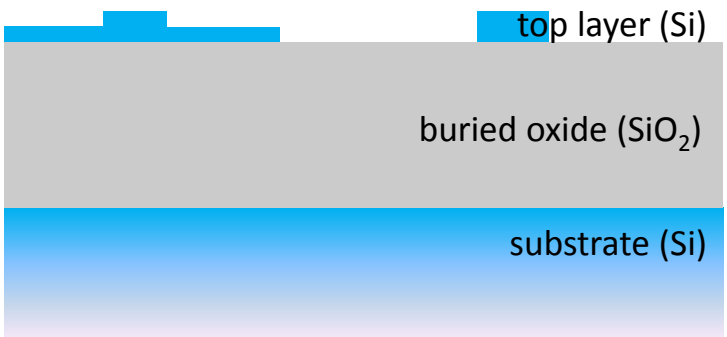

Figure 1.1: SOI layer stack with a rib waveguide (left) and a bulk waveguide (right) and air cladding.

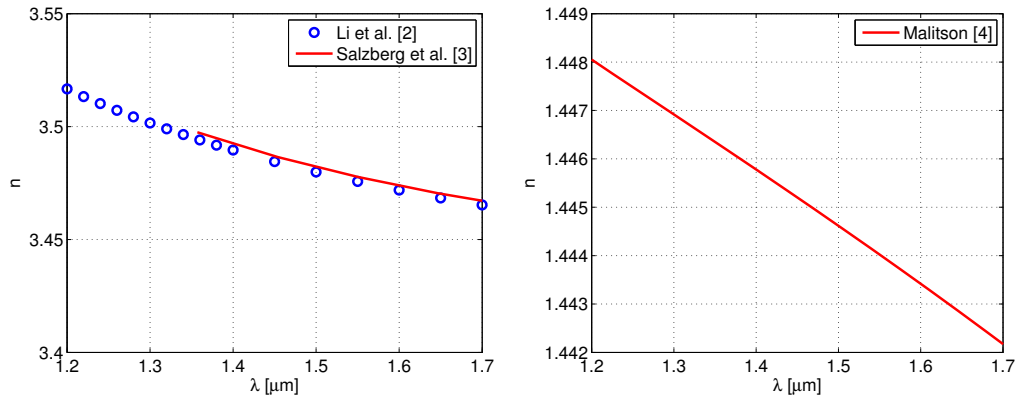

Figure 1.2: Refractive indices of mono crystalline silicon after [2, 3] (left) and silica glass (SiO_2) after [4] (right).

micron thickness. By processing of the top silicon layer (see chapter 3.1) waveguide structures as shown in figure 1.1 are obtained. If the top silicon layer is fully etched, bulk waveguides or wires are obtained, while in the case of partial etching a silicon slab region remains constituting a rib waveguide. The high refractive index of silicon ($n_{Si} \approx 3.47$ at $\lambda = 1.55\mu m$, see figure 1.2 (left)) compared to that of the buried oxide ($n_{SiO2} \approx 1.44$, see figure 1.2 (right)) and the surrounding cladding material, which is either air or again SiO_2 yields an excellent confinement of guided waves even in small waveguides. In the wavelength region used in this thesis (from $1.3\mu m$ to $1.6\mu m$) both materials may be regarded as completely lossless. SOI waveguides with losses as low as 0.1dB/cm have been demonstrated on large $4\mu m$ silicon substrates [5]. However, the SOI stack used for the devices shown here is much smaller. The top layer, in which the devices are etched, has a height of only 220nm. In contrast to thicker silicon layers, where single mode waveguide are practically only achievable through the use of rib waveguides, this allows for single mode waveguides made from bulk material. However, rib waveguides are still used on this scale to reduce losses caused by surface roughness at the etched edges of the waveguide. Since bulk waveguides (i.e. nano wires) are etched by their full height, their exposed surface is much larger than that of rib waveguides, which are shallowly etched by only a fraction of their height. Both waveguide types can be seen in figure 1.1.

The fields inside such waveguides satisfy the Helmholtz equation

$$\Delta_t \vec{E} + (k_0^2 n^2 - \beta^2)\vec{E} = 0. \tag{1.1}$$

It is implicitly assumed, that the structure is invariant along the z-axis and fields are time harmonic. Thus the ansatz

$$\vec{E}_m(x, y, z, t) = \vec{E}(x, y)e^{i\omega t - i\beta z} \tag{1.2}$$

describes the field of a mode inside the waveguide, where β is the phase constant of each mode. Δ_t in equation 1.1 is the transverse Laplace operator $\Delta_t = (\frac{\partial^2}{\partial x^2} + \frac{\partial^2}{\partial y^2})$ and $k_0 = \frac{2\pi}{\lambda}$ is the free space wavenumber.

Solutions to equation 1.1 for an optical fiber and integrated SOI waveguides of different size are illustrated to scale in figure 1.3. The modes of the integrated waveguide are labeled TE_{xy} and TM_{xy} modes depending on their polarization, where the subscript xy are the zero based counts of the intensity maxima in x- and y-direction of the respected modes. Although the actual waveguide modes exhibit

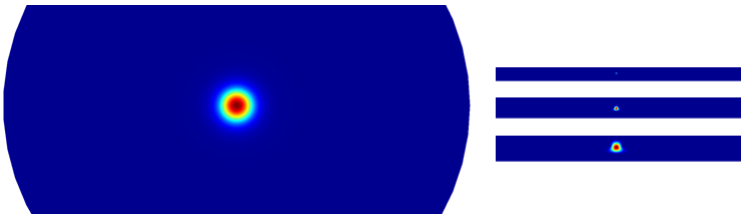

Figure 1.3: Electric field intensities of fundamental waveguide modes in a standard single mode fiber (left) and integrated waveguides (right) at $\lambda = 1.55\mu m$. Top: Nano wire (500nm x 220nm), middle: rib waveguide ($1.5\mu m$ x $1.5\mu m$, 750nm etch depth), bottom: rib waveguide ($3.5\mu m$ x $4\mu m$, $2\mu m$ etch depth).

both electric and magnetic field components in propagation direction, the TE or TM field components are carrying the predominant fraction of power. Therefore the TE/TM approximation is a valid classification. The depicted modes of figure 1.3 are therefore all TE_{00} modes, which are the most commonly used ones in this work. In chapter 5.3 the first higher order TE_{10} mode also becomes of importance.

In fibers most commonly the linearly polarized ($LP_{\phi r}$) modes are used, where the indices ϕ and r describe the order of the mode in angular and radial direction, respectively. These indices are not zero based and therefore the fundamental fiber mode is labeled LP_{01}.

1.2 Coupling Schemes

Coupling between a fiber and an integrated waveguide is a challenging task due to their vastly different sizes and phase constants of their modes. The scope of the problem is illustrated in figure 1.4, where the cross sections of the electric fields of the modes shown in figure 1.3 in SOI waveguides of varying size and that of a standard single mode fiber (sSMF) are shown. It is evident, that the smaller the

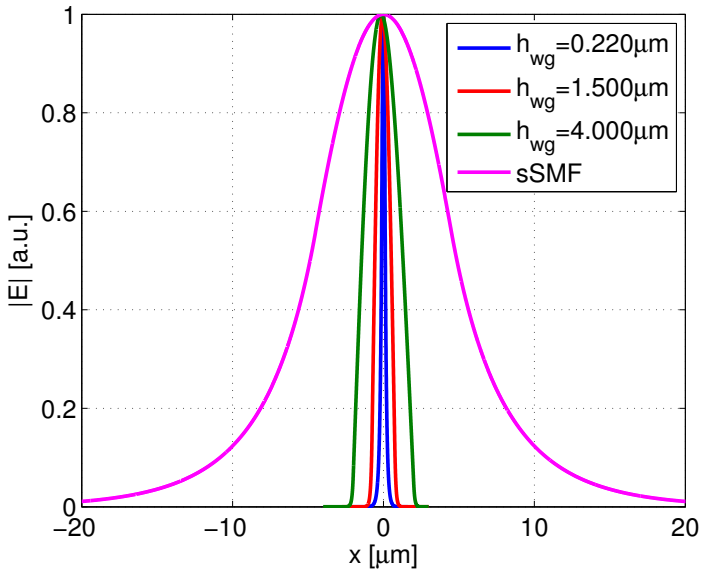

Figure 1.4: Cross sections of the electric field distribution in integrated waveguides of varying size (c.f. figure 1.3) and a sSMF at $\lambda = 1.55\mu m$.

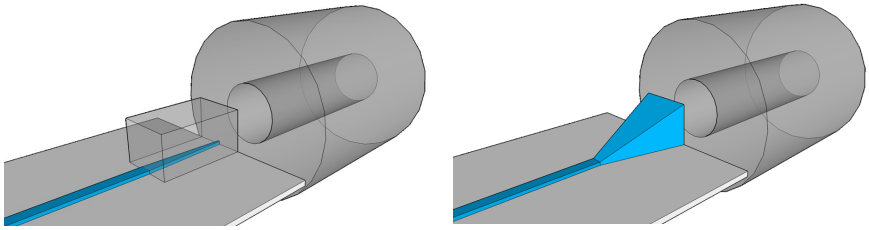

Figure 1.5: Taper structures for fiber chip interfacing. Left: Inverted taper with polymer waveguide. Right: 3d taper structure.

integrated waveguide is, the larger the mismatch between the fields of that waveguide and that of the fiber. In terms of loss, this mismatch can amount to less than -20dB coupling efficiency (in case of nanowires of 500nm x 220nm cross section), when the two waveguides are butt-coupled. For transmission systems with high data rates this value is fatal, as it severely impacts the signal to noise ratio and therefore the bit error rate of the transmission.

For this reason more elaborate coupling schemes were developed, that yield higher coupling efficiencies. The most straight forward solution to small waveguide dimensions is a tapering to larger cross sections (see figure 1.5). However, to be fully effective, in addition to a planar tapering, which can be realized with ease, an increase in waveguide height is required as well. In [6, 7] vertical, monolithically integrated silicon tapers were demonstrated, that yielded up to 60% (80% theoretical performance) coupling efficiency with a $10\mu m$ x $10\mu m$ waveguide facet. However, due to the fabrication process involving gray-scale masks, the device can not be fabricated with CMOS compatibility.

Inverted tapers, as first used for coupling from lasers to optical fibers [8], also achieve an increase in spot size of the optical mode. By decreasing the dimensions of the integrated waveguide, confinement of the mode is drastically reduced, resulting in a high overlap with the fiber mode. An increase in coupling efficiency compared to butt-coupling was demonstrated [9] and through the use of a polymer cladding (c.f. figure 1.5 (left)) an efficiency of just below 50% was shown [10]. Due to the extreme change in mode size required for an efficient coupling, the resulting structures can become unreasonably large. In [11] a lensed fiber was used for coupling, reducing the cladding size of the inverted taper from approximately $10\mu m$ x $10\mu m$ to only $2\mu m$ x $2\mu m$. -0.7dB coupling efficiency was achieved in [12] with a SiO_2 cladding and a two etch process. Nonetheless, adding an additional material to the process increases cost and potentially impedes CMOS compatibility. Additionally problematic is the small cross section on the tip of the inverted taper, which is usually well below 100nm in width and therefore not necessarily within reach of every fabrication technology.

A more elaborate approach was demonstrated in [13], where light was coupled to a larger cross section and lower index contrast SiON waveguide on top of the silicon waveguide by means of evanescent coupling. Since the phase mismatch between the silicon waveguide and the SiON waveguide, that is subsequently butt coupled to the fiber, is very large, a grating is employed, which reduces the phase mismatch between waveguides. However, due to the vastly different waveguides in use, this approach has to be carried out in two stages with an intermediate Si_3N_4 waveguide between them. Experiments on the Dual-Grating Assisted Directional Coupler [14] show a peak coupling efficiency of 55%, however, due to strong wavelength dependency of

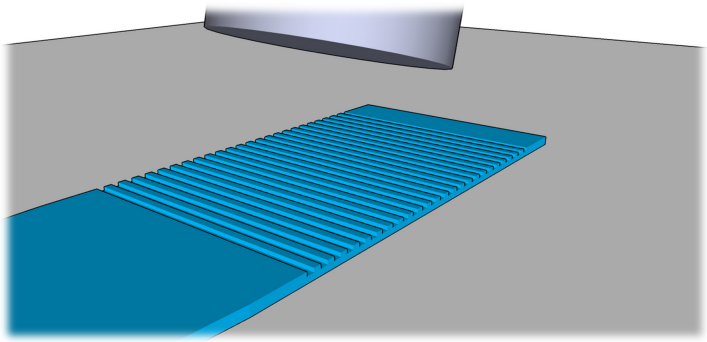

Figure 1.6: Fiber grating coupler.

asymmetric directional couplers and gratings, the bandwidth of the device amounts to only 4nm, which is a drastic reduction compared to taper based approaches, which typically exhibit bandwidths of more than 100nm.

Although compatible to established packaging technology, the common drawback of all edge based approaches is the need for a processed facet, at which fiber chip interfacing takes place. The nature of this coupling scheme demands the tapers to be positioned at the edges of the chip, where a flat surface has to be provided. For this reason each edge of the chip, where coupling takes place, has to be ground to remove material and bring the coupling device as close as possible to the chip's border and polished to decrease surface roughness.

A more elegant solution, that does not require additional processing of surfaces at edges, is the grating coupler (see figure 1.6). In contrast to other coupling devices, the grating coupler may be placed anywhere on the chip as it diffracts light in vertical direction rather than horizontal and is therefore not bound to edges. The additional process steps of grinding and polishing are not necessary and PICs can even be tested before separation of chips from the wafer.

Through periodic etches on the waveguide's surface light is diffracted in nearly vertical direction, where constructive interference of field scattered at each grating period resembles the field distribution of the fundamental fiber mode, resulting in a high coupling efficiency between integrated waveguide and optical fiber. The drawback of this approach is limited bandwidth, as the angle at which the diffracted field propagates is highly dependent on the wavelength. Early grating couplers were very long [15, 16], exhibiting indeed low bandwidths and large spot sizes of the diffracted fields. Thus additional lenses were used for coupling to a fiber. Shorter grating couplers as used today [17] do not have the need of additional lenses and show -1dB-bandwidths of well above 20nm [18].

Besides having a sufficient bandwidth, the coupling efficiency is the primary concern when designing a fiber grating coupler. So far, the best performing devices make use of a reflecting layer (either metal or a dielectric Bragg layers) placed under the buried oxide of the SOI stack [19], which yield a coupling efficiency of up to -0.6dB, as demonstrated in [20]. However, this approach requires additional processing, since the reflecting layers are accessed through the backside of the substrate, rendering this method cost intensive, though unparalleled in performance.

A different approach to increasing efficiency is the use of a poly-silicon overlay on top of the grating region of the top silicon layer [21]. This method requires only one additional process step and can be implemented inexpensively. However, the benefit

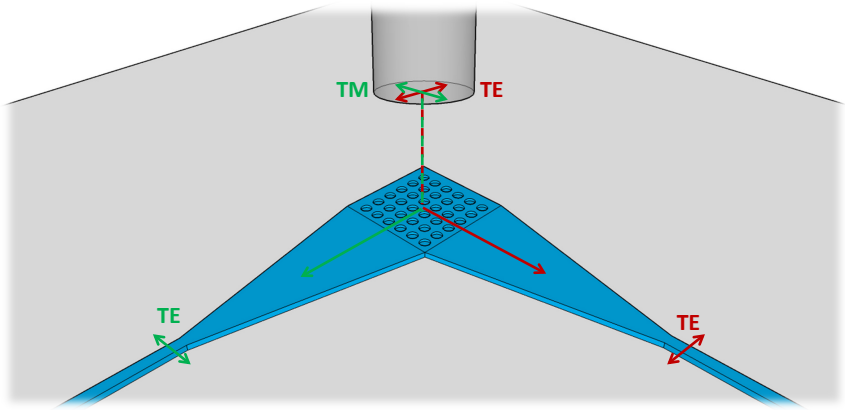

Figure 1.7: Two dimensional fiber grating coupler.

over standard gratings is not as large as it is the case for grating couplers with bottom reflectors. Both methods may be used in combination with chirp or apodization to increase the field overlap with the fiber mode [22]. Additional improvements can be achieved by means of a rear reflector or a blazing of the grating etches [23].

In contrast to most etch based coupling approaches, grating couplers show a large polarization dependency. For this reason, only light of one polarization is reasonably well coupled between the integrated waveguide and the fiber using grating couplers. TE polarized light shows better performance in the SOI substrate used and has properties better suited for coupling using grating couplers. However, since modern fiber optic transmission systems utilize both polarization states, coupling of both polarizations has to be made available through a single device. In [24] a two dimensional grating coupler was demonstrated, that couples TE as well as TM polarized light from the fiber to the TE polarization of two different integrated waveguides, therefore acting as a polarization splitter and converter at the same time (see figure 1.7).

Here, improvements similar to the ones made for the one dimensional grating couplers can be conducted, although to a lesser extent. The orthogonal alignment of the integrated waveguides to the grating prohibits an effective apodization or chirp of the grating etches. Additionally, bottom reflectors and overlay layers are less effective since scattering loss to the substrate plays a less significant role compared to one dimensional grating couplers. Exact performance values are hard to find in the literature, but first investigations of such structures revealed a coupling efficiency of 23% [23] (without any enhancement measures). In more recent work coupling efficiencies of -1dB and -2dB were claimed [25] for 2D gratings with and without bottom reflector, respectively.

Gratings for special purposes have been developed as well: Focusing gratings, that reduce the required taper length for the mode conversion between grating and waveguide, thus reducing the footprint of the coupler, have been shown [26]. Coupling to fiber modes other than LP_{01} was conducted through the use of grating couplers by different means [27, 28, 29, 30]. And a different approach to the polarization splitting grating was illustrated in [31], where the TM polarization was maintained.

In this thesis an extensive numerical investigation of one and two dimensional fiber grating couplers was conducted. Starting with simple one dimensional grat-

ings adapted for operation at a wavelength of $\lambda = 1.31\mu m$, gratings for $\lambda = 1.55\mu m$ are improved stepwise by identifying and eliminating sources of loss. First a silicon overlay is used to improve the fraction of out-coupled power, while maintaining a low scattering angle. In contrast to other devices this layer is mono-crystalline and the whole grating is fully compatible to IHP's BiCMOS manufacturing line. Further improvement is achieved by adding a secondary etch step to the grating, which improves overlap with the fiber mode similarly to chirped gratings known from the literature, but maintains regularity along the grating. Lastly, a heuristic optimization approach is used to explore optimal grating designs, leading to novel grating layouts with extremely low losses. Additionally, this approach surprisingly indicates inversely chirped gratings to be superior to regularly chirped ones. Similarly, two dimensional gratings are designed for IHP's manufacturing line and a novel device for the excitation and detection of higher order fiber modes is presented.

Chapter 2

Theory

In this chapter an overview over the theory of diffraction gratings will be given. Early work on this topic was closely related to spectroscopy and therefore much of the theory of gratings is focused on that subject. A brief look into the history of the development in this area shows, that a great deal of effort was put into the development of highly dispersive gratings for commercial applications. Since efficiency was only - if at all - a secondary consideration, analytical descriptions of diffraction gratings lack models for their performance. In other words, with current theories one could predict, where light of a certain wavelength would scatter, when diffracted by a grating but not how much of it. Therefore numerical solutions to this problem need to be employed, which the majority of results in this thesis are calculated with. The most common electromagnetic field simulation methods relevant for this field will be outlined here.

2.1 Gratings and Spectroscopy

2.1.1 The Grating Equation

An intuitive description of the diffraction of an incoming wave by a grating is given by the grating equation (or Bragg condition). Consider a setup as in figure 2.1. A plane wave is incident on the grating under the angle φ_0. The path difference between the diffracted beams of light can be derived through geometrical observation as

$$n_1 b - n_0 a = \Lambda n_1 \sin(\varphi) - \Lambda n_0 \sin(\varphi_0). \tag{2.1}$$

To achieve constructive interference in the scattered field it is again necessary, that light diffracted from two neighboring grating periods is in phase. This is the case when the path difference given in 2.1 is equal to the wavelength λ or integral multiples of it. Substituting this condition into equation 2.1 leads to

$$\Lambda(n_1 \sin(\varphi) - n_0 \sin(\varphi_0)) = m\lambda, \quad m = 0, \pm 1, \pm 2, \pm 3, \ldots \tag{2.2}$$

If this condition is not met, there will be destructive interference at the angle φ. Condition 2.2 is known as the grating equation and may also be derived by means of Fraunhofer diffraction [32]. m is being called the diffraction order or the grating order, when used in the a context with fixed wavelength and angles φ_0 and φ. The order $m = 0$ denotes the specular order since in the case of reflection the grating

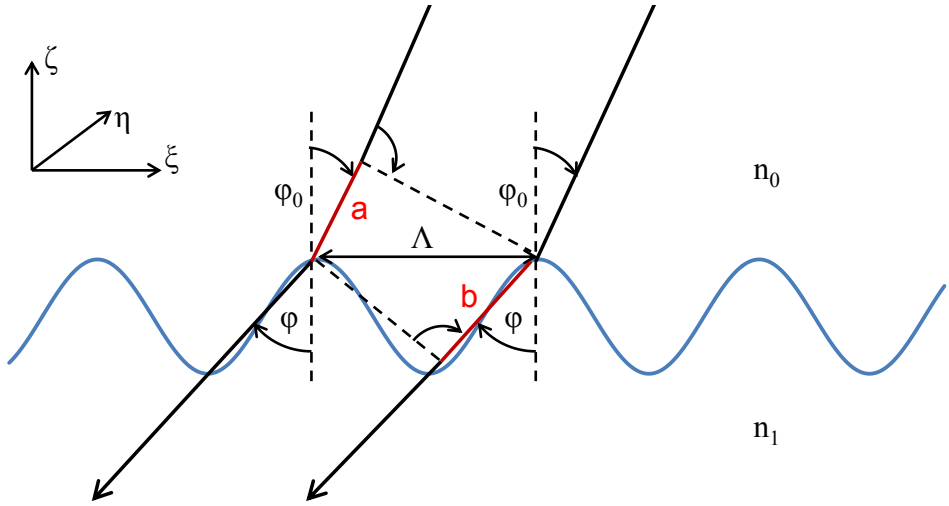

Figure 2.1: Illustration of the optical path difference in from neighboring grooves diffracted light.

behaves just like a mirror [33] with $\varphi = \varphi_0$. For all other diffraction orders the angle of diffraction φ is dependent on the wavelength. Therefore, the grating acts as a prism, separating wavelengths angularly, albeit with a much larger effect. This property is what made gratings initially attractive for spectroscopy. In the case of fiber grating couplers on the other hand the strong dependence of the scattering angle on wavelength is the main limiting factor when it comes to bandwidth.

A more general representation of equation 2.2 can be denoted using the wave vectors $\vec{k}$ of incident and diffracted light. Using the coordinate system defined in figure 2.1 yields

$$\begin{aligned} k_\xi &= k_{0,\xi} + m\frac{2\pi}{\Lambda} \\ k_\eta &= k_{0,\eta}, \end{aligned} \tag{2.3}$$

when the grating lies along the ξ-axis. k_0 and k denote the wave vector components of the incoming and diffracted fields, respectively. Sometimes the term $K = \frac{2\pi}{\Lambda}$ is used and is called the grating vector. Since the absolute of the wave vector $|\vec{k}| = n\frac{2\pi}{\lambda}$, where n is the refractive index of the cladding material on either side of the grating, this representation of the grating equation takes the environment into account. Each component of $\vec{k}$ can be expressed in terms of angle of incidence or refraction respectively by substituting $k_\xi = n\frac{2\pi}{\lambda}\sin(\varphi)$. Therefore it is easy to see that equations 2.2 and 2.3 are equivalent.

It can be seen, that equations 2.2 and 2.3 are only true if

$$-1 \leq \sin(\varphi) \leq 1. \tag{2.4}$$

If a grating order m can be found, for which this condition is satisfied, then this order is called a propagating order. The wave vector associated with it describes a regularly propagating plane wave, since

$$|k|^2 = k_\xi^2 + k_\zeta^2 = n^2(\frac{2\pi}{\lambda})^2. \tag{2.5}$$

Therefore the vertical component of $\vec{k}$ can be expressed as

$$k_\zeta = \sqrt{n^2(\frac{2\pi}{\lambda})^2 - k_\xi^2} = n\frac{2\pi}{\lambda}\sqrt{1-\sin(\varphi)^2} = n\frac{2\pi}{\lambda}\cos(\varphi), \tag{2.6}$$

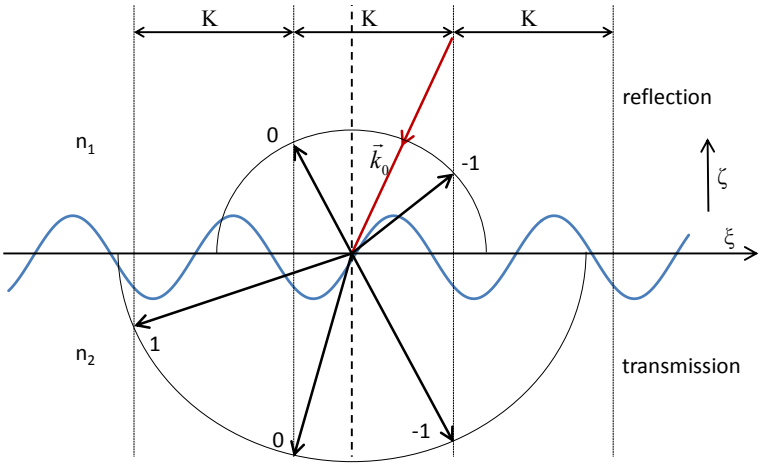

Figure 2.2: Illustration of the grating equation.

which gives rise to a plane wave propagating along the direction of $\vec{k}$. If on the other hand condition 2.4 is not met, the vertical component $\vec{k}$ becomes imaginary and the amplitude of the diffracted wave decreases along the ζ-direction by a factor of

$$\exp(-i\,\vec{k}\vec{r}) = \exp(-k_\zeta \zeta)\exp(-i\,k_\xi \xi). \tag{2.7}$$

These orders are called evanescent orders and must be taken into consideration for a complete theory on gratings. A graphical representation of equation 2.3 can be seen in figure 2.2. In agreement with the earlier convention the specular order is denoted with $m = 0$. The other order reachable in the reflection spectrum is displaced by $-1 \cdot K$ in the ξ-direction with respect to the zero order and therefore carries the order $m = -1$. The resulting wave vectors are located on a half circle, as demanded by equation 2.5. In the transmission spectrum an additional order is obtained through a higher refractive index in the substrate of the grating. Again the distance between zero order and first order diffraction is K and the diffraction order of it is $m = 1$. All other orders can not be reached through the wave vector of the incoming field and are therefore evanescent. For very long periods K becomes zero and naturally the diffraction orders vanish with the exception of the 0th order, in which case equation 2.3 reduces to Snell's law of refraction.

A special case in the grating equation occurs if the incident field is aligned with the ξ-axis (c.f. figures 2.1 and 2.2) and is a guided mode. The wave vector $\vec{k_0}$ has only a single component pointing in the ξ-direction and is expressed in terms of the effective refractive index n_{eff} of the guided mode. The grating equation is then written as

$$k_\xi = \beta + mK \tag{2.8}$$

with

$$\beta = n_{eff}\frac{2\pi}{\lambda} \tag{2.9}$$

being the phase constant of the waveguide mode. For weaker gratings this expression holds true since the effective refractive indices of guided modes in an unimpaired waveguide and in one with a grating present are nearly equal. But for strong gratings this is no longer the case. One could estimate the overall effective refractive index in a waveguide with a strong grating by determining the geometrical average of n_{eff} in one period at every point along the propagation direction (here ξ-direction).

However, this method would disregard reflections at interfaces between or within periods and therefore resonance effects, which could affect n_{eff}. Therefore, it is necessary to obtain the phase velocity of the mode in a perturbed waveguide by other means - mostly numerically.

The convention for naming the diffraction orders is not consistent in the literature. Usually, perfectly vertical diffraction is associated with the order $m = \pm 2$, while reflection back into the waveguide is denoted as the 0th diffraction order. The waveguide grating coupler for nearly vertical diffraction is therefore denoted with $m = \pm 1$, which is the preferred case for fiber grating couplers.

A rough estimation of the bandwidth of a waveguide grating can be already made using equation 2.8 by relating a change in wavelength to the change in diffraction angle φ as was shown in [34] and further elaborated in [18].

2.2 Numerical Description

In the previous section an analytical description of diffraction gratings was presented. As noted, in the general case this method is by itself insufficient when it comes to the characterization of gratings. The grating equation 2.8 can be used to predict diffraction angles of waveguide gratings as a function of wavelength but it relies on the numerical input in form of the effective refractive index of the waveguide mode in the grating structure. In addition to this problem, nowhere in the analytical description is one of the most important values touched upon - diffraction efficiency. For a theoretical description of gratings numerical methods, which are capable of producing those figures of merit, that are not available through analytical means, are of utmost importance. Therefore, in this chapter a brief outline of the numerical methods available for the simulation of fiber grating couplers is presented. Since numerical methods tend to cover broader areas than single types of structures, the use of these methods is not limited to diffraction gratings and are therefore used for the investigation of other devices throughout this thesis as well.

2.2.1 Finite-Difference Time-Domain Method

Early development on the finite-difference time-domain (FDTD) method was largely driven by military applications [35]. Next to asymptotic methods [36, 37] and integral methods as the Method of Moments [38, 39], the FDTD method was one of the earliest numerical methods of solving Maxwell's equations. Being more general than other methods at the time it soon became the method of choice for many applications. The nature of problems much research was focused on such as radar and electromagnetic pulses also strongly favored the FDTD method as it directly operates in time domain.

The basic method was first laid out by K. Yee in 1966 [40] and adapted by A. Taflove [41]. It is designed to solve Maxwell's curl equations on a spatial (and temporal) grid, thus requiring a discretization of the computational domain. As mentioned before, the FDTD method is very general. Therefore, at its basis a very

general formulation of the Maxwell equations can be found:

$$\frac{\partial \vec{H}}{\partial t} = -\frac{1}{\mu}\nabla \times \vec{E} - \frac{1}{\mu}(\vec{M}_s + \sigma_h \vec{H}) \tag{2.10a}$$

$$\frac{\partial \vec{E}}{\partial t} = \frac{1}{\epsilon}\nabla \times \vec{H} - \frac{1}{\epsilon}(\vec{J}_s + \sigma_e \vec{E}). \tag{2.10b}$$

The vectors $\vec{M}_s$ and $\vec{J}_s$ represent the sources of magnetic and electric field energy and are called the equivalent magnetic current density and electric current density, respectively; they carry the units $\frac{V}{m^2}$ and $\frac{A}{m^2}$. σ_e and σ_h are the electric and magnetic conductivities.

Expanding the curl operator in Cartesian coordinates of equations 2.10 yields

$$\frac{\partial H_x}{\partial t} = \frac{1}{\mu}[\frac{\partial E_y}{\partial z} - \frac{\partial E_z}{\partial y} - (M_{s,x} + \sigma_h H_x)] \tag{2.11a}$$

$$\frac{\partial H_y}{\partial t} = \frac{1}{\mu}[\frac{\partial E_z}{\partial x} - \frac{\partial E_x}{\partial z} - (M_{s,y} + \sigma_h H_y)] \tag{2.11b}$$

$$\frac{\partial H_z}{\partial t} = \frac{1}{\mu}[\frac{\partial E_x}{\partial y} - \frac{\partial E_y}{\partial x} - (M_{s,z} + \sigma_h H_z)] \tag{2.11c}$$

$$\frac{\partial E_x}{\partial t} = \frac{1}{\epsilon}[\frac{\partial H_z}{\partial y} - \frac{\partial H_y}{\partial z} - (J_{s,x} + \sigma_e E_x)] \tag{2.12a}$$

$$\frac{\partial E_y}{\partial t} = \frac{1}{\epsilon}[\frac{\partial H_x}{\partial z} - \frac{\partial H_z}{\partial x} - (J_{s,y} + \sigma_e E_y)] \tag{2.12b}$$

$$\frac{\partial E_z}{\partial t} = \frac{1}{\epsilon}[\frac{\partial H_y}{\partial x} - \frac{\partial H_x}{\partial y} - (J_{s,z} + \sigma_e E_z)]. \tag{2.12c}$$

Equations 2.11 and 2.12 are the general three dimensional basis of the FDTD algorithm. For many problems however, a simplification can be assumed by reducing the problem to two dimensions. If geometry and sources do not change along one direction (e.g. z-direction), the spatial derivatives are zero and the six coupled differential equations can be grouped so that no field components of the first group appear in the second. It can be seen, that this is the case, when equations 2.11a, 2.11b and 2.12c are in the first group (TM group) and 2.11c, 2.12a and 2.12b are in the second (TE group), if the problem is invariant along the z-direction. The groups are completely decoupled and any field in this geometry can be expressed as a linear superposition of solutions of the TE and TM group. As mentioned before, the FDTD method relies on decomposition of the computational domain into unit cells, which are sometimes referred to as pixels or voxels (short for volumetric pixel). A unit cell is depicted in figure 2.3. In contrast to most other methods, which solve for the electric or magnetic field alone, the FDTD method solves for both at the same time. Therefore, it is potentially more robust and applicable for a wider class of structures [35]. As illustrated, each field component of the electric field is centered within four positions, where the magnetic field components are located. Conversely, each magnetic field component is surrounded by four circulating locations of the electric field. That gives a clear analogy to the contour integrals for electric and magnetic induction. One can also see, that continuity of the tangential field components of both electric and magnetic fields is naturally maintained at material interfaces.

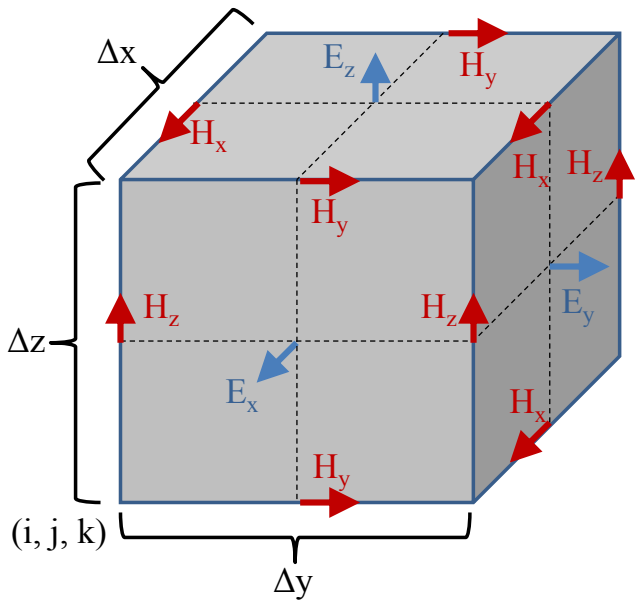

Figure 2.3: Illustration of the locations of electric and magnetic field components on a unit grid cell.

However, having field components located at non integral unit positions within the spatial grid also gives rise to a problem at material interfaces. Since it is not clear which material property needs to be assigned to a field component, some form of averaging needs to be performed. Although this has to be done only once and the computational effort to do so is not high, it can result in an unexpectedly high memory usage limiting the size of the computational domain.

Analogously to the decomposition of the spatial dimensions into unit cells, time is discretized similarly. The method used is called leapfrog arrangement, where at each full time step the electric field is computed and at every half time step the magnetic field. At every point in space the electric field is stored in memory and used to compute the magnetic field of the following half time step and after that the newly obtained magnetic field is the basis for the calculation of the electric field for next full time step. This cycle continues until termination is reached. By this method problems caused by the simultaneous calculation of electric and magnetic field are avoided. Figure 2.4 illustrates the leapfrog arrangement for a one dimensional space grid.

With the environment in space and time set, it is now possible to adapt equations 2.11 and 2.12. First, it is common to describe the position of each unit cell with multiples of its dimensions. Usually a unit cell is cubic (although other anisotropic forms can be used) and therefore its location is denoted as $(i\Delta x, j\Delta y, k\Delta z)$ or (i, j, k) for short (c.f. figure 2.3). Similarly, a point in time is expressed as $n\Delta t$ or simply n. The x-component of the electric field in a unit cell is therefore represented as $E_x(i, j + 0.5, k + 0.5, n)$. The derivatives in Yee's algorithm are calculated by the difference quotient [40]. This is easily implemented and numerically inexpensive, however, it results in an error of second order.

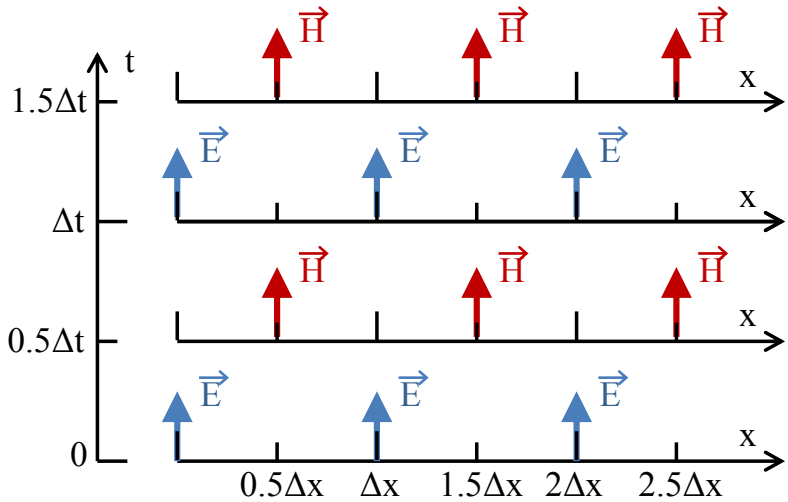

Figure 2.4: Illustration of the leapfrog arrangement in a one dimensional FDTD grid.

Equation 2.12a is thus expressed as

$$\begin{aligned}\frac{E_x|^{n+0.5}_{i,j+0.5,k+0.5} - E_x|^{n-0.5}_{i,j+0.5,k+0.5}}{\Delta t} &= \frac{1}{\epsilon_{i,j+0.5,k+0.5}} \cdot \\ &\Big(\frac{H_z|^{n}_{i,j+1,k+0.5} - H_z|^{n}_{i,j,k+0.5}}{\Delta y} - \frac{H_y|^{n}_{i,j+0.5,k+1} - H_y|^{n}_{i,j+0.5,k}}{\Delta z} \\ &- J_{s,x}|^{n}_{i,j+0.5,k+0.5} - \sigma_{i,j+0.5,k+0.5} E_x|^{n}_{i,j+0.5k+0.5}\Big),\end{aligned} \tag{2.13}$$

where the temporal dependency is denoted in the superscript of each field component and the spatial location in the subscript. On the left hand side of equation 2.13 a field component of time step $n + 0.5$ is present, whereas on the right hand side all fields are denoted with time step n. Since the fields from time step $t \geq n$ are unknown at this point, they have to be obtained through estimation. It is assumed that a field at time step n is the arithmetic average of its half time step predecessor and successor

$$U_c|^{n}_{i,j,k} = \frac{U_c|^{n+0.5}_{i,j,k} + U_c|^{n-0.5}_{i,j,k}}{2}, \tag{2.14}$$

where U_c is either component c of the electric or magnetic field. Applying this assumption to equation 2.13 yields

$$\begin{aligned}\frac{E_x|^{n+0.5}_{i,j+0.5,k+0.5} - E_x|^{n-0.5}_{i,j+0.5,k+0.5}}{\Delta t} &= \frac{1}{\epsilon_{i,j+0.5,k+0.5}} \cdot \\ &\Big(\frac{H_z|^{n}_{i,j+1,k+0.5} - H_z|^{n}_{i,j,k+0.5}}{\Delta y} - \frac{H_y|^{n}_{i,j+0.5,k+1} - H_y|^{n}_{i,j+0.5,k}}{\Delta z} \\ &- J_{s,x}|^{n}_{i,j+0.5,k+0.5} - \sigma_{i,j+0.5,k+0.5} \cdot \frac{E_x|^{n+0.5}_{i,j+0.5,k+0.5} + E_x|^{n-0.5}_{i,j+0.5,k+0.5}}{2}\Big).\end{aligned} \tag{2.15}$$

Now $E_x|^{n+0.5}_{i,j+0.5,k+0.5}$ can be isolated:

$$E_x|^{n+0.5}_{i,j+0.5,k+0.5} = \frac{1-\frac{\Delta t\sigma_{i,j+0.5,k+0.5}}{2\epsilon_{i,j+0.5,k+0.5}}}{1+\frac{\Delta t\sigma_{i,j+0.5,k+0.5}}{2\epsilon_{i,j+0.5,k+0.5}}} E_x|^{n-0.5}_{i,j+0.5,k+0.5} + \frac{\frac{\Delta t}{\epsilon_{i,j+0.5,k+0.5}}}{1+\frac{\Delta t\sigma_{i,j+0.5,k+0.5}}{2\epsilon_{i,j+0.5,k+0.5}}} \cdot \left(\frac{H_z|^n_{i,j+1,k+0.5} - H_z|^n_{i,j,k+0.5}}{\Delta y} - \frac{H_y|^n_{i,j+0.5,k+1} - H_y|^n_{i,j+0.5,k}}{\Delta z} - J_{s,x}|^n_{i,j+0.5,k+0.5}\right). \tag{2.16}$$

Equally, the remaining electric and magnetic field components have to be isolated and expressed in terms similar to equation 2.16, but for brevity this is not done here. For a complete account of all field components, the reader may refer to [35]. It can be seen, that the x-component of the electric field at any position, which is not adjacent to sources, is only dependent on the x-component of the electric field from the previous time step and on the surrounding magnetic field components H_y and H_z. The sources $\vec{J}_s$ and $\vec{M}_s$ are the time dependent inputs for the algorithm and are therefore known parameters, just like the material properties ϵ and σ.

One of the strengths of this method is related to parallel computing. The computational domain can be divided into smaller sub-domains of any number of unit cells, which can be computed by individual processors. Only values obtained at the interfaces between sub-domains need to be communicated to other processors, aggregating to a moderate amount of communication bandwidth. It is therefore evident that the FDTD method scales very well with problem size and as a consequence it is used with all kinds of computers ranging from normal desktops to huge clusters [42]. Even problems as big as the earth itself have been modeled [43], using alternative grids.

A number of optimizations to the implementation of the algorithm can be undertaken by specifying the problem to a less general form. For example having an exact cubic grid with $\Delta x = \Delta y = \Delta z$ saves a large amount of memory in the case of continuous material properties. Also a small amount of different non continuous, non permeable media ($\mu = \mu_0$) affects memory usage in a positive way. For specific geometries other unit cell shapes might prove to be favorable over the standard rectangular one. For details on optimization see [44, 45].

2.2.2 Eigenmode Expansion Method

The Eigenmode Expansion (EME) method or sometimes called the Mode Matching method differs somewhat from the FDTD or FEM approach, as it does not rely on a decomposition of the computational domain into spatial cells, but rather partitions with equal (or nearly equal) character along the axis of propagation. The electric or magnetic field in each partition is described in terms of modes rather than a summation of individual field points. Therefore, the size of the device simulated is not an indication of the computational cost. Structures that are easily out of reach of the FDTD and FEM methods can be handled by the Eigenmode Expansion method, as long as the number of modes necessary to describe the device is moderate. Therefore, devices best simulated using this method are straight, unchanging waveguides, which guide a low number of modes. However, such a device would not be simulated in the first place, since it is already fully described by the guided modes. The Eigenmode Expansion method is most commonly used to calculate the scattering matrix of interfacing structures. Figure 2.5 shows two different waveguides butt-coupled to

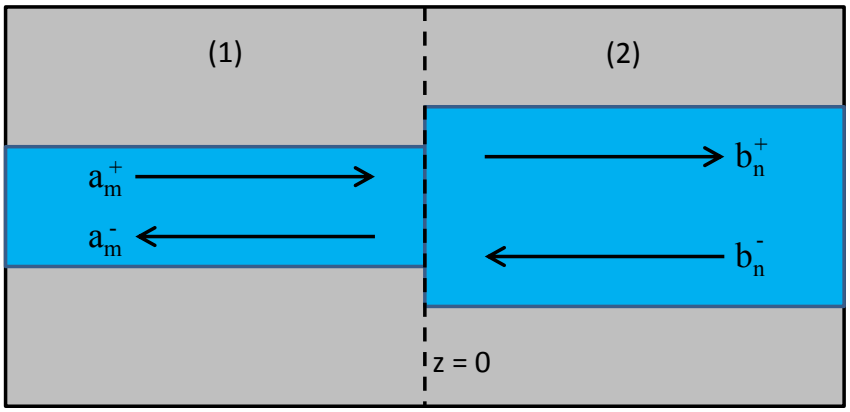

Figure 2.5: Mode coefficients in two waveguides interfacing.

each other. Since the waveguides are unequal, reflections at the interface and losses are to be expected.

The fields in each uniform waveguide part are described as a linear superposition of all guided and radiation modes [46]. If the z-axis is the direction of propagation the transverse electric and magnetic fields are

$$\vec{E}_t(x,y,z) = \sum_m^M (a_m^+ \exp(-i\,\beta_m z) + a_m^- \exp(i\,\beta_m z))\,\vec{E}_{t,m}(x,y) \text{ and} \tag{2.17a}$$

$$\vec{H}_t(x,y,z) = \sum_m^M (a_m^+ \exp(-i\,\beta_m z) - a_m^- \exp(i\,\beta_m z))\,\vec{H}_{t,m}(x,y), \tag{2.17b}$$

where a_m^+ and a_m^- are the amplitudes of the forward and backward propagating mode m. As usual the time dependent factor $\exp(i\,\omega t)$ is omitted. $\vec{E}_{t,m}$ and $\vec{H}_{t,m}$ are the transverse fields associated with the modal propagation constant β_m and are solutions of the Helmholtz equation 1.1. M is the combined number of guided and radiation modes. For a complete basis one would have to include all modes - a finite number of guided and an infinite number of radiation modes. In many cases however, a moderate amount of guided modes is sufficient to describe a device.

For straight lossless waveguides the amplitude of the backward propagating field might be neglected, but for a structure as illustrated in figure 2.5, where reflections are to be expected, it is very important. Maxwell's equations demand the x- and y-component of the electric and magnetic field to be continuous at interfaces. Therefore, the condition

$$\begin{aligned} &\sum_{m=1}^M (a_m^+ \exp(-i\,\beta_m z) - a_m^- \exp(i\,\beta_m z))\,\vec{E}_{t,m}(x,y) \\ &= \sum_{n=1}^N (b_n^+ \exp(-i\,\beta_n z) - b_n^- \exp(i\,\beta_n z))\,\vec{E}_{t,n}(x,y) \end{aligned} \tag{2.18}$$

has to be met at $z = 0$, where M is the number of modes on one side of the interface and N the number of modes on the other. If a single mode i from the left waveguide

(1) is incident on the interface, equation 2.18 can be simplified to

$$\begin{aligned}\vec{E}_{t,i}^{(1)}(x,y)\exp(-i\,\beta_i^{(1)}z) + \sum_{m=1}^{M} a_m^- \vec{E}_{t,m}^{(1)}(x,y)\exp(i\,\beta_m^{(1)}z) \\ = \sum_{n=1}^{N} b_n^+ \vec{E}_{t,n}^{(2)}(x,y)\exp(-i\,\beta_n^{(2)}z).\end{aligned} \tag{2.19}$$

For clarity, the superscript denotes the waveguide section: (1) for the partition at $z < 0$ and (2) for $z > 0$. Similarly, for the magnetic field the following expression has to be valid.

$$\begin{aligned}\vec{H}_{t,i}^{(1)}(x,y)\exp(-i\,\beta_i^{(1)}z) - \sum_{m=1}^{M} a_m^- \vec{H}_{t,m}^{(1)}(x,y)\exp(i\,\beta_m^{(1)}z) \\ = \sum_{n=1}^{N} b_n^+ \vec{H}_{t,n}^{(2)}(x,y)\exp(-i\,\beta_n^{(2)}z)\end{aligned} \tag{2.20}$$

Equations 2.19 and 2.20 yield the resulting fields traveling away from the joint in both waveguide parts as a function of the incident wave i. In general this is expressed as

$$\begin{bmatrix}\vec{a}^- \\ \vec{b}^+\end{bmatrix} = \begin{bmatrix}S\end{bmatrix} \cdot \begin{bmatrix}\vec{a}^+ \\ \vec{b}^-\end{bmatrix}, \tag{2.21}$$

where the vectors $\vec{a}$ and $\vec{b}$ contain the coefficients a_m and b_n. With a single incident mode i $\vec{a}^+$ has only a single non-zero entry and $\vec{b}^-$ is empty. The coefficients of scattering matrix $[S]$ are determined by calculating the overlap integral between the incident mode field of waveguide section (1) and the mode fields of waveguide section (2)

$$b_n^+ = \left\langle \vec{E}_i^{(1)}, \vec{H}_n^{(2)} \right\rangle = \iint (\vec{E}_i^{(1)} \times \vec{H}_n^{(2)}) \cdot \vec{n}_z \, dx\, dy, \tag{2.22}$$

where $b_n^+ = \delta_{in}$ (δ_{in} being the Kronecker delta) if both waveguide sections (1) and (2) are equal and $\vec{a}^-$ is determined through the field, that was not coupled to waveguide section (2). It is assumed, that the fields are normalized according to 2.22, i.e. by $c = \left\langle \vec{E}_m, \vec{H}_m \right\rangle^{\frac{1}{2}}$.

Since, as mentioned before, M and N include all modes - the guided modes and an infinite amount of radiation modes - equation system 2.21 is in practice truncated, resulting in a finite system of linear equations. The number of modes included in the calculation determine the accuracy of the system. Unfortunately, the Eigenmode Expansion method scales very poorly with the number of modes and is therefore only applicable if the cross section of the device modeled or its numerical aperture support only a moderate amount of modes [47, 48].

On the other hand, the length of the structure is not a limit to the performance of the method as it is the case for the FDTD and FE methods. Therefore, it is very well suited for the simulation of MMIs or directional couplers, where only a moderate amount of modes is needed for an accurate representation of the fields inside the devices [49].

2.2.3 Finite Element Method

In contrast to the Eigenmode Expansion and FDTD methods, the Finite Element Method is not limited to electromagnetic field problems, but rather a more general tool for solving partial differential equations. In fact this method is most commonly used for stress analysis in complex structures or thermal conductivity problems, where it originated from. For a detailed account on the history of FEM the reader may refer to [50]. As is the FDTD method the Finite Element Method is a generic approach, since any kind of (electromagnetic) problem can be solved without making assumptions about the solution, provided that computational resources are sufficient. This method also relies on a discretization of the computational domain, but it is more flexible, as the cells do not have to be equal or even of the same kind. The first applications to electromagnetic field problems are reported in [51, 52].

Different implementations of the Finite Element Method are feasible. Here the use of the so called weak formulation of a problem is used to solve the original problem. As an example, the mode field in a homogeneous, isotropic waveguide is determined through the scalar potential $\vec{E} = -\nabla\phi$. Thus the Helmholtz equation and boundary condition are given by

$$\Delta_t\phi + k^2\phi = 0, \quad \frac{\partial\phi}{\partial n} = 0 \text{ on } d\Omega, \tag{2.23}$$

where Ω is the computational domain and $d\Omega$ is its boundary. The weak formulation of equation 2.23 is obtained by multiplying both sides with so called test functions ψ and integrating over the computational domain Ω.

$$\iint_\Omega \psi\Delta_t\phi\, dS + \iint_\Omega k^2\psi\phi\, dS = 0. \tag{2.24}$$

Using the identities

$$\nabla_t(\psi(\nabla_t\phi)) = \nabla_t\psi\cdot\nabla_t\phi + \psi(\nabla_t\nabla_t\phi) \tag{2.25}$$

and

$$\iint_\Omega \nabla_t\nabla_t\phi\, dS = \int_{d\Omega} \nabla_t\phi\vec{n}\, dl, \tag{2.26}$$

where $\vec{n}$ is the normal vector of the domain's boundary $d\Omega$, equation 2.24 may be rewritten as

$$\iint_\Omega \nabla_t\psi\nabla_t\phi\, dS - \iint_\Omega k^2\psi\phi\, dS = \int_{d\Omega} \psi\frac{d\phi}{dn}dl. \tag{2.27}$$

Although equations 2.23 and 2.27 describe the same problem, the weak formulation of equation 2.27 only requires first order derivatives of the solution, while the original problem demands second order derivatives.

As mentioned before, the the Finite Element Method relies on a discretization of the computational domain into smaller elements, which can be theoretically of any form. In practice, most commonly triangles - or tetrahedrons in the three dimensional case - are used, because any topology can be decomposed to a chosen degree of accuracy with a comparatively low computational effort [53]. The algorithms to do so are widely known as they have a broad field of applications [54, 55]. The decomposition of a computational domain is shown in figure 2.6. Due to the homogeneous and symmetrical nature of the specific problem, the mesh consists of

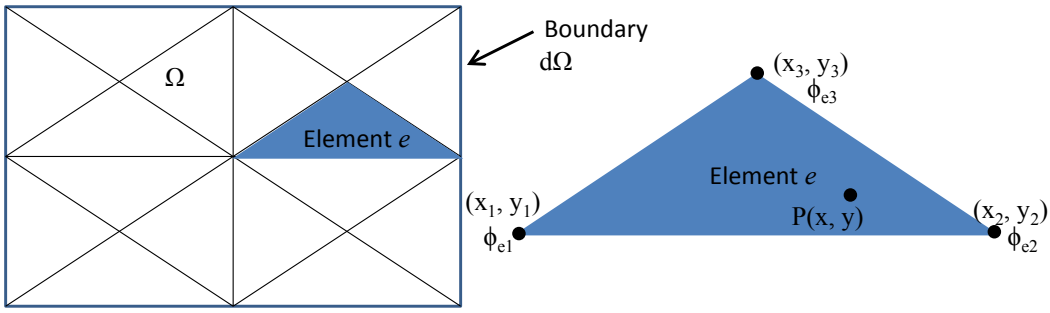

Figure 2.6: Decomposition of a computational domain into finite elements of triangular shape.

equal finite elements. One of the strengths of the Finite Element Method is, that this is not a necessary condition for the method to work. In contrast, the mesh can be dense in regions, where a rapid change in field is expected and coarse everywhere else. This nonuniform grid allows for lower computational costs compared to other methods, which rely on discretization of the computational domain, as e.g. the FDTD method. The solution of 2.23 on the complete computational domain Ω is obtained through superposition of solutions on each element e:

$$\phi(x, y) = \sum_{e=1}^{N} \phi_e(x, y) \tag{2.28}$$

The field inside the finite element e is approximated by

$$\phi_e(x, y) = \sum_{i=1}^{3} \phi_{e,i}\psi_{e,i}(x, y), \tag{2.29}$$

where

$$\psi_{e,i}(x, y) = \frac{1}{2A_e} \cdot (a_{e,i} + b_{e,i}x + c_{e,i}y + d_{e,i}x^2 + e_{e,i}xy + f_{e,i}y^2 \ldots) \tag{2.30}$$

is the test function and is in this case a polynomial. However, equation 2.30 is truncated so that only a polynomial of degree p remains, which is also referred to as the finite element degree. Here only a linear interpolation ($p = 1$) is considered, so that the remaining coefficients are

$$a_{e,i} = x_{e,j}y_{e,k} - x_{e,k}y_{e,j} \tag{2.31a}$$
$$b_{e,i} = y_{e,j} - y_{e,k} \tag{2.31b}$$
$$c_{e,i} = x_{e,k} - x_{e,j}, \tag{2.31c}$$

with i, j and k being cyclic permutations of the element corner points 1, 2 and 3. A_e is the area of element e and is determined by the nodal positions (x_i, y_i), $i = 1 \ldots 3$ (c.f. figure 2.6).

Substituting 2.28 and 2.29 into 2.27 and making use of the linearity of all operators involved yields

$$\sum_{e=1}^{N}\sum_{i=1}^{3} \phi_{e,i} \iint_{\Omega_e} \nabla_t\psi_{e,j}(x, y)\nabla_t\psi_{e,i}(x, y)\, dS - k^2\psi_{e,j}(x, y)\psi_{e,i}(x, y)\, dS = 0. \tag{2.32}$$

Since $\psi_{e,j}$ is nonzero only on element e the outer sum can be neglected and 2.32 can be reformulated as a linear equation system for each finite element:

$$\begin{bmatrix} A_{e,11} & A_{e,12} & A_{e,13} \\ A_{e,21} & A_{e,22} & A_{e,23} \\ A_{e,31} & A_{e,32} & A_{e,33} \end{bmatrix} \cdot \begin{bmatrix} \phi_{e,1} \\ \phi_{e,2} \\ \phi_{e,3} \end{bmatrix} = \begin{bmatrix} 0 \\ 0 \\ 0 \end{bmatrix}, \tag{2.33}$$

where

$$A_{e,ij} = \iint_{\Omega_e} \nabla_t \psi_{e,i}(x,y) \nabla_t \psi_{e,j}(x,y)\, dS - k^2 \iint_{\Omega_e} \psi_{e,i}(x,y)\psi_{e,j}(x,y)\, dS. \tag{2.34}$$

The integrals in 2.34 can be evaluated individually, giving rise to

$$\iint_{\Omega_e} \nabla_t \psi_{e,i}(x,y) \nabla_t \psi_{e,j} dS = \frac{1}{4A_e} \begin{bmatrix} b_{e,1}^2 + c_{e,1}^2 & b_{e,1}b_{e,2} + c_{e,1}c_{e,2} & b_{e,1}b_{e,3} + c_{e,1}c_{e,3} \\ b_{e,2}b_{e,1} + c_{e,2}c_{e,1} & b_{e,2}^2 + c_{e,2}^2 & b_{e,2}b_{e,3} + c_{e,2}c_{e,3} \\ b_{e,3}b_{e,1} + c_{e,3}c_{e,1} & b_{e,3}b_{e,2} + c_{e,3}c_{e,2} & b_{e,3}^2 + c_{e,3}^2 \end{bmatrix} \tag{2.35a}$$

$$\iint_{\Omega_e} \psi_{e,i}(x,y)\psi_{e,j} dS = \frac{A_e}{12} \begin{bmatrix} 2 & 1 & 1 \\ 1 & 2 & 1 \\ 1 & 1 & 2 \end{bmatrix}. \tag{2.35b}$$

The last step necessary for obtaining the solution to the initial problem is the summation 2.28. This is done via assembly of the local matrices $[A_e]$ into a global matrix $[A]$. This process is straightforward, however it should be noted, that nodes are shared among neighboring elements. This property reduces the number of nonzero entries in $[A]$ resulting in a sparse matrix, which is numerically very inexpensive to handle.

The stability and performance of various algorithms for solving the remaining eigenvalue problem has been subject to research [56, 57] and is implemented in highly optimized packages for different system architectures [58].

It is evident though, that matrix $[A]$ can still become quite big, when the number of elements, the number of nodes within each element or the polynomial degree p increases, thus having a large impact on memory consumption and computational cost. As with the FDTD method this is the main limiting factor in the application of this method.

The shown example is somewhat limited in application as it only describes scalar propagation modes in a homogeneous and isotropic waveguide. For more general structures or other applications such as resonant modes or scattering analysis require the weak formulation of Maxwell's curl equations, which can be fully vectorial and also include complex, anisotropic materials. Other approaches to the Finite Element Method, e.g. via minimization of functionals also offer valid solutions to each problem class and can be found in [59]. Commercial implementations are highly optimized and available for use. The FEM solver used throughout this thesis is described in [60].

2.2.4 Boundary Conditions

To be applicable to the problems discussed in this thesis, the introduced simulation methods need to model scattered fields in an open environment. Although this

is somewhat contradictory to the finite computational resources available, there are mathematical constructs, which are designed to suppress reflections from metallic or magnetic boundary conditions imposed on the computational domain and therefore emulate an infinite computational domain. Most commonly these are referred to as Perfectly Matched Layers (PMLs) or transparent boundary conditions [61].

By having an absorber in front of the ordinary domain boundary, where tangential field components are forced to be zero, reflections are minimized. This can either be achieved by assigning complex, anisotropic permittivities or permeabilities to the absorber [62] or by adding an additional imaginary spatial dimension in the boundary domain [63]. In both cases reflections for a wide range of incident plane waves can be minimized. Usually PMLs are associated with frequency domain implementations but time domain implementations as required for the FDTD method are available as well [64, 65].

2.2.5 Other Methods

There are several other methods available for the computation of electromagnetic fields, but only a few are suitable for integrated optics. One of the oldest methods is the Beam Propagation Method (BPM), which assumes a slowly varying device along the axis of propagation [66]. With a chosen input field, the transmission characteristics of a device can then be determined by eliminating the second order derivative with respect to the propagation direction. However, this assumption makes the Beam Propagation Method unsuitable for the simulation of grating couplers because of the rapid change in the propagation direction of the electric field. Similar to the Eigenmode Expansion method it is better used with MMIs or other structures with invariant dimensions. Another disadvantage of this method is the inability to handle material systems with high refractive index contrast well, which is generally the case for nano wires on SOI.

The Rigorous Coupled-Wave Analysis (RCWA) is a method, which was specifically designed for the simulation of periodic structures. It expresses materials and electric or magnetic fields as Fourier expansions in space and solves for a spectrum of periodic modes known as Floquet or Bloch waves [67, 68]. This method is therefore similar to the Eigenmode Expansion method, as it expresses the solution to a scattering problem as a superposition of fields. However, it can be seen, that while the Eigenmode Expansion method only needs a moderate amount of modes to yield accurate results, the RCWA has difficulties with abrupt changes in material properties, especially in the case of high refractive index contrast, since a large amount of spatial harmonics is needed to accurately model such structures. This problem is known as the Gibbs phenomenon [69] and is the reason, why RCWA is also not well suited for the simulation of fiber grating couplers on SOI.

2.3 Near- and Far-Field

Due to limited computational resources, it is not convenient to obtain field data from electromagnetic field simulations directly, especially when the point of observation is far away from the scatterer. In this case, a near- to far-field transformation can be used that yields the electromagnetic field at any point in the distance from the field computed in the simulation, provided the simulated field and the point

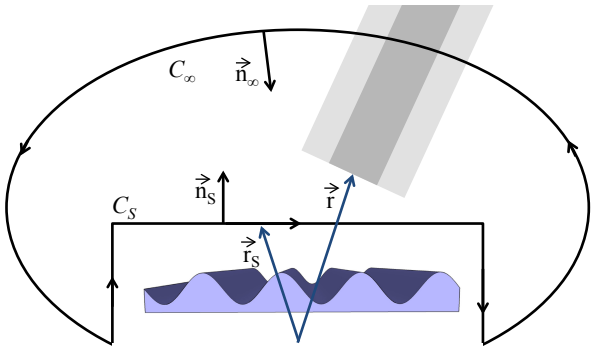

Figure 2.7: Sketch of integration contours for two dimensional scattering from a diffraction grating.

of observation are within a homogeneous medium and no obstacles or additional sources can be found between them.

In the case of a fiber grating coupler this transformation can be utilized to obtain the field coupled to the fiber by transforming the simulated field to the plane of the fiber and calculating the overlap with the fiber mode. This method neglects potential reflections from the facet of the fiber back towards the grating but it is a good approximation of the real coupling efficiency. The advantage of obtaining fields at large distances by transformation is, that the fiber does not need to be included in the simulation. Since the fiber is relatively far away from the grating (ca. $10\mu m$, depending on the fiber tilt angle φ) and is very large compared to dimensions of integrated devices, excluding the fiber from the simulation saves a lot of computational resources and time, since only the fields directly adjacent to the grating are used.

Usually the far-field transformation is applied, when the distance between near-field and point of observation is very large. Depending on the phase and amplitude error one allows for with given dimensions of the scatterer, a minimum distance to the observation point may be defined, for which the far-field transformation is valid. However, since for the fiber-grating setup the error would be too large, the far-field transformation is not quite applicable here, rather one has to speak of a near-field transformation.

Considering a setup as shown in figure 2.7, where the field at the fiber's facet is of interest but its location $\vec{r}$ is not within the computational domain of the scattering grating coupler, a near-field transformation may be applied. To obtain the field at point $\vec{r}$ caused by the field at point $\vec{r}_S$ at the border of the computational domain Green's theorem [70] is applied

$$\begin{aligned}\int_S [\phi(\vec{r}_S)(\nabla^2)G(\vec{r},\vec{r}_S) - G(\vec{r},\vec{r}_S)(\nabla^2)\phi(\vec{r}_S)]dS \\ = \oint_{C_\infty} [\phi(\vec{r}_S)\frac{\partial G(\vec{r},\vec{r}_S)}{\partial r_S} - G(\vec{r},\vec{r}_S)\frac{\partial \phi(\vec{r}_S)}{\partial r_S}]dC \\ - \oint_{C_S} [\phi(\vec{r}_S)\frac{\partial G(\vec{r},\vec{r}_S)}{\partial n_S} - G(\vec{r},\vec{r}_S)\frac{\partial \phi(\vec{r}_S)}{\partial n_S}]dC,\end{aligned} \tag{2.36}$$

where G is Green's function, ϕ is the scalar electric or magnetic field, $\vec{r}$ is the point of observation on the fiber's facet and $\vec{r}_S$ is the coordinate of the source. The closed

surface S, which contributes to the resulting field at $\vec{r}$ is split into two subdomains C_S and C_∞. On the contour C_S the diffracted field from the grating is simulated, which serves as the source for the field transformation. Similar to the reduction of integration contours for the Kirchhoff diffraction, the contour C_∞ is assumed to be sufficiently far away to yield no contribution to the field transformation. Therefore, the integral term over C_∞ in equation 2.36 can be neglected. The term $(\nabla^2)G(\vec{r},\vec{r}_S)$ can be rewritten as

$$(\nabla^2)G(\vec{r},\vec{r}_S) = \delta(\vec{r}-\vec{r}_S) - k^2 G(\vec{r},\vec{r}_S) \tag{2.37}$$

and from the Helmholtz equation we derive

$$(\nabla^2)\phi(\vec{r}_S) = -k^2\phi(\vec{r}_S). \tag{2.38}$$

Substituting 2.37 and 2.38 into 2.36 yields

$$\phi(\vec{r}) = \oint_{C_S} [G(\vec{r},\vec{r}_S)\frac{\partial\phi(\vec{r}_S)}{\partial n_S} - \phi(\vec{r}_S)\frac{\partial G(\vec{r},\vec{r}_S)}{\partial n_S}]dC. \tag{2.39}$$

In the two dimensional case G is expressed by the Hankel function

$$G(\vec{r},\vec{r}_S) = \frac{1}{4}H_0^{(1)}(k|\vec{r}-\vec{r}_S|). \tag{2.40}$$

In three dimensions the full vector quantities of the electric and magnetic field are needed, since the reduction to scalar fields does not apply here. The field transformation is given by [71]

$$\vec{E}(\vec{r}) = -i\omega[\vec{A} + \frac{1}{k^2}\nabla(\nabla\cdot\vec{A})] - \frac{1}{\epsilon}\nabla\times\vec{F} \tag{2.41a}$$

$$\vec{H}(\vec{r}) = -i\omega[\vec{F} + \frac{1}{k^2}\nabla(\nabla\cdot\vec{F})] + \frac{1}{\mu}\nabla\times\vec{A}, \tag{2.41b}$$

with

$$\vec{A}(\vec{r}) = \frac{\mu}{4\pi}\iint_S \vec{J}_S\frac{e^{-ik|\vec{r}-\vec{r}_S|}}{|\vec{r}-\vec{r}_S|}dS \tag{2.42a}$$

$$\vec{F}(\vec{r}) = \frac{\epsilon}{4\pi}\iint_S \vec{M}_S\frac{e^{-ik|\vec{r}-\vec{r}_S|}}{|\vec{r}-\vec{r}_S|}dS, \tag{2.42b}$$

where $\vec{J}_S$ and $\vec{M}_S$ are the equivalent current densities of the source field defined by

$$\vec{J}_S = \vec{n}_S\times\vec{H}_S \tag{2.43a}$$

$$\vec{M}_S = -\vec{n}_S\times\vec{E}_S. \tag{2.43b}$$

2.3.1 The Gaussian Beam

Obtaining the field at the facet of the fiber through field transformation as mentioned in the previous section is accurate, but numerically expensive due to the involvement

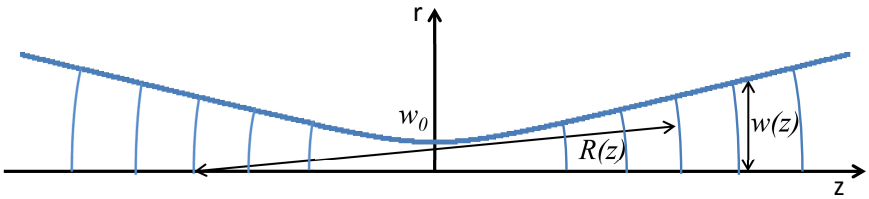

Figure 2.8: Gaussian beam with spot size diameter w and curvature R.

of the Hankel function. Reciprocity demands, that coupling from the integrated waveguide to the fiber is equal to coupling from the fiber to the integrated waveguide. Thus transforming the fiber mode onto the grating yields equal results to the scheme discussed in the previous section. However, the near field transformation of the fiber mode is equally numerically expensive as the transformation of the diffracted field from the grating to the fiber. Nevertheless, 'reversed' coupling may be preferred, since the design of the fiber and thus the fiber mode is fixed and therefore the transformation from fiber to grating has to be conducted only once, while in the case of 'regular' coupling for every change in grating design a new transformation is necessary as the diffracted field changes its shape.

In addition, the fundamental fiber mode can be to a large degree of accuracy be approximated by a Gaussian distribution.

$$U(r) = U_0 \exp(-\frac{r^2}{w_0^2}), \tag{2.44}$$

where r the radial direction and w_0 is the spot size radius of the beam. The scalar field U at any point (r, z) may then be calculated by

$$U(r,z) = \frac{w_0}{w(z)} U_0 \exp(-ik(z + \frac{r^2}{2R(z)}) + i \arctan(\frac{2z}{kw_0}) - \frac{r^2}{w^2(z)}). \tag{2.45}$$

The functions $w(z)$ and $R(z)$ are the spot size radius and the radius of curvature at distance z, respectively. They are given by

$$w(z) = w_0 \sqrt{1 + (\frac{2z}{kw_0^2})^2} \text{ and} \tag{2.46a}$$

$$R(z) = z(1 + (\frac{kw_0^2}{2z})^2). \tag{2.46b}$$

A graphic representation of $w(z)$ and $R(z)$ is shown in figure 2.8. The solid blue curve shows the spot size radius w along the axis of propagation z and R is represented through circular lines between the z-axis and $w(z)$. The field starts out with a flat phase and a spot size diameter w_0, which becomes increasingly more circular as the beam expands. The circular phase fronts between $z = 0$ and $z = \infty$ are the main reason for a diminishing coupling efficiency, since the field scattered by the grating exhibits flat phase fronts and has the highest overlap with a Gaussian beam, when its phases are also flat. Therefore, it is advisable to have a distance between grating coupler and fiber as low as possible.

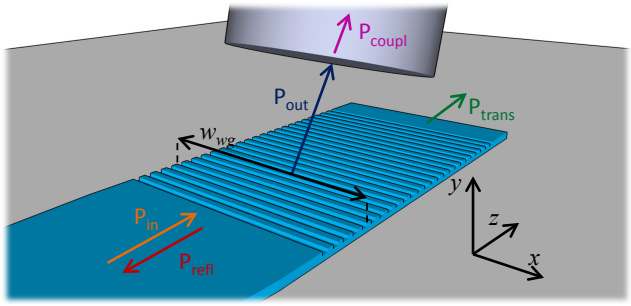

Figure 2.9: Sketch of the grating coupler setup with fiber.

2.4 Definitions

Throughout this thesis the setup for fiber chip coupling using grating couplers remains mostly the same. Figure 2.9 depicts a basic layout of such a setup. Due to reciprocity, the direction of operation is irrelevant to the performance of the device, i.e. one and the same setup can be used equally for coupling from the fiber to the integrated waveguide and from the integrated waveguide to the fiber. Therefore, the coupling efficiencies for in- and out-coupling are necessarily equal. In this thesis mostly the out-coupling direction is analyzed, as it allows for better distinction of the parameters that contribute to the performance of the device.

The setup consists of an integrated waveguide, that is adiabatically tapered from the usual waveguide width w_{wg} (depending on the waveguide type approximately 500nm to 750nm) to a width of around $10\mu m$ to accommodate a fundamental waveguide mode, whose spot size matches the fundamental fiber mode's spot size in the transverse (x-) direction. Through periodic etching, the grating is inscribed into the widened waveguide, which diffracts light in the waveguide towards the fiber, which, if done over an appropriate length, leads to a high overlap with the fiber mode in the lateral (z-) direction. The fiber itself is a standard single mode fiber with a spot radius of the fundamental mode of $5\mu m$ and is tilted at an angle φ with respect to the chip's surface normal (y-direction). This prevents unwanted reflections from the fiber's facet back onto the grating and thus into the waveguide. Additionally, as will be shown later, coupling angles $\varphi \neq 0°$ display a higher coupling efficiency. For optimal coupling the angle, at which the field is diffracted and the fiber tilt angle should be equal. Thus only one value φ is used to describe both.

For the simulations however the fiber is not included in the setup, but as explained in chapter 2.3 the overlap of the scattered field at the position of the fiber with the fundamental fiber mode is calculated. The field overlap η_F is defined by

$$\eta_F = \iint_{-\infty}^{\infty} \vec{E}_g \times \vec{H}_f^* \, dA, \tag{2.47}$$

where $\vec{E}_g$ is the diffracted electric field from the grating and $\vec{H}_f^*$ is the conjugated magnetic field of the fiber mode. The overlap used here is not related to fields but

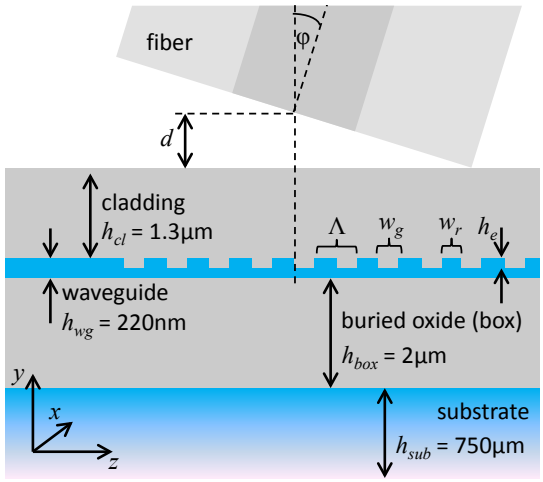

Figure 2.10: Cross sectional view of the fiber grating coupler with design parameters.

to power and can be obtained through the square of equation 2.47

$$\eta = \frac{|\iint_{-\infty}^{\infty} \vec{E}_g \times \vec{H}_f^* \, d\vec{A}|^2}{\mathrm{Re}(\iint_{-\infty}^{\infty} \vec{E}_g \times \vec{H}_g^* \, d\vec{A} \cdot \iint_{-\infty}^{\infty} \vec{E}_f \times \vec{H}_f^* \, d\vec{A})}. \tag{2.48}$$

The value is normalized with respect to the overlap integral 2.47 (i.e. $\iint \vec{E}_g \times \vec{H}_g^* dA = 1$ and $\iint \vec{E}_f \times \vec{H}_f^* dA = 1$), thus the total coupled power P_{coupl} can be calculated by

$$P_{coupl} = \eta \cdot P_{out}, \tag{2.49}$$

where P_{out} is the fraction of power relative to the incoming power, that is diffracted in positive y-direction. In the literature the term 'directionality' is also used from time to time to distinguish between power scattered upwards P_{out} (positive y-direction) and downwards (P_{down}) (negative y-direction)

$$\text{directionality} = \frac{P_{out}}{P_{out} + P_{down}}. \tag{2.50}$$

Since the majority of power is scattered either upwards or downwards, this value gives a good estimation of the grating's performance. However, it neglects the influence of reflected (power reflected back from the grating into the waveguide) and transmitted power (power passing through the grating and remaining in the waveguide) and can thus be only regarded as a rough approximation. P_{out} is normalized to the complete power, that is shone onto the grating and is therefore exact. For convenience, in the following when using P_{out} it is already assumed to be normalized without mention of the input power.

The grating itself is described by many design parameters, which can be seen in figure 2.10. The values concerning the SOI stack do have an influence on the performance of the grating coupler and may therefore be subject to optimization, however limitations in available substrates and in process technology do not allow for variations. Therefore, substrate height h_{sub}, buried oxide thickness h_{box}, waveguide height h_{wg} and cladding thickness h_{cl} are fixed to the values shown in figure 2.10.

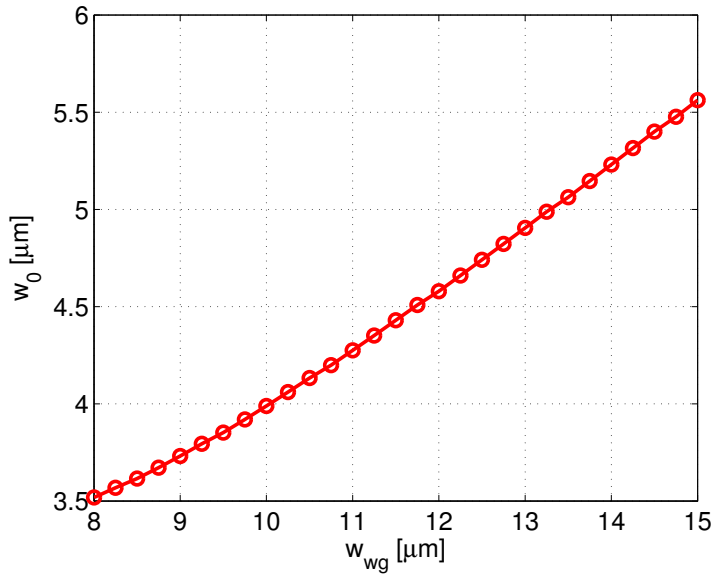

Figure 2.11: Optimal spot size radius w_0 of a fundamental fiber mode for maximum lateral overlap with a fundamental waveguide mode TE_{00} in a waveguide of width w_{wg} at $\lambda = 1.55\mu$m.

The grating parameters groove width w_g, ridge width w_r and etch depth h_e are the primary values for optimization and will be discussed for each grating separately. In the literature grating period $\Lambda = w_g + w_r$ and duty cycle $d_c = w_g/\Lambda$ (sometimes also referred to as fill factor) are commonly used instead of groove width and ridge width, as these values are closer to the analytical expressions shown in chapter 2. However, the quantities used here are more related to fabrication and are therefore easier to evaluate for fabrication tolerance.

The distance d between the chip's surface and fiber center point is usually around $10\mu m$ but depends on the fiber tilt angle φ. Since the fiber is very wide (usually a diameter of $125\mu m$), the distance to the chips surface must be large enough in the center of the fiber to avoid contact at the edges. The position of the fiber in x-direction is centered over the grating and in z-direction the optimal position for highest coupling efficiency is used to calculate performance.

The optimal width of the waveguide section, where the grating is located, is determined by the spot size of the fiber mode the waveguide is coupled to. In the case of the LP_{01} mode of an SMF-28, whose spot size diameter is denoted with with $d_0 = 2w_0 = 10.4\mu m \pm 0.5\mu m$ at $\lambda = 1.55\mu m$ wavelength [72], the waveguide width $w_{wg} = 13\mu m$ gives optimal overlap in transverse waveguide direction with a fiber in 10μm distance (c.f. figure 2.11).

Chapter 3

Fabrication & Measurement

To give an overview about the realization and characterization of the fiber grating couplers presented throughout this thesis, this chapter introduces the fabrication process used at IHP to produce the integrated optical devices, that were designed and analyzed here. Furthermore, the measurement setup at TU Berlin, with which the devices are characterized, will be detailed.

3.1 Fabrication

IHP's $0.25\mu m$ BiCMOS process SG25H1 is used as a baseline for fabrication of all optical devices throughout this thesis. The photonic modules are co-integrated in the process flow of the standard BiCMOS line enabling the production of fully optoelectronic circuits. A description of the co-integration process can be found in [73], where a monolithically integrated receiver chip with both electronic and photonic components is outlined. The relevant steps for grating couplers in the process flow are the formation of the waveguides, whose position in process flow is dependent on the waveguide type (i.e. nano wire or rib waveguide), the grating etches and the photonic protection layers, which are relevant for the grating design as they constitute the cladding material and do influence the performance of the devices.

Nano wire waveguides are processed at the very beginning of the flow with the grating etches done in a second etch step on a different mask layer. The two distinct etch steps are necessary, since the etch depth used for waveguides (down to the buried oxide of the SOI stack) is usually much deeper than that for gratings (depending on the waveguide height ca. 70nm - 300nm). Additionally, the features of the grating potentially exhibit much smaller sizes than found in waveguides. Thus having the fabrication on two etch steps allows for an eventual readjustment for smaller critical dimensions.

For the rib waveguides the grating etches are produced simultaneously as they are by design of equal etch depth as the slab region of the waveguide. This will be also the case for gratings presented in chapter 4.1, where very basic gratings are designed for operation around the wavelength $\lambda = 1.31\mu m$. Obviously, using only a single etch step for both waveguides and gratings saves expensive mask space, rendering the use of rib waveguides in this case more economical. However, in later chapters more efficient gratings are presented, which exhibit etch depths, that do not match the waveguide height, resulting in the necessity of two etch steps.

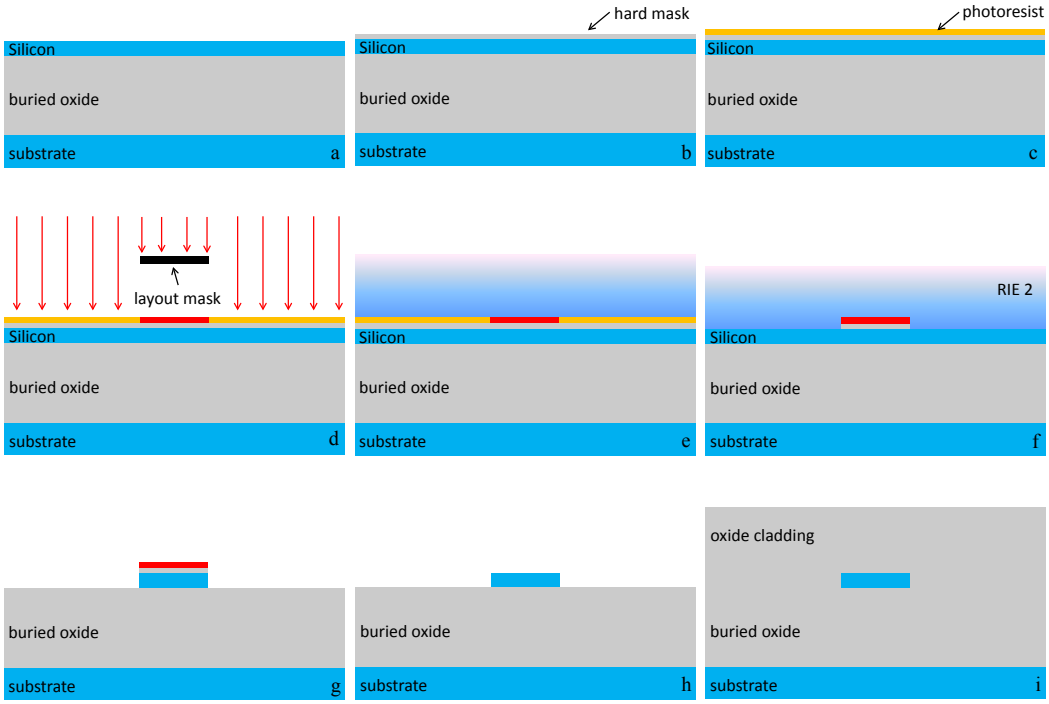

Figure 3.1: Basic fabrication flow of a nano wire.

Figure 3.1 depicts the basic process flow used for fabrication of a nano wire using positive tone resist. Rib waveguides and grating etches are produced similarly using negative tone resist and etch depths, that do not reach all the way down to the buried oxide.

After cleaning the wafer, the top silicon layer is coated with an oxide hard mask before the photoresist is applied to it. Using deep UV projection lithography at 248nm wavelength the layout from the mask is projected onto the surface of the wafer. For positive photoresist, the part, which is exposed to the DUV light becomes soluble and is later removed using reactive ion etching (RIE) together with the hard mask and in a second RIE step the top silicon layer is cleared, where the unexposed parts of the top silicon layer remain. As a last step, the wafer is covered again with an SiO_2 protection layer. The grating etches are added by a repetition of steps b to h, before covering the wafer with the oxide layer (step i) using another mask layout and negative photoresist. For rib waveguides the inclusion of grating etches is conducted simultaneously, requiring no repetition of steps as mentioned before .

Gratings from chapter 4.2 onwards will make use of a locally increased waveguide height to increase performance. Fabrication-wise this is achieved by a selective epitaxial growth of silicon in the required region between waveguide fabrication and grating etch step. Figure 3.2 outlines this process. Again, positive tone resist is used for the epitaxial growth using a hard mask and RIE. BiCMOS protection layers

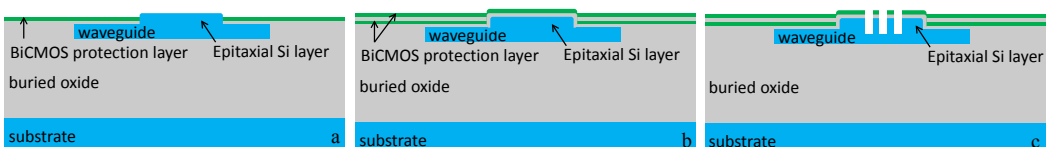

Figure 3.2: Fabrication of silicon epitaxial layer and grating etches.

(Si_3N_4) are added as a side effect from electronic processing taking place between the photonic process steps.

3.2 Measurement

The experimental characterization of the gratings is conducted via a simple transmission measurement. Figure 3.3 depicts a block diagram of the measurement setup used at TU Berlin to characterize integrated optical devices.

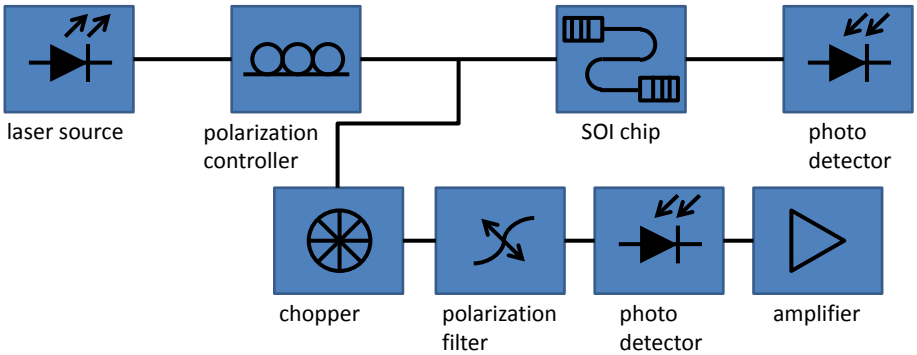

Figure 3.3: Block diagram of the measurement setup used for the characterization of fiber grating couplers.

Light is coupled through a standard single mode fiber (sSMF) from a tunable laser source (Agilent 81940A) to a polarization controller (Agilent 8169A), which is used to ensure a linear TE polarization at the grating. Environmental noise is reduced with a calibration setup consisting of a chopper, a polarization filter, a detector and a lock-in amplifier, which is decoupled before the transmission measurement is done. The sample is placed on a stage, which is heated to 35°C to ensure a constant and stable temperature and therefore reduce inconsistent thermo-optic effects, which could potentially result in fluctuations in the measured devices.

After passing through the sample, light is again coupled to a SMF and guided to the detector (Agilent 81634B), which records the spectrum of the whole transmission line. To determine the performance of a specific device, losses induced through the measurement setup and waveguides on chip have to be deducted using reference measurements. The effect of the measurement setup on the transmission spectrum can be obtained by conducting a fiber to fiber measurement, where the sample is excluded and instead light is butt-coupled directly from one fiber to another. Waveguide losses are determined using identical transmission lines with varying waveguide lengths. Figure 3.4 shows raw data for fiber to fiber reference measurements (blue) and transmission measurements for nano wires (left) and rib waveguides (right) for three different waveguide lengths. It is apparent, that rib waveguides exhibit much smaller losses compared to nano wires, as the difference in transmitted power of different waveguide lengths is much smaller. The dip in all three measurements at $\lambda = 1.58\mu m$ originates from the filter curve, that the grating couplers contribute to the transmission spectrum.

Since the reference measurements do not include grating couplers, but couple directly from fiber to fiber, the grating filter curve is not featured in there. The waveguide losses are obtained through the inclination of transmission power as a function

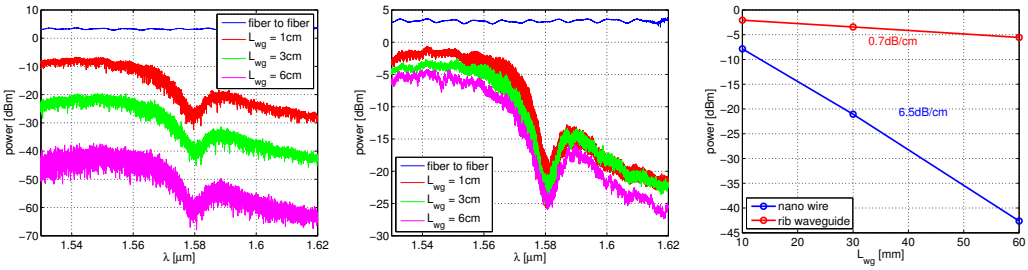

Figure 3.4: Transmission measurements (left: nano wires, middle: rib waveguides) over wavelength of a fiber to fiber setup (blue) and a grating setup with three different waveguide lengths (red: 1cm, green: 3cm and magenta: 6cm). Right: Transmission power as a function of waveguide length at $\lambda = 1.55\mu m$.

of waveguide length at a certain wavelength (see figure 3.4 (right)) and amount to 6.5dB/cm for nano wires and 0.7dB/cm for the rib waveguide at $\lambda = 1.55\mu m$ in this specific example. The noisy nature of the curves is compensated by evaluating the median value of five measurement points around the center wavelength λ.

Chapter 4

1D Gratings

In this chapter one dimensional grating couplers are presented with increasing complexity and coupling efficiency. The first grating coupler is very similar to the standard fiber grating coupler shown by Taillaert et al. [17], but is adapted for the use with the substrate available for this work and a wavelength of $\lambda = 1.31\mu m$. In the next section, the directionality of the grating is increased by the placement of a silicon overlay on top of the grating coupler, which increases the coupling efficiency by simply scattering more light towards the fiber. The following section improves upon this concept by increasing the field overlap of the diffracted field with the fundamental mode of a fiber through the introduction of a secondary etch step in front of the grating, while maintaining a high directionality.

After that, considerations are made of how an optimal design of a fiber grating coupler for maximum possible out-coupling and field overlap might be constituted and how it might be obtained numerically. Additionally a resulting design with very high performance is presented.

4.1 Gratings for $\lambda = 1.31\mu$m

The first grating to be presented is an adaptation of the standard grating coupler [17] for the center wavelength $\lambda = 1.31\mu m$ and the available SOI layer stack. The purpose of this grating is to assist in the reduction of noise and jitter of a quantum-dot laser in an integrated optical feedback loop. This mode locking technique has been implemented using fibers [74], but an integrated solution would offer higher compactness compared to a fiber based one. The laser shows best performance when tuned to the wavelength $\lambda = 1.31\mu m$, for which coupling to the integrated waveguide had to be performed.

A cross-sectional view of the grating coupler is shown in figure 4.1. The grating is shallowly etched into a waveguide of $h_{wg} = 220nm$ height.

Comparing the effective refractive indices of the fundamental guided mode in the integrated waveguide at $\lambda = 1.55\mu m$ ($n_{eff} = 2.85$) and $\lambda = 1.31\mu m$ ($n_{eff} = 2.99$) and substituting these values into the grating equation 2.8 leads to the conclusion, that smaller feature sizes are necessary for coupling with a shorter wavelength. Figure 4.2 shows a parameter scan of all design parameters shown in figure 4.1. Out-coupled power P_{out} of the grating, field overlap η of the diffracted grating field with the fundamental fiber mode and optimal coupling angle φ are depicted as functions of etch depth h_e, groove width w_g and ridge width w_r.

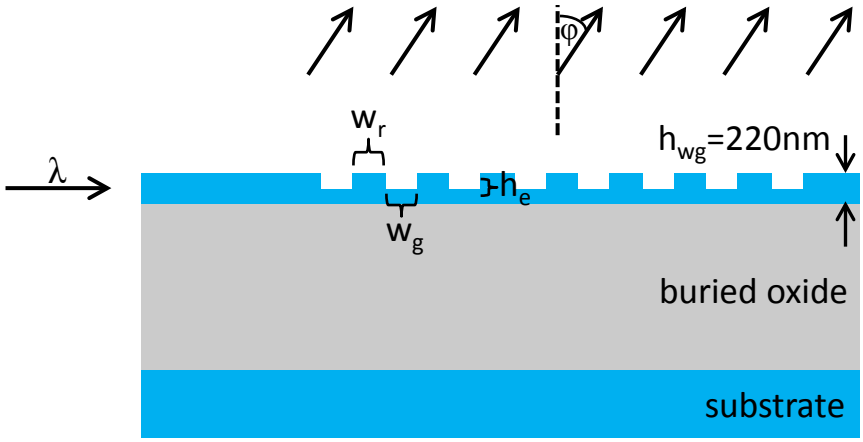

Figure 4.1: Sketch of a grating structure on the standard SOI stack.

The out-coupled power shows various local maxima along the main diagonal, which corresponds to the grating period $\Lambda = w_g + w_r$. These maxima represent the different diffraction orders of the grating and therefore display very different diffraction angles φ. With respect to duty-cycle, P_{out} shows generally best performance at a duty cycle of $d = \frac{w_g}{\Lambda} = 0.5$ for all etch depths and decreases near the extremes of $d = 0$ and $d = 1$. For the simulation only coupling angles φ between 3° and 20° are considered, since angles below this range potentially lead to high reflections between fiber and grating, and larger angles require a greater coupling distance, resulting in higher losses due to decreasing field overlap between scattered field and fiber mode. This constraints limits the range of acceptable grating periods to values of $450nm < \Lambda < 550nm$, where smaller grating periods are better suited for shallow etch depths h_e and large periods for deep etches.

The limitation in coupling angles is also reflected in the field overlaps η between diffracted field and fiber mode, as only a small range of grating periods allows for high performance. At an etch depth of $h_e = 50nm$ the duty cycle has almost no influence on η, but for etch depths $h_e \geq 70nm$ a balanced duty cycle of 0.5 becomes less favorable as the performance here decreases and only remains constant at the extremes of either very high or very low duty cycles. Unfortunately, the dependency of P_{out} on duty cycle is opposite to the progression of η and therefore a tradeoff between these two has to be found. Additionally, resorting to small etch depths ($h_e < 70$nm) for a constant, high overlap does also impact P_{out} negatively and a compromise has to be found here as well.

In the end an etch depth of $h_e = 70nm$ was chosen, since it offers still a high out-coupling efficiency and allows for co-integration with other devices using IHP's standard technology. In spite of the lower field overlap η at duty cycles of $d = 0.5$ the highest coupling efficiency $P_{coupl} = \eta \cdot P_{out}$ can still be found at this value, due to the maximum of P_{out} being located there and at a grating period $\Lambda = 480nm$. Therefore the design values for the grating are $w_g = 240nm$, $w_r = 240nm$ and $h_e = 70nm$, which result in a simulated coupling efficiency of 46% or $-3.3dB$ at a coupling angle $\varphi = 6°$.

The complete spectral performance of the device is shown in figure 4.3. Reflection and transmission are with 5% and 2%, respectively, quite low at the design wavelength and increase sharply at the edge of the current diffraction order. The peak wavelength for a coupling angle of $\varphi = 6°$ can be found at $\lambda = 1.312\mu m$ but

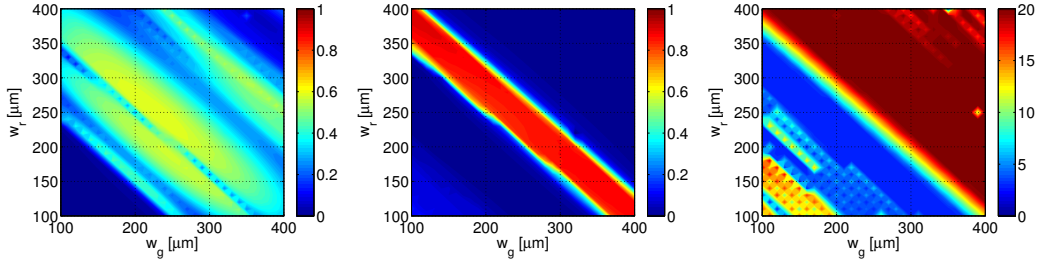

(a) Etch depth $h_e = 50nm$.

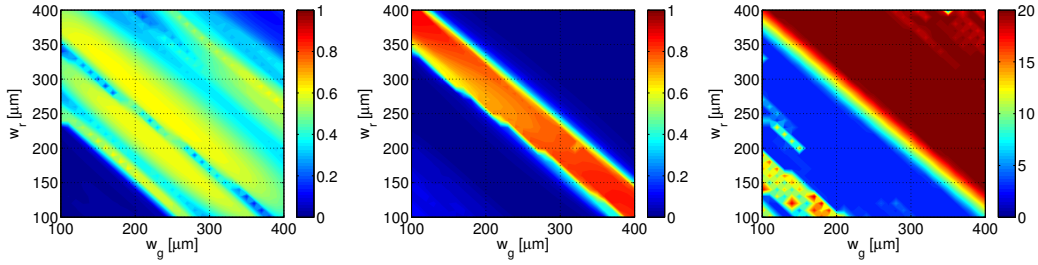

(b) Etch depth $h_e = 70nm$.

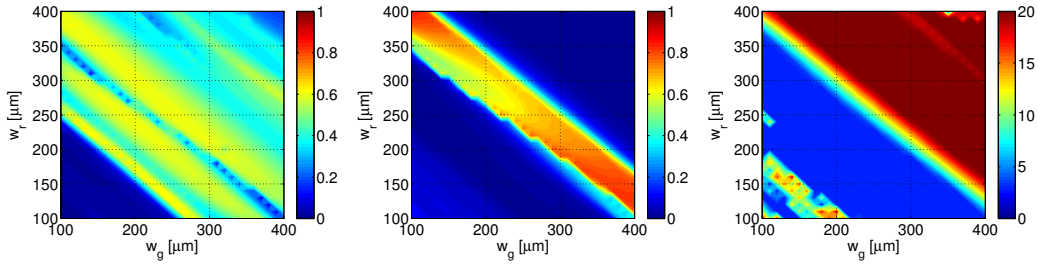

(c) Etch depth $h_e = 90nm$.

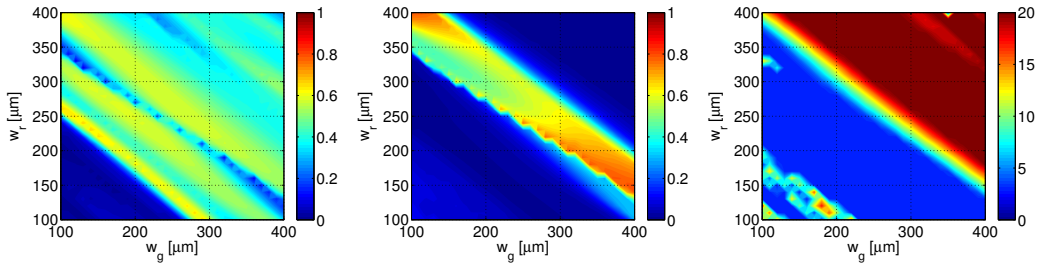

(d) Etch depth $h_e = 110nm$.

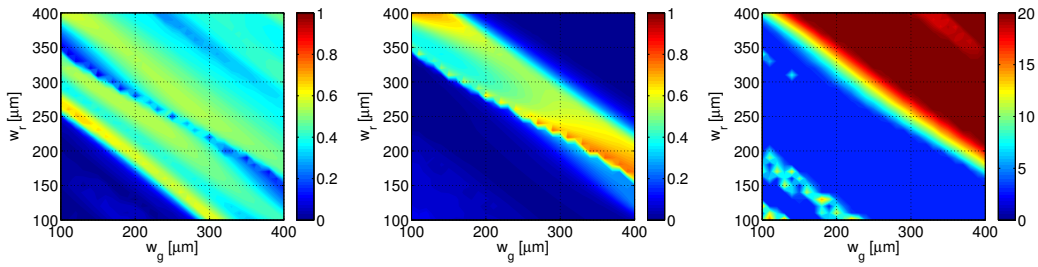

(e) Etch depth $h_e = 130nm$.

Figure 4.2: Performance plots of gratings on standard SOI stack as a function of groove width w_g and ridge width w_r for five different etch depths h_e at $\lambda = 1.31\mu m$. Left: P_{out}, middle: Field overlap η, right: Optimum coupling angle φ in degree.

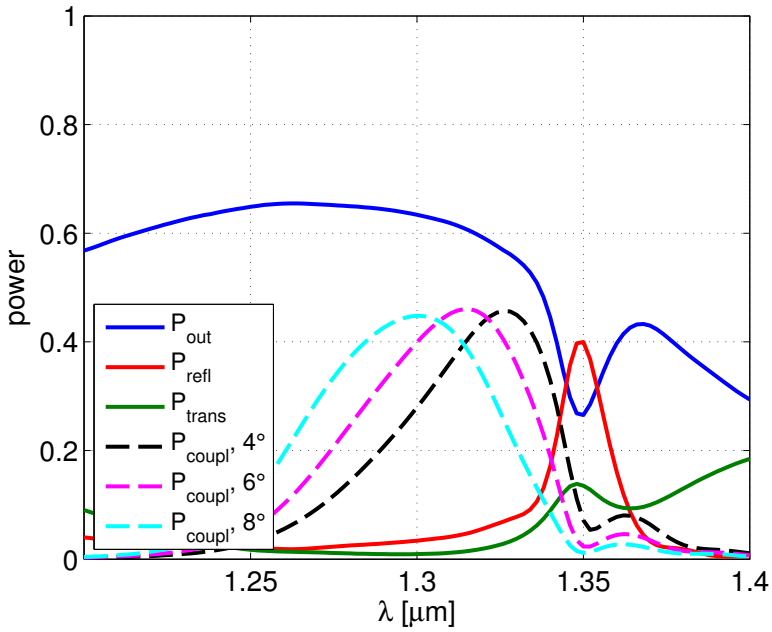

Figure 4.3: Coupling spectrum for three different fiber tilt angles (dashed lines), out-coupled power P_{out} (blue), reflected power (red) and transmitted power (green) of a grating coupler optimized for the center wavelength $\lambda = 1.31\mu m$.

may be shifted through an adaptation of the angle without much loss in coupling efficiency. The wavelength shift experienced through a 2° adaptation of the coupling angle amounts to $\Delta\lambda = 10nm$ and is accompanied by an additional loss of less than 1%.

The distance in terms of efficiency between out-coupled power (P_{out}) and coupled power to the fiber (P_{coupl}) is quite large compared to gratings shown in later chapters. This indicates a low overlap η between diffracted field and fiber mode for these gratings. Adaptations, which result in higher field overlap, will be examined in later chapters.

4.1.1 Measurement Results

The measured spectral performance of a single grating is shown in figure 4.4 for fiber tilt angles φ ranging from 2° to 12°. Waveguide losses are already subtracted and the curve is normalized with respect to a fiber to fiber reference measurement as described in chapter 3.2. Additionally, the remaining losses are divided by 2 to obtain the performance of a single grating coupler.

The measured performance is in very good agreement with the simulated predictions of figure 4.3. The optimal coupling angle for peak performance at $\lambda = 1.31\mu m$ is found at $\varphi = 6°$ and amounts to -3.8dB peak coupling efficiency. By lowering the coupling angle the performance peak can be shift to longer wavelengths with the rate of approximately 5nm/°. The same is true for shorter wavelengths and higher coupling angles. The performance drop is minimal, when moving to other wavelengths and coupling angles and is even slightly increased at shorter wavelengths, with measured global maximum of $-3.6dB$ coupling efficiency at $\lambda = 1295nm$ and a coupling angle of $\varphi = 8°$. The 1dB bandwidth reaches 23nm with a constant coupling angle.

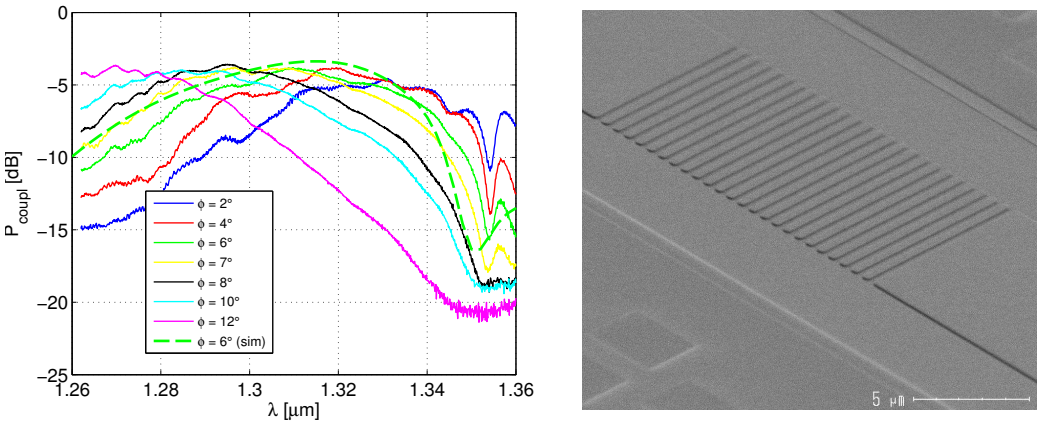

Figure 4.4: Left: Measured performance of a grating coupler ($w_g = 240nm$, $w_r = 240nm$, $h_e = 70nm$) around $\lambda = 1310nm$. Right: Electron microscope image of the device.

4.2 Gratings with High Directionality

The biggest source of coupling loss experienced by the grating couplers shown in the previous section originated from field scattering into the substrate. The slight asymmetry in vertical direction of the grating coupler achieved an upward diffraction of a slight majority of optical power. In this section the directionality of the grating coupler is further increased through the introduction of an mono crystalline epitaxial silicon layer on top of the grating. A sketch of the structure is depicted in figure 4.5.

In contrast to work presented in [21, 75], where poly-crystalline silicon and amorphous silicon are used for the enhancement of the grating's directionality, a grown mono-crystalline silicon overlay is employed, which avoids lossy materials as p-Si and a-Si. The improvement generated from an increased waveguide height is mainly caused by an upward momentum, that the waveguide mode experiences at the interface between the regular waveguide of height h_{wg} and the grating area of height $h_{wg} + h_{epi}$. Theoretically, this effect can also be achieved by reducing the waveguide height instead of increasing the height of the grating coupler, as will be shown in the section 4.3. In addition, due to the higher asymmetry in vertical direction compared with standard grating couplers without any overlay, constructive interference of fields diffracted from each grating period can potentially be achieved in the upward direction, while at the same time destructive interference will occur for fields diffracted toward the substrate.

The aim of this section is to design one dimensional grating couplers with a high coupling efficiency while maintaining a low scattering angle φ. The reason for the choice of a low scattering angle is to alleviate the computationally demanding optimization of two dimensional grating couplers, that will be presented in chapter 5. For symmetry reasons the diffraction angle needs to be very small, to avoid polarization dependent loss.

Figure 4.6 shows the out-coupled power P_{out}, field overlap η and coupling angle φ for gratings as shown in figure 4.5 as a function of design parameters. The parameters were varied from $w_g = 150nm$ to $w_g = 450nm$, $w_r = 150nm$ to $w_r = 450nm$, $h_{epi} = 100nm$ to $h_{epi} = 180nm$ and $h_e = 120nm$ to $h_e = 270nm$ in 10nm steps, totaling to 138384 simulations. The plots are maximized over the etch depth h_e, so

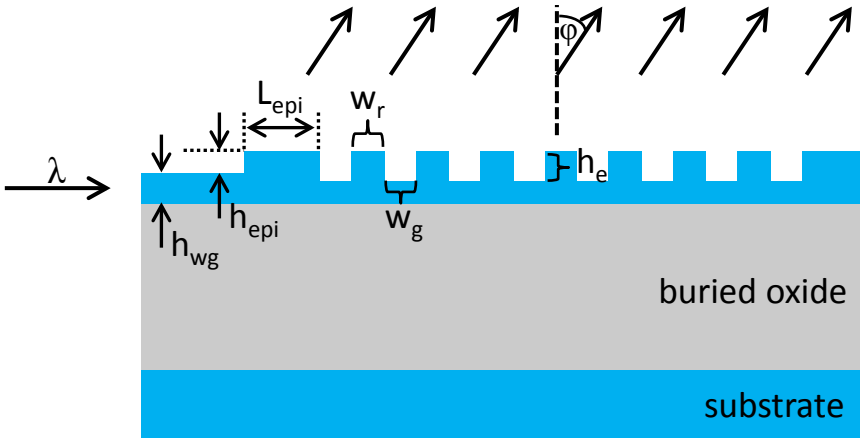

Figure 4.5: Sketch of a grating structure with epitaxial layer of height h_{epi} on top of the waveguide into which the grating is etched.

that only three of the four independent parameters are visible. The figures show at each point the values for optimal coupling with any etch depth and coupling angle. Since the etch depth mainly defines the grating strength, it is reasonable to assume, that the deeper the etch depth the higher the out-coupling efficiency P_{out}. However, having a high out-coupling efficiency in a uniform grating implies a steep increase in scattered field amplitude with respect to the axis of propagation of the waveguide mode and therefore a low overlap with the fiber mode. A tradeoff between out-coupled power and field overlap with the fiber mode is therefore to be expected. Due to the compensation through etch depth implicit in figure 4.6 the overall variation in coupling efficiency as a function of epitaxial layer height appears not as rapid as it would without the implicit optimum etch depths. Nonetheless, a slight increase in out-coupled power can be seen, when the epitaxial layer height is increased, which is accompanied by a decrease in width of the local maxima, rendering the structures less tolerant toward inaccuracies in the manufacturing process. Equally, the region of high field overlap with the fundamental fiber mode is shrinking, but the maximum reachable values do not change significantly. Therefore, the increased performance of uniform gratings with added epitaxial layer over a standard grating coupler stems almost exclusively from the increased directionality. The coupling angle φ does not display a big tolerance towards change in grating period, but as the grating equation 2.8 suggests, the duty cycle has almost no influence on the direction of scattering. Thus the diffraction angle φ is only changing along the main diagonal of the figures shown. A high coupling efficiency at low diffraction angle may be achieved, when the regions of high out-coupled power P_{out} and high field overlap η overlap with the grating period Λ, that provides the desired diffraction angle φ. A good value for the epitaxial layer height, that allows for these requirements to be fulfilled, is $h_{epi} = 150nm$. The lower bound of diffraction angles, that allow for a high field overlap with a fiber mode is $\varphi \approx 6°$, since below that angle first the out-coupled power drops to a local minimum, before increasing again in a different diffraction order and at even lower angles the field overlap vanishes. The grating period, that finds its optimal coupling angle at $\varphi = 6°$ is $\Lambda = 590nm$. In the previous section for standard gratings a duty cycle of 0.5 was chosen. But figure 4.6 indicates, that a higher performance may be achieved with larger duty cycles, since both the maximum in out-coupled power and field overlap are shifted towards

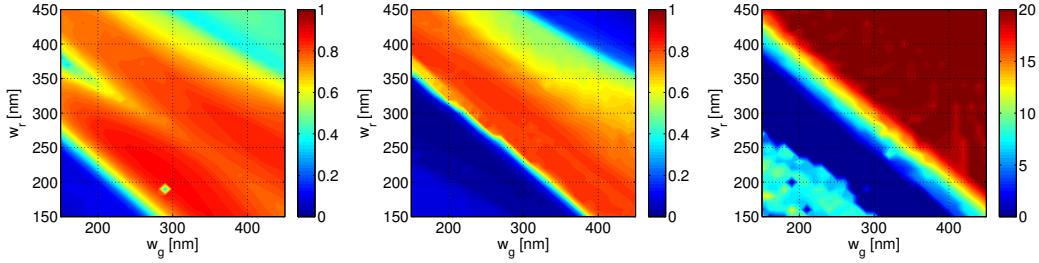

(a) Epitaxial layer height $h_{epi} = 100nm$.

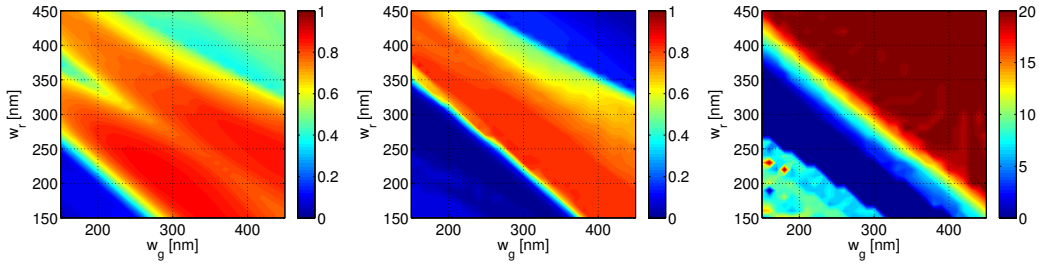

(b) Epitaxial layer height $h_{epi} = 120nm$.

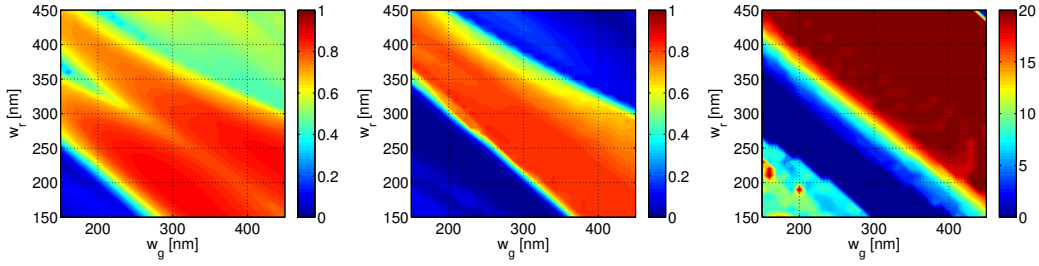

(c) Epitaxial layer height $h_{epi} = 140nm$.

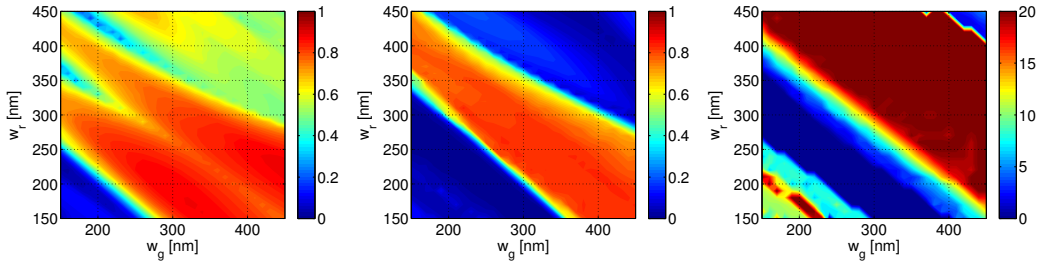

(d) Epitaxial layer height $h_{epi} = 160nm$.

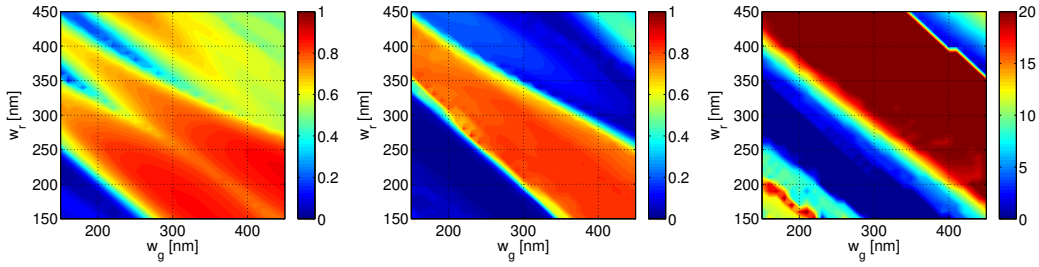

(e) Epitaxial layer height $h_{epi} = 180nm$.

Figure 4.6: Performance plots of gratings with added epitaxial layer as a function of groove width w_g and ridge width w_r for five different epitaxial layer heights h_{epi} at $\lambda = 1.55\mu m$ ($L_{epi} = w_r$). Left: P_{out}, middle: Field overlap η, right: Coupling angle φ in degree.

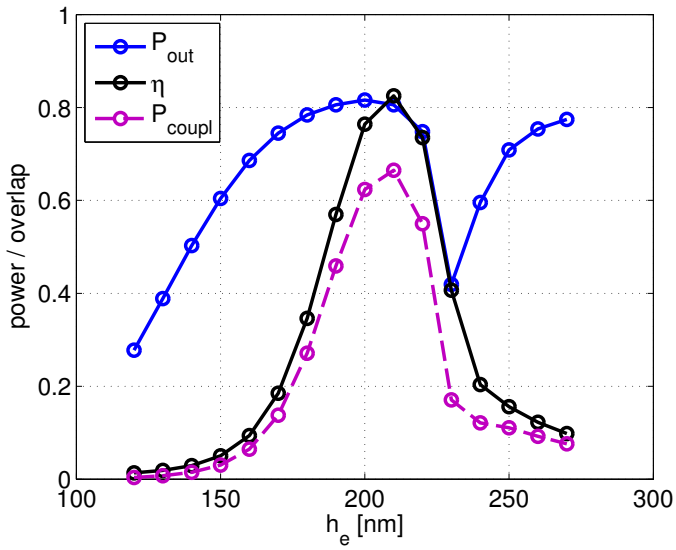

Figure 4.7: P_{out}, η and P_{coupl} at $\varphi = 6°$ as a function of etch depth h_e for a grating of $w_g = 360nm$, $w_r = 230nm$ and $h_{epi} = 150nm$ ($\lambda = 1.55\mu m$).

large groove widths w_g and small ridge widths w_r. A duty cycle of $d = \frac{w_g}{w_g+w_r} \geq 0.6$, translating to $w_g = 360nm$ and $w_r = 230nm$ yields reasonable coupling efficiencies. The dependency of the performance on the etch depth h_e is shown in figure 4.7.

While the out-coupled power P_{out} has its maximum at an etch depth of $h_e = 200nm$, the overlap with the fiber mode shows best performance at $h_e = 210nm$. Since the increase in overlap from $h_e = 200nm$ to $h_e = 210nm$ is higher than the drop in P_{out} over the same etch depth, the overall maximum in coupling efficiency $P_{coupl} \approx 0.66$ is found at $h_e = 210nm$ etch depth. The coupling spectrum can be seen in figure 4.8. It should be noted, that without the oxide cladding of height $h_c = 1.3\mu m$, that covers the whole device, the coupling spectrum is not changed significantly. The only difference is a slight decrease of diffraction angle from $\varphi = 6°$ to $\varphi = 4.5°$. The same effect with a similar magnitude can be seen in standard

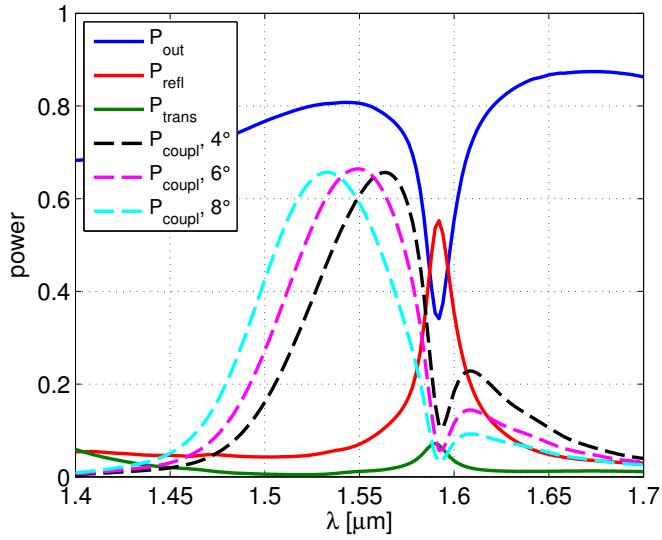

Figure 4.8: Coupling spectrum of a grating with added epitaxial layer of height $h_{epi} = 150nm$ ($w_g = 360nm$, $w_r = 230nm$, $h_e = 210nm$).

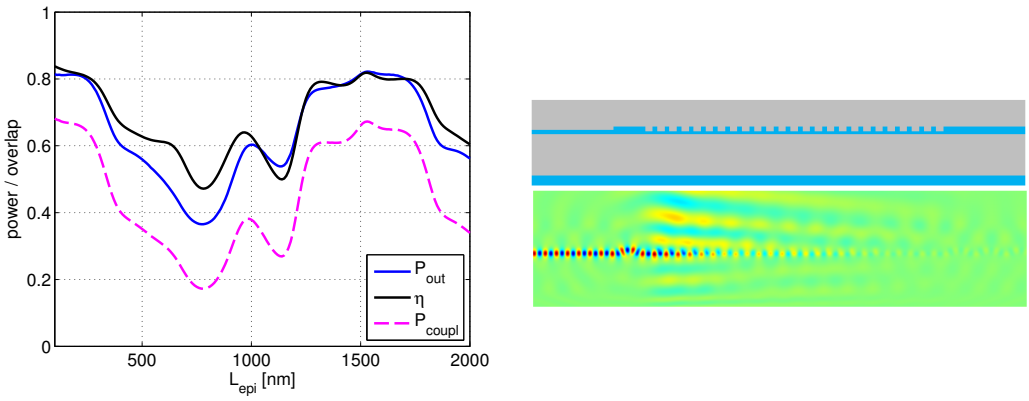

Figure 4.9: Left: Performance (P_{out}, η and P_{coupl}) of a grating with $w_g = 360nm$, $w_r = 230nm$, $h_{epi} = 150nm$ and $h_e = 210nm$ as a function of extension length over the grating region L_{epi} at $\lambda = 1.55\mu m$. Right: Geometry and Electric field of the device with $L_{epi} = 1.53\mu m$.

gratings, which also display a diffraction angle, that is around 2° lower, when the oxide cladding is removed. If therefore a very low diffraction angle φ is the goal of optimization, a grating without cladding yields preferable properties.

An additional dimension for optimization is the amount of epitaxial layer, that extends over the grating onto the waveguide. It is unreasonable to assume, that a material growth can be achieved, which has straight vertical boundaries and does not affect its surrounding. Therefore, an investigation of the influence of this parameter on the performance of the grating is shown in figure 4.9. As can be seen, without proper control over the extension length L_{epi}, the performance of the grating can be severely impacted. The previously assumed $L_{epi} = w_r = 230nm$ does not represent the global maximum of the coupling efficiency, but is not far from it in terms of performance. With extension lengths L_{epi} lower than 120nm the coupling efficiency can be further improved by approximately 3%, but the fabrication of features of such small size is problematic. More tolerant in this regard is an extension length $L_{epi} = 1530nm$, which still offers a slight improvement over the previously assumed value, but does not pose a problem manufacturing wise. The new geometry of the device and the electric field distribution are shown in figure 4.9. The additional material allows for half a wavelength overtone of the incoming field before it comes into contact with the grating and thus ensures, that the field is pushed into the lower region of the waveguide, giving the field the upward momentum mentioned earlier.

4.2.1 Measurement

The result of a transmission measurement of the gratings with epitaxial layer can be seen in figure 4.10. The different curves represent results from three different measurements on identical grating couplers, but varying waveguide lengths. The data are already normalized to a fiber to fiber reference measurement and waveguide losses are subtracted. The depicted performance represents a single grating coupler.

Once again the measured results are in excellent agreement with the simulations shown in the previous section. The peak performance amounts to $P_{coupl} = -1.7$dB around $\lambda = 1.55\mu m$ and drops off sharply at wavelength longer than $1.56\mu m$. For shorter wavelengths the coupling efficiency remains high over a large range and

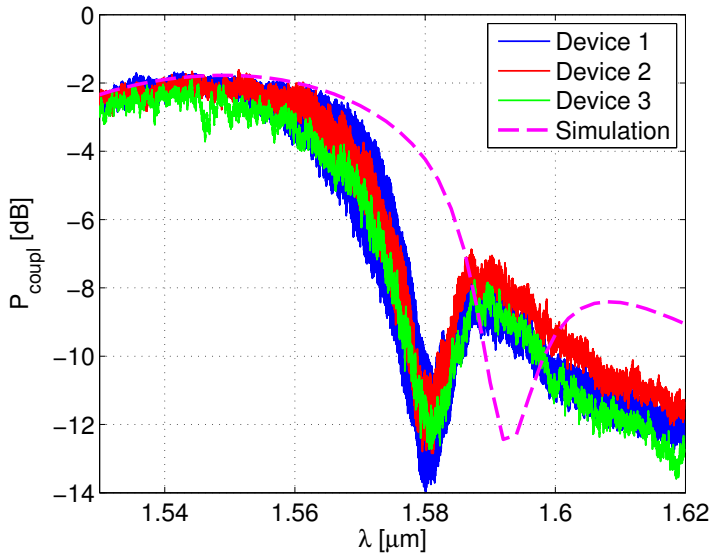

Figure 4.10: Measured performance of a grating coupler ($w_g = 360nm$, $w_r = 230nm$, $h_e = 210nm$, $h_{epi} = 150nm$, $w_{wg} = 12\mu m$) around $\lambda = 1.55\mu m$ with a fiber tilt angle of $\varphi = 6°$ for three different devices of identical constitution.

starts to decrease lightly beyond $1.54\mu m$ wavelength. As found in the simulation, the wavelength $\lambda = 1.58\mu$m marks the transition to another diffraction order and therefore exhibits a minimum in coupling efficiency, which is due to a low out-coupled power at that point. The -1dB bandwidth amounts to 25nm and is therefore comparable to standard grating couplers, as e.g. shown in section 4.1.

Figure 4.11 shows an electron microscope image of the device measured before the application of the oxide cladding and a cross sectional view of the finished device in a pseudo color illustration highlighting the material composition of the structure. One can clearly recognize the nitride layers (purple), that stem from the co-integration process with electronic devices, as mentioned in chapter 3.1. Due to their shallow thickness (approximately 45nm on the grating ridges and below 10nm over the oxide cladding) and low index contrast to the oxide cladding, their influence on the grating performance is negligible.

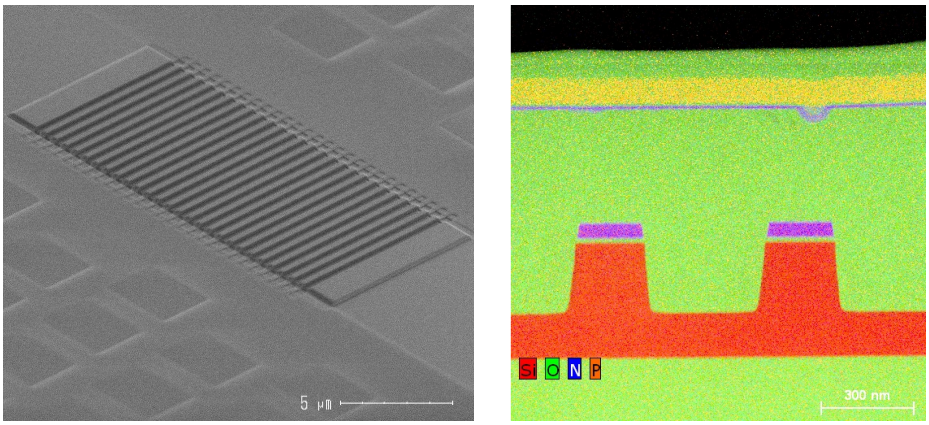

Figure 4.11: Electron microscope image of the grating coupler and a cross sectional pseudo color image of the device (Green: SiO_2, red: Si, purple: Si_3N_4, yellow: phosphate glass).

4.3 Improved Overlap

In the previous section a high directionality of the grating coupler and a low scattering angle were the primary concerns. Here, for a better performance in addition to a high directionality the field overlap between diffracted field and fiber mode is optimized. Since the field overlap has an equally large influence on overall coupling efficiency, the gain from an improved overlap is very large. In contrast to gratings presented before, in this section a 400nm waveguide height is assumed, as the gratings were originally designed for use with doped waveguides in a diode structure, that required a waveguide height larger than the traditional 220nm.

To illustrate the problem figure 4.12 shows the normalized electric field amplitudes of the scattered field of a standard grating coupler and a fiber mode. To obtain a high overlap between these two fields, they have to exhibit a similar shape in amplitude and phase. The phase is adjusted mostly through the grating period as indicated by the grating equation 2.8 and the amplitude through the grating strength (i.e. the etch depth).

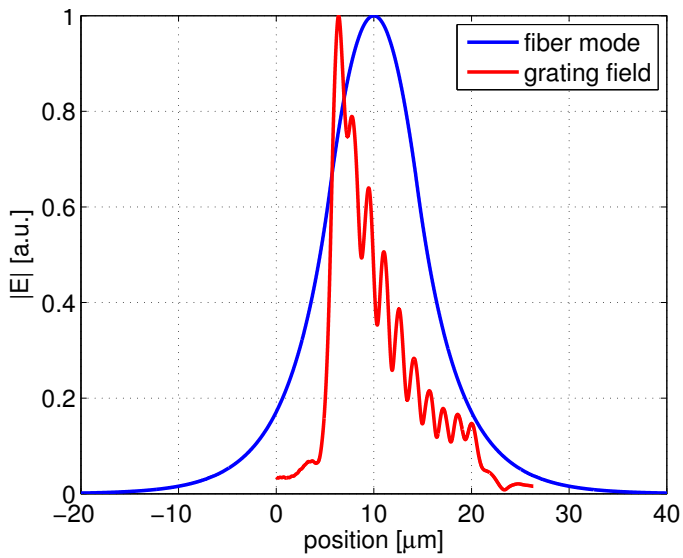

Figure 4.12: Absolutes of the normalized electric field amplitudes of a standard fiber grating coupler (red) and a fiber mode (blue) at $\lambda = 1.55\mu m$.

It can be seen, that the rise in amplitude of the diffracted field from the grating is much steeper than the rise in amplitude exhibited by the fiber mode. One could therefore conclude, that this problem can be reduced with weaker gratings. However, this solution would reduce the directionality of the grating and therefore impair the overall performance. Therefore another solution, which results in softer rise of field amplitude over the grating without affecting its out-coupling efficiency has to be found. This is achieved by introducing a secondary etch step in front of the grating. Several periods of different constitution than those of the actual grating are placed at the beginning of the grating to introduce a low directionality without producing unwanted reflections or losses.

Before finding a working design for the secondary grating periods, a grating, which features a high out-coupling efficiency has to be found. From the previous section it is known, that a silicon epitaxial layer on top of the grating offers an increased directionality over a standard grating. In this section however, the means

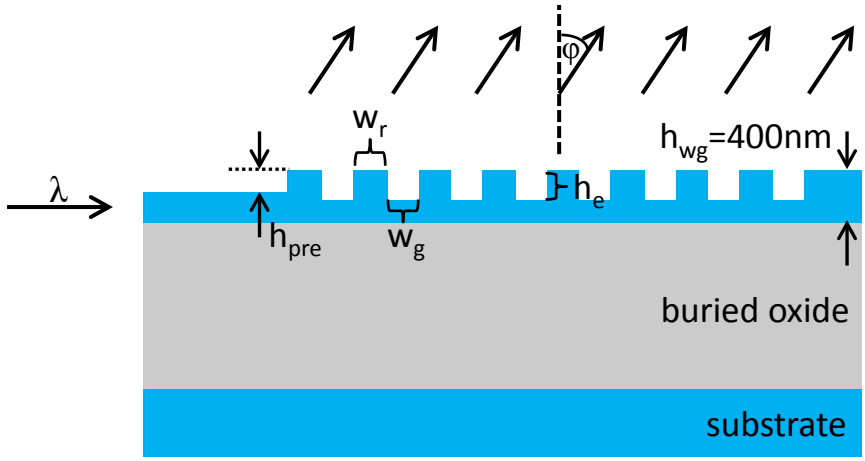

Figure 4.13: Sketch of a grating structure with $h_{wg} = 400nm$ waveguide height. The waveguide height is reduced by h_{pre} in front of the grating to facilitate a higher directionality.

of increasing the directionality is to reduce the waveguide height in front of the grating and leave the grating height as it is. Process-wise this is advantageous as it only requires an etch step instead of a deposition of materials and from a design point of view the dimensions are not much different than the ones seen in previous sections.

Figure 4.14 shows the results of a parameter scan across groove width w_g, ridge width w_r, etch depth h_e and the preliminary etch depth h_{pre}, which reduces the waveguide height in front of the grating (c.f. figure 4.13). For convenience, figure 4.14 only shows results, where only a single etch depth for both etches is used, therefore $h_{pre} = h_e$ is valid for these plots. At later points this assumption is revoked, since with two different etch depths the adaptation of the scattered field from the grating to the fiber mode is achieved. But for now this convention is sufficient to find a suitable groove width w_g and ridge width w_r for the grating on 400nm waveguides.

The parameters were varied in 10nm steps from 350nm to 500nm and from 180nm to 300nm, respectively. The left column of figure 4.14 shows the out-coupling efficiency of the gratings and it is clear that with increasing etch depth, P_{out} increases as well. For large etch depths ($h_e = h_{pre} \geq 240nm$) a saturation is reached and P_{out} remains flat. The second maximum, which becomes visible for large etch depths in the parameter range chosen indicates another diffraction order of the grating, but is not of interest here.

The second column illustrates the field overlap η with the fundamental fiber mode LP_{01} of a sSMF tilted by the angle φ with respect to the surface normal. The overlap is evaluated for angles ranging from $\varphi = 3°$ to $\varphi = 15°$ and is plotted for the angle, which provides the maximum overlap. The third column shows the corresponding fiber tilt angle φ. It is evident, that the region of high overlap for the allowed range of angles moves to larger grating periods with increased etch depth. However, in terms of absolute numbers a drop in η for etch depths $h_e = h_{pre} \geq 240nm$ can be noticed, which is most likely due to a sharper rise in amplitude caused by the stronger grating and therefore a larger mismatch with the fiber mode. Together with the observation, that P_{out} also saturates at this point the first conclusion can

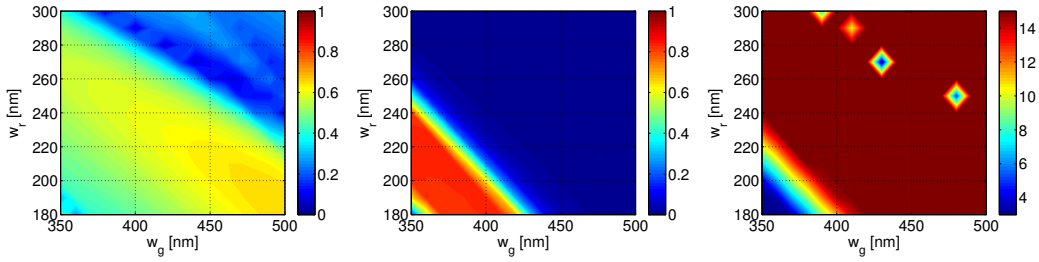

(a) Etch depth $h_e = 180nm$.

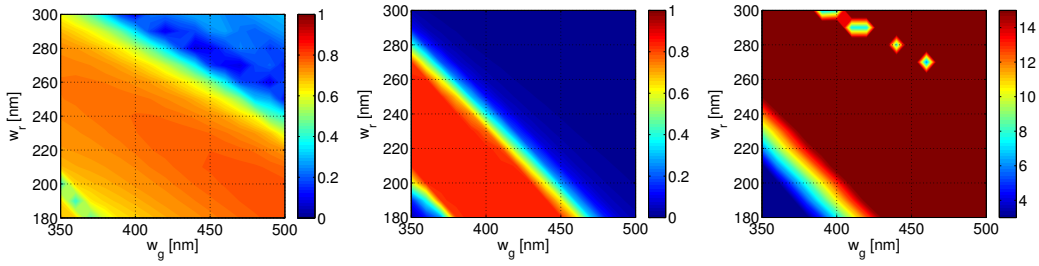

(b) Etch depth $h_e = 200nm$.

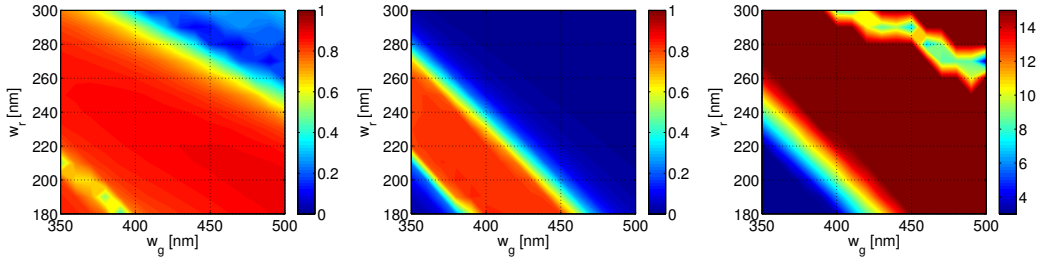

(c) Etch depth $h_e = 220nm$.

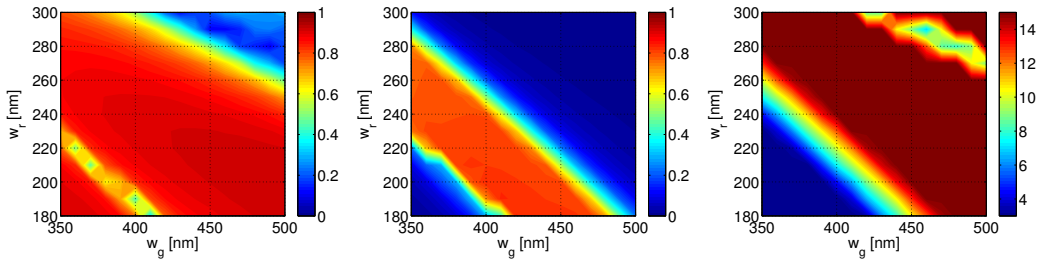

(d) Etch depth $h_e = 240nm$.

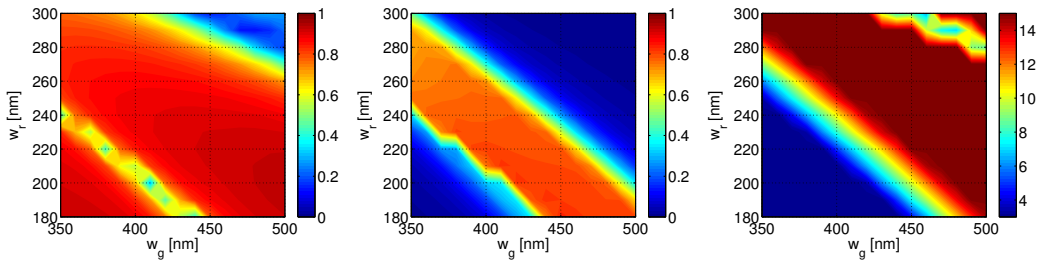

(e) Etch depth $h_e = 260nm$.

Figure 4.14: Performance plots of gratings on 400nm waveguides as a function of groove width w_g and ridge width w_r for five different etch depths at $\lambda = 1.55\mu m$. Left: P_{out}, middle: Field overlap η, right: Coupling angle φ in degree.

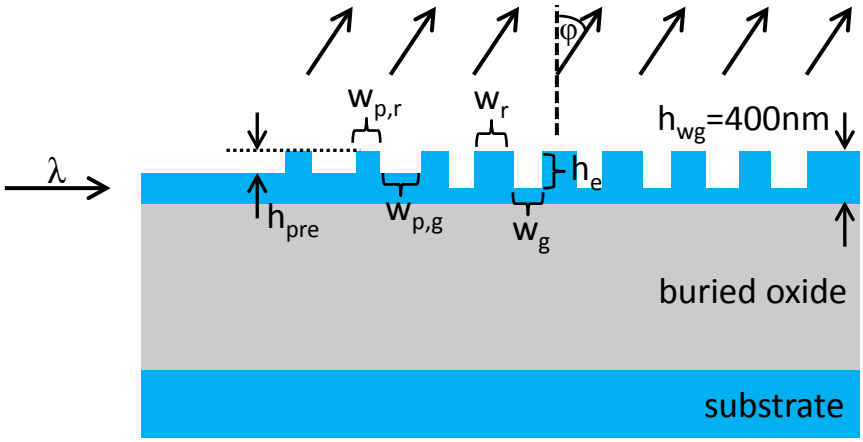

Figure 4.15: Sketch of a grating structure with $h_{wg} = 400nm$ waveguide height. The grating exhibits two different etch steps to increase the field overlap with a fiber mode and a reduced waveguide height in front of the grating.

be reached, that a good etch depth h_e is approximately 240nm.

The other two parameters - grating period Λ and duty cycle or groove width w_g and ridge width w_r - can be chosen with a bit more freedom, as a large range of combinations leads to acceptable results. The grating period determines mostly the diffraction angle φ and should be chosen accordingly. The duty cycle has almost no influence on the diffraction angle. However, it can be seen that for lower ridge widths w_r and therefore larger duty cycles the overlap η and out-coupling efficiency P_{out} increase slightly. The combination $w_g = 440nm$ and $w_r = 200nm$ shows a good performance ($P_{out} = 0.9$, $\eta = 0.81$), while maintaining a reasonable coupling angle ($\varphi = 13.5°$).

Suitable parameters for the secondary etch steps of the preliminary etches can be determined similarly to the ones of the grating itself. Figure 4.15 shows a sketch of such a grating. The values for $w_g = 440$nm, $w_r = 200$nm and $h_e = 240$nm have already been determined and are fixed. Groove width $w_{p,g}$, ridge width $w_{p,r}$ and etch depth h_{pre} of the secondary etches are found by parameter scans once again. The convention of $h_e = h_{pre}$ is no longer valid, but the waveguide is etched by the same amount as the preliminary grating etches, resulting in two different etch depths necessary for the whole grating structure.

The parameters $w_{p,g}$ and $w_{p,r}$ were varied in 10nm steps from 250nm to 500nm and from 100nm to 250nm, respectively. The etch depth h_{pre} was scanned from 150nm to 250nm in 10nm steps as well. Figure 4.16 shows the performance plots for a single etch depth of $h_{pre} = 180nm$. The considerations on etch depth are the same as before, however, since the out-coupling efficiency P_{out} of the grating is already determined by the parameters found before, the magnitude of h_{pre} plays a less significant role. Nonetheless, a small decrease in field overlap η can be observed, when moving to larger etch depths, while the optimal grating period shifts to larger values. The out-coupling efficiency P_{out} increases with larger etch depth similar to gratings seen before. Therefore a compromise between η and P_{out} has to be reached, for which $h_{pre} = 180nm$ proved to be well suited.

The other two values to be determined $w_{p,g}$ and $w_{p,r}$ exhibit a minor influence on P_{out}, since it remains high over a large area. However, the field overlap η is very much dependent on these parameters and shows a maximum for large $w_{p,g}$ and small

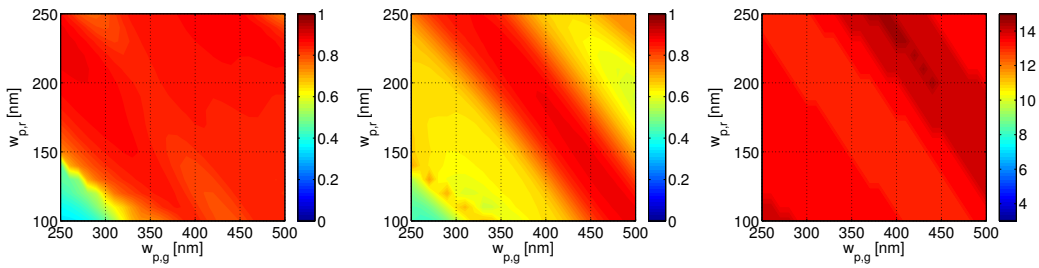

Figure 4.16: Performance plots of gratings on 400nm waveguides as a function of preliminary etch parameters groove width $w_{p,g}$ and ridge width $w_{p,r}$ for etch depth $h_{pre} = 180nm$ at $\lambda = 1550nm$ ($w_g = 440nm$, $w_r = 200nm$, $h_e = 240nm$). Left: P_{out}, middle: Field overlap η, right: Coupling angle φ in degree.

$w_{p,r}$, right at the border of the domain depicted. An even further increased η might be possible, when allowing for $w_{p,r} < 100nm$, but such values might be problematic in terms of fabrication. Therefore, the values $w_{p,g} = 500nm$ and $w_{p,r} = 100nm$ yield best results, while maintaining easy manufacturability. Additionally, the coupling angle φ (c.f. figure 4.16, right) is not affected by the introduction of secondary etch steps, as it remains at $\varphi = 13.5°$.

After the optimization of $w_{p,g}$, $w_{p,r}$ and h_{pre} the number of preliminary periods has to be determined. Figure 4.17 shows the overlap of diffracted fields of grating couplers with different amount of secondary periods in front of it with the fundamental fiber mode of a sSMF. It can be seen, that the overlap is indeed rising with the number of secondary grating periods until a maximum is reached. The optimal number of secondary grating periods is largely dependent on the spot size of the fiber mode, as it dictates the optimal slope for the out-coupled field along the axis of propagation of the grating. For a spot size of $w_0 = 5.5\mu m$ the optimal amount of

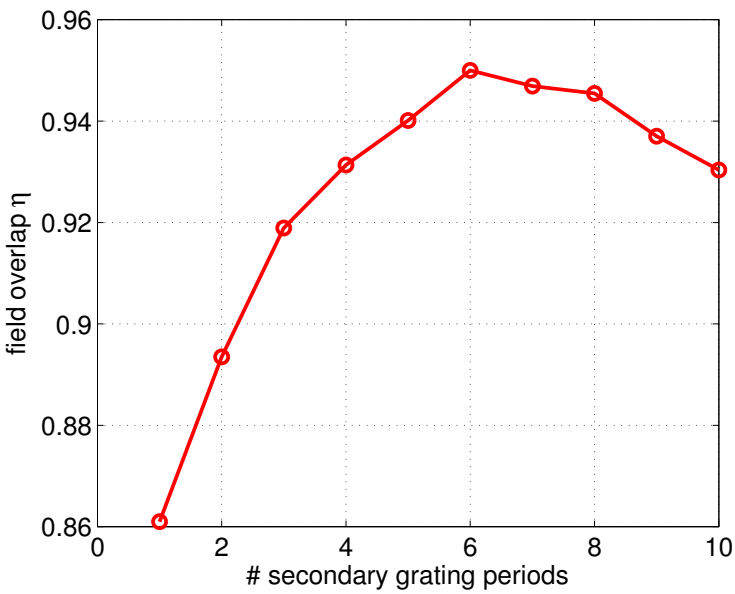

Figure 4.17: Field overlap between LP_{01} mode of a sSMF and diffracted field of a grating on a 400nm waveguide with two different etch steps as a function of the number of secondary grating periods in front of the grating at $\lambda = 1.55\mu m$. ($w_g =$ 440nm, $w_r =$ 200nm, $h_e =$ 240nm, $w_{p,g} =$ 500nm, $w_{p,r} =$ 100nm, $h_{pre} =$ 180nm)

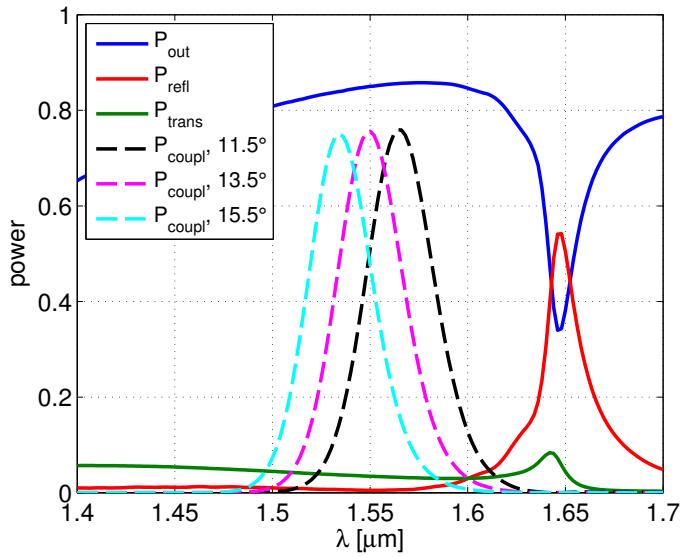

Figure 4.18: Coupling spectrum of a fiber grating coupler on a 400nm high waveguide with two different etch depths and reduced preliminary waveguide height (w_g = 440nm, w_r = 200nm, h_e = 240nm, $w_{p,g}$ = 500nm, $w_{p,r}$ = 100nm and h_{pre} = 180nm).

secondary grating periods is 6, after which the overlap and therefore the coupling efficiency is decreasing again. It is apparent, that the grating can be adapted to other spot sizes as well, simply by varying the amount of secondary etch steps. The limit to this method can be found by evaluating the slopes of a diffracted field of a grating with zero secondary grating periods (c.f. figure 4.12). For optimal coupling the slopes of the field amplitude on both sides of its maximum have to be equal. The declining slope on the right hand side of the maximum is determined by the grating itself, to which the secondary grating periods adapt the increasing part of the electric field amplitude on the left hand side of the amplitude maximum. Using shallow etches in the preliminary grating and deep etches in the original grating will therefore result in a more symmetrical diffracted field and hence a higher overlap with the fiber mode.

The performance of the grating over wavelength is shown in figure 4.18. At the center wavelength of $\lambda = 1.55\mu m$ the optimal coupling angle is $\varphi = 13.5°$ as found before. The effect on coupling efficiency through a small variation in φ is very small. By changing the coupling angle by 2° the coupling efficiency changes by less than 1%, but the central wavelength drifts by $\Delta\lambda \approx \pm 15nm$, where a larger angle causes a shift to lower wavelengths and a smaller angle results in a higher central wavelength, similar to the gratings seen in previous sections. Reflected power and transmitted power are with 0.5% and 3.5%, respectively quite low at $\lambda = 1.55\mu m$ and do not change significantly over a large spectrum. The overall coupling efficiency amounts to -1.4dB.

4.3.1 Taper Structure for the Reduction of Waveguide Height

An additional difficulty not mentioned so far is the problem of reducing the waveguide height in front of the grating from $h_{wg} = 400nm$ to $h_{wg} = 220nm$ without introducing additional losses. This can be achieved by a taper structure as shown in figure 4.19, where a rib waveguide is gradually transformed into a nano wire.

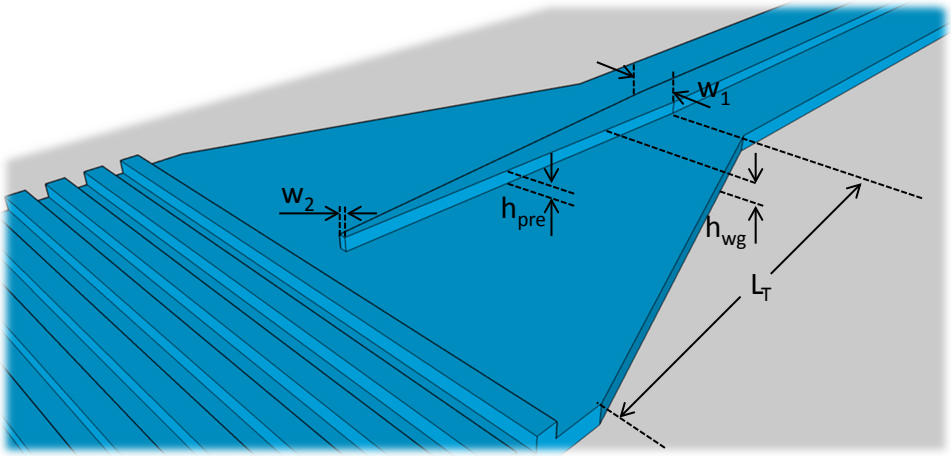

Figure 4.19: Taper structure for the simultaneous reduction of waveguide height h_{wg} and increase in waveguide width w_{wg}.

Instead of reducing the height of the waveguide continuously, which would be difficult to manufacture, the width of the rib is minimized and the incoming mode is gradually pushed into the slab region through the reduction of the rib width from w_1 to w_2. At the same time the slab region is widened to facilitate coupling to the grating coupler. This way the taper that is used in front of every grating anyhow can be combined with the taper that reduces waveguide height. An adiabatic taper can certainly be achieved, if the width w_2 of the tip of the rib at the end of the taper is very thin, resulting in a high overlap between fundamental modes in rib waveguide and nano wire and the taper length L_T is very large, which reduces the coupling between modes in the taper.

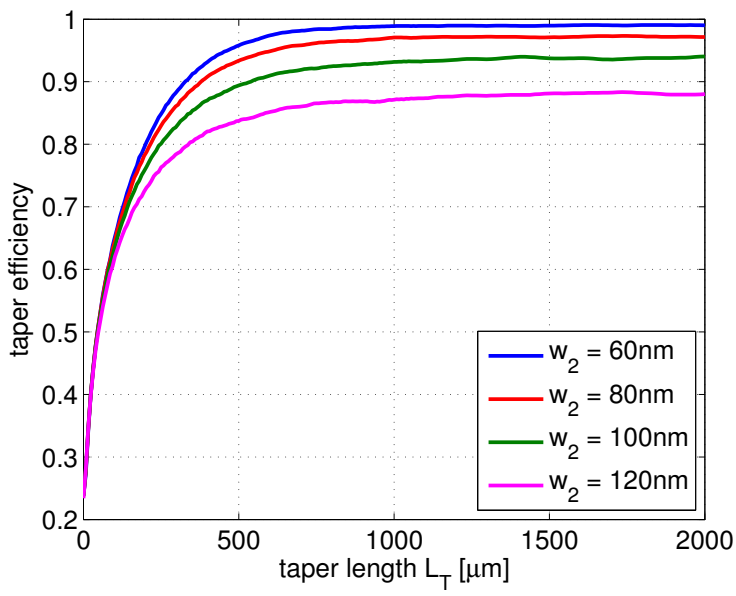

Figure 4.20: Coupling efficiency between the fundamental waveguide mode of a rib waveguide with rib width $w_{wg} = w_1 = 750nm$, waveguide height $h_{wg} = 400nm$ and etch depth $h_e = h_{pre} = 180nm$ and the fundamental mode of a nano wire of $h_{wg} = 200nm$ and $w_{wg} = 10\mu m$ in a taper of length L_T as shown in figure 4.19 at $\lambda = 1.55\mu m$.

However, the same technological constraints, which were relevant for the critical dimensions in the grating structures are valid here as well, thus limiting the minimum width w_2 of the rib. The taper length L_T is less challenging as several millimeter length do not pose a problem. Figure 4.20 illustrates the performance of such a taper as a function of taper length for four different minimum rib widths w_2 obtained through a simulation using Eigenmode Expansion.

With a width of $w_2 = 60nm$ the taper structure provides a nearly lossless conversion from the fundamental TE mode of the rib waveguide to the fundamental mode of a $10\mu m$ wide nano wire. The efficiency falls to 97% if w_2 is widened to $80nm$. For larger rib widths it decreases even further to 88% in the case of $w_2 = 120nm$. A taper length of $L_T \geq 1000\mu m$ seems to be sufficient for any rib width in the order of magnitude depicted in figure 4.20, as the curves have reached saturation at this point.

4.4 Optimal Gratings

As mentioned before the efficiency of a fiber grating coupler is primarily determined by two values: Out-coupled power and overlap with the fiber mode. In the first section of this chapter a grating design, which features a high directionality, was presented. Later considerations to improving the field overlap between the scattered field and the fundamental fiber mode of a standard single mode fiber while maintaining a high directionality of a grating on a 400nm waveguide basis were made. In this section grating designs with even further improved characteristics are presented.

4.4.1 Theoretical Considerations

In an undisturbed waveguide, which lies in the xy-plane of a Cartesian coordinate system, the electric field of the fundamental waveguide mode is described by

$$\vec{E}_{wg}(x, y, z) = \vec{E}_0(x, y) \exp(-i\,\beta z). \tag{4.1}$$

For convenience the time dependent term $\exp(i\,\omega t)$ is omitted. β is the phase constant of the mode and can be expanded to

$$\beta = n_{eff} \frac{2\pi}{\lambda}, \tag{4.2}$$

in which the effective refractive index $n_{eff} = n_1 - i\,n_2$. Ideally the imaginary part of n_{eff} is zero, which makes the waveguide lossless. If that is not the case the field is decaying exponentially along the z-direction. The power of the electric field in the waveguide along the axis of propagation is then proportional to the absolute of the exponential term of equation 4.1 squared

$$\begin{aligned} P_{wg}(z) &\propto |\exp(-i\,\beta z)|^2 \\ &\propto |\exp(-2i\,\beta z)| \\ &\propto |\exp(-i\frac{4\pi}{\lambda}(n_1 - i\,n_2)z)| \\ &\propto \exp(-n_2\frac{4\pi}{\lambda}z)|\exp(-i\frac{4\pi}{\lambda}n_1 z)|. \end{aligned} \tag{4.3}$$

Since the last term in equation 4.3 is always unity it can be omitted. The power in a lossy waveguide is therefore decreasing exponentially, provided the imaginary part of n_{eff} is constant. If that is not the case a more general term for the distribution of power along the z-axis must be considered, where the imaginary part of the optical path is integrated over the whole waveguide. Assuming that the initial power in the waveguide at $z = -\infty$ is normalized, 4.3 changes to

$$P_{wg}(z) = \exp(-\frac{4\pi}{\lambda} \int_{-\infty}^{z} n_2(z')\, dz'). \tag{4.4}$$

Complementary, the power that is lost to the waveguide up until position z is

$$\begin{aligned} P_{loss}(z) &= 1 - P_{wg}(z) \\ &= 1 - \exp(-\frac{4\pi}{\lambda} \int_{-\infty}^{z} n_2(z')\, dz'). \end{aligned} \tag{4.5}$$

From here on one must pay attention to the meaning of n_2. By convention the imaginary part of the effective refractive index is used to describe absorption loss (or gain) of the waveguide mode. However, the meaning here is a different one. Through a perturbation of the waveguide power is lost due to scattering of the electric field at a discontinuity. The power is not lost in the sense that it is absorbed by carriers but it is no longer guided in a mode of the unperturbed waveguide. A better term for the description of P_{loss} would be power outside the waveguide mode rather than lost power. If lossy materials are present an additional imaginary part in n_{eff} must be regarded, which does not necessarily show the same z-dependence as n_2. Applying this approach to the fiber grating coupler, the question to be answered is, how n_2 and therefore how the perturbation of the waveguide needs to be constituted, so that the profile of the scattered field resembles that of a fiber mode. Since the fundamental fiber mode can be approximated with a Gaussian distribution, P_{loss} must take the same form. One can therefore postulate

$$\frac{d}{dz} P_{loss}(z) = \frac{2}{\omega_0 \sqrt{2\pi}} \exp(-2\frac{z^2}{w_0^2}), \tag{4.6}$$

where w_0 is the spot radius of the Gaussian distribution and the factor $\frac{2}{\omega_0\sqrt{2\pi}}$ provides for unity power after integration. Integration with respect to z yields

$$P_{loss}(z) = 1 - P_{wg}(z) = \frac{2}{\omega_0 \sqrt{2\pi}} \int_{-\infty}^{z} \exp(-2\frac{z'^2}{w_0^2})\, dz'. \tag{4.7}$$

The integral on the right hand side is solved by the error function. By assuming w_0 to be positive and substituting equation 4.4 for $P_{wg}(z)$, equation 4.7 can be written as

$$1 - \exp(-\frac{4\pi}{\lambda} \int_{-\infty}^{z} n_2(z')\, dz') = \frac{1}{2}(1 - \mathrm{erf}(\frac{\sqrt{2}z}{w_0})). \tag{4.8}$$

Equation 4.8 can now be solved for $n_2(z)$ by assuming $\lim_{n \to -\infty} n_2(z) = 0$:

$$n_2(z) = \frac{\sqrt{2}\lambda}{4\pi^{\frac{3}{2}}\omega_0} \cdot \frac{\exp(-2\frac{z^2}{w_0^2})}{\frac{1}{2}(1 - \mathrm{erf}(\frac{\sqrt{2}z}{w_0}))}. \tag{4.9}$$

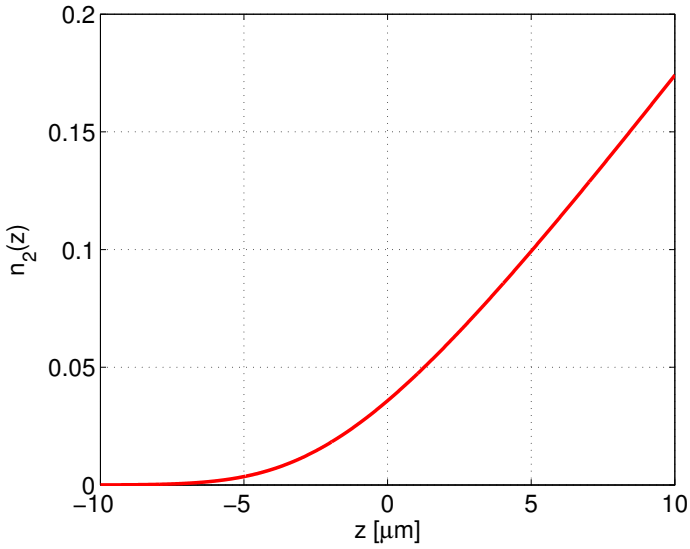

Figure 4.21: Imaginary part of the effective refractive index as a function of propagation length z in a perturbed waveguide necessary for optimal field overlap with a fundamental fiber mode of a sSMF at $\lambda = 1.55\mu m$.

Figure 4.21 shows $n_2(z)$ for optimal coupling to a fiber mode of an approximately Gaussian distribution at $\lambda = 1.55\mu m$. The field waist w_0 was assumed to be $5.5\mu m$. Naturally, $n_2(z)$ extends towards infinity at both ends of z since the ideal fiber mode shows the same behavior. At $z = -\infty$ n_2 tends towards zero, giving a smooth rise to the amplitude of the scattered field. For larger z n_2 shows a linear growth, but can be disregarded for real applications since the power scattered at later stages of the waveguide is negligible. However, it is not clear how a waveguide has to be constituted to show such a loss characteristic. First it is assumed that the scattering losses of the waveguide are continuous, which is not the case for gratings. This can, however, be compensated with a discrete approximation of n_2. Even further problematic is the fact, that simple scatter losses even in the form of equation 4.9 do not ensure the desired high overlap with a fiber mode, since light in a perturbed waveguide does not tend to be scattered solely in one direction. Rather, even in gratings with a high directionality, only a large percentage is scattered towards the fiber. To derive a well performing grating coupler from n_2 one would need to obtain the scattering characteristics of a large amount of different waveguide perturbations, which need to display a high, uniform directionality and negligible reflections.

The real part of n_{eff} also needs to show certain attributes. Figure 4.22 shows a sketch of a fiber grating coupler with discrete uniformly distributed etches at $z = z_0 \ldots z = z_N$. To achieve a high overlap between scattered field and fiber mode the field scattered by the grating needs to have a plane phase front. Therefore, it is necessary that the optical paths for light scattered from the beginning of the grating at $z = z_0$ to the fiber and from every other discrete location $z = z_i$ are equal or differ by multiples of 2π. According to equation 4.1 this phase condition can be expressed as

$$-i\,\frac{2\pi}{\lambda} n_1 \Delta z = -i\,\frac{2\pi}{\lambda} n_c \Delta x - i\,m 2\pi, \tag{4.10}$$

where n_c is the refractive index of the cladding material and Δx is the vertical distance between waveguide and fiber. It is more convenient to express Δx in terms

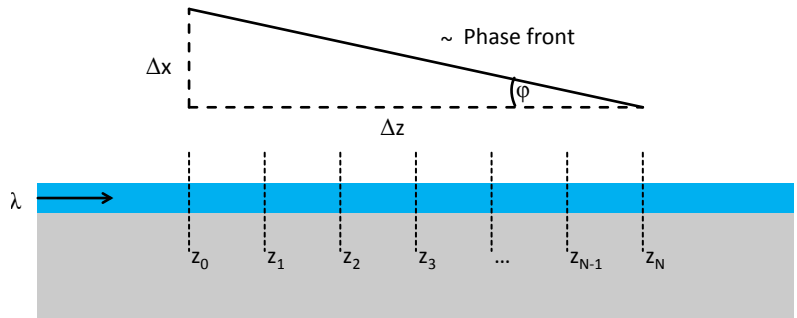

Figure 4.22: Sketch of optical path differences in a grating coupler.

of fiber tilt angle. Equation 4.10 can thus be solved for n_1:

$$n_1 = n_c \tan(\varphi) + \frac{m\lambda}{\Delta z} \tag{4.11}$$

In the usual environment of fiber grating couplers the effective refractive index of the waveguide mode is larger than the refractive index of the cladding material. It is therefore not feasible to achieve near vertical coupling in a grating of the order $m = 0$. Under this condition only for larger angles $\varphi > 45°$, when the tangent becomes larger than 1, equation 4.11 can be satisfied. As a consequence, having a grating with continuous loss characteristics as called for in the imaginary part of n_{eff} for an optimal distribution of the intensity profile is not achievable. The additional phase delay between grating periods is unavoidable for near vertical coupling. Equation 4.11 is of course again a representation of the grating equation 2.3, but better suited for the description of a fiber grating coupler from the design point of view.

The complete effective refractive index of an optimal fiber grating coupler is

$$\begin{aligned} n_{eff} &= n_1 - i\, n_2 \\ &= n_c \tan(\varphi) + \frac{m\lambda}{\Delta z} - i\,\frac{\lambda}{4\pi} \cdot \frac{\exp(-2\frac{z^2}{w_0^2})}{1 - \frac{1}{4}\sqrt{2\pi} w_0 (1 + \mathrm{erf}(\frac{\sqrt{2}z}{w_0}))}. \end{aligned} \tag{4.12}$$

In uniform gratings Δz is constant and can therefore be replaced by the grating period Λ.

4.4.2 Numerical Preliminary Considerations

In the previous section properties of a waveguide that is ideally suited for a fiber grating coupler were discussed. However, this theoretical view of the matter does not give much specific hints on geometrical features, which would benefit the performance of a grating coupler. In this section a grating coupler, that perturbs a waveguide in such a way that its characteristics largely correspond to equation 4.12 is found by utilizing search algorithms. Since theoretically there are an infinite amount of waveguide geometries, that could be used for scattering light, a complete search over the problem space is not feasible. Rather it is helpful to eliminate as many degrees of freedom as possible before running an automated optimization.

Before considering the substrate the grating coupler is designed for, the technology used for manufacturing of the device dictates certain design rules, which are by

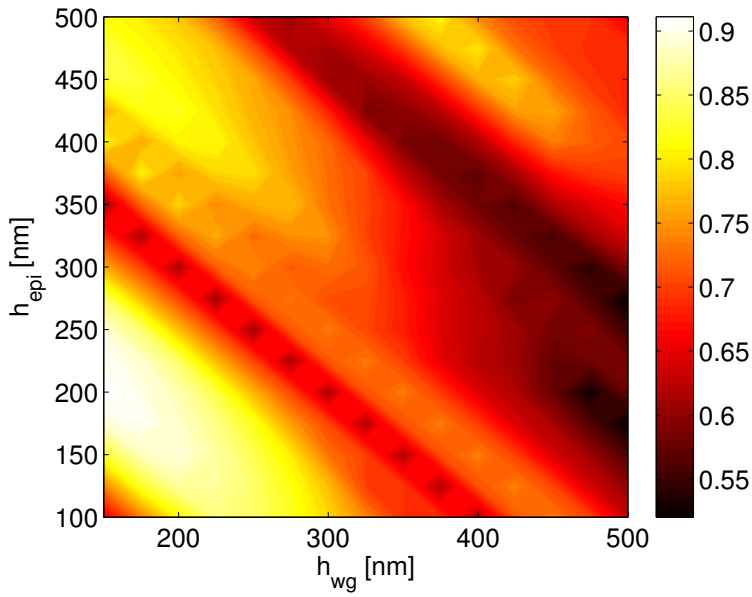

Figure 4.23: P_{out} as a function of waveguide height h_{wg}, epitaxial layer height h_{epi}, etch depth h_e and grating period Λ at $\lambda = 1.55\mu m$. The function is reduced to two dimensions by maximization over h_e and Λ.

no means constraints to the search space the optimization algorithm is running on. For example, grating grooves are strictly vertical as standard etch processes do not allow for arbitrary etch shapes. V-, sinusoidal, slanted grooves, etc. are therefore forbidden designs. In terms of dimension, horizontal feature sizes below 100nm are also not feasible. Although certainly possible using state of the art lithography, for the majority of microchip manufacturers structures smaller than this size are difficult to achieve using standard (DUV) lithography.

For the choice of a suitable substrate for high efficiency grating couplers earlier considerations are taken into account. To achieve a high directionality an epitaxial layer on top of the grating is used. If not fixed to 220nm waveguide height, many combinations of design parameters are feasible, for which efficient grating couplers can be implemented. Figure 4.23 shows the out-coupled power P_{out} independent of mode coupling (i.e. only the fraction of power that is diffracted by a grating in the upwards direction) of fiber grating couplers in dependence of waveguide height h_{wg}, epitaxial layer height h_{epi}, etch depth h_e and grating period Λ. The function is maximized over Λ and h_e so that only waveguide height and epitaxial layer height remain on the x- and y-axis, respectively. The wavelength, for which the simulations took place, is $\lambda = 1.55\mu m$. The ranges, in which the four design parameters were varied are $h_{wg} = 150nm \ldots 500nm$, $h_{epi} = 100nm \ldots 500nm$, $h_e = 10nm$ to the available total waveguide height $h_{wg} + h_{epi}$ and $\Lambda = 500nm \ldots 800nm$. The duty cycle was fixed to 0.5 and the number of grating periods was 25. Overall, the number of simulations making up figure 4.23 amount to 89250. First to notice are multiple maxima in P_{out}, which can provide gratings with high fractions of out-coupled power (80% and above). These maxima correspond to different orders of refraction, as seen in plots in previous sections. Therefore, only one of the three visible maxima can provide for near vertical coupling, as the scattering angles φ connected with the other two are too large. The maximum in the bottom left corner is the one, which comprises gratings of orders $m = -1$. This circumstance

is fortunate for two reasons: First, it is also the global maximum, which means it potentially yields the highest efficiencies and second, it is located near the usual dimensions of grating couplers widely available, which implies that technology-wise no major adjustment is necessary. The absolute maximum of figure 4.23 is located at the lowest waveguide heights. Therefore, one could claim the lower the waveguide height, the higher the grating efficiency. However, it must be considered, that low waveguide heights also introduce additional loss due to worse field confinement and higher intensities at waveguide edges, which will lead to more losses caused by rough surfaces. Here a waveguide height of $h_{wg} = 200nm$ and epitaxial layer height of $h_{epi} = 200nm$ are chosen. This combination of parameters still shows a high fraction of out-coupled power ($P_{out} > 85\%$) and can be achieved through either growth on 200nm waveguides or etching of 400nm waveguides. Additionally, both substrates are commercially available and CMOS compatible.

4.4.3 Optimization Using Search Algorithms

In the previous section two design parameters h_{wg} and h_{epi} were derived from a rigorous search over a large parameter space. These two parameters approximately determine the maximum out-coupled power P_{out}. However, having a large P_{out} by itself does not guarantee a high coupling efficiency, since a high overlap with a fiber mode still needs to be established. To find values for the rest of the so far undetermined design parameters, two search algorithms were implemented for the optimization of fiber grating couplers on the given substrate. Figure 4.24 shows a sketch of a grating design to be optimized. The grating is 24 periods long and consists of random grooves and ridges. The design parameters describing each period i are groove width $w_{g,i}$, ridge width $w_{r,i}$ and etch depth $h_{e,i}$. Since each period can be changed independently, the overall search space has 72 dimensions. Given today's computational power, it is not viable to employ traditional optimization algorithms, that rely on the knowledge of derivatives along each degree of freedom, for problems of that size. One can imagine, that an exhaustive search over a space with a large amount of dimensions can not be finished within a reasonable time. It is evident,

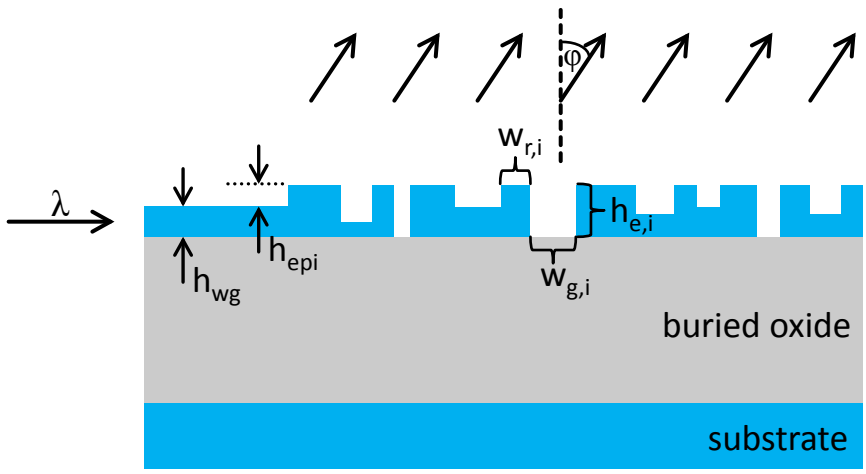

Figure 4.24: Sketch of a grating structure with random etches. Each period i is independently described by three parameters: groove width $w_{g,i}$, ridge width $w_{r,i}$ and etch depth $h_{e,i}$.

that search algorithms that rely on other means than computing the derivative of the function to be optimized along all dimensions on every point examined need to be employed. The so called heuristic procedures are capable of traversing a large parameter space with incomplete knowledge of its shape. Therefore, they are well suited for finding solutions of complex problems, for which the computational cost is too high if approached by traditional optimization methods [76, 77]. Usually, heuristics are limited to specific problems. If applicable to a wider range of problems the distinction to metaheuristics is made. Although metaheuristics are very general, it was shown, that on average no search method performs better than any other [78, 79]. This statement is known as the 'no free lunch theorem' and expresses, that the computational effort of finding solutions of a complete class of problems is on average the same for any search method, or in other words: Any search algorithm is no better than random guess. The reason, why specific algorithms are used anyway, is that in real world scenarios they do perform better and those problems for which they perform worse are rather unrealistic. The downside of the heuristic approach is, that there is no guarantee, that the optimal solution to a problem is found or even, that any solution is found. The most common case is, that these algorithms converge towards a point near the global optimum, which could be considered 'good enough'.

With all these points taken into account, the procedures for the optimization of the random fiber grating coupler of figure 4.24 are Genetic Algorithm [80, 81] and Particle Swarm Optimization [82]. Genetic algorithms are a subclass of evolutionary algorithms, which seek to mimic the natural processes found in biology. By passing on beneficial traits from one generation to another the fitness of a population is increased incrementally. For application in an optimization problem a few terms need to be defined:

- Individual: An individual I is a candidate solution of the given problem. It has a genetic representation, which contains all features that determine its fitness; in this case $w_{g,i}$, $w_{r,i}$ and $h_{e,i}$ of all 24 grating periods. A genetic representation of a grating is:

$i = 1$			$i = 2$				$i = 24$		
$w_{g,1}$	$w_{r,1}$	$h_{e,1}$	$w_{g,2}$	$w_{r,2}$	$h_{e,2}$	$\cdots$	$w_{g,24}$	$w_{r,24}$	$h_{e,24}$

Table 4.1: Genetic representation of a grating with 24 periods.

- Fitness function: The fitness function f evaluates the fitness of an individual, by taking the genetic representation of it as a parameter and returns a real number from [0, 1], where 0 represents the lowest possible fitness and 1 the highest. Here, the fitness of a grating is the coupling efficiency to a standard single mode fiber, which is tilted at an angle $\varphi = 10°$. This angle is somewhat arbitrary, since one could optimize gratings for a different diffraction angle. In fact, all angles from ca. 3° to 15° could be considered equally well suited for near vertical fiber coupling, but such a loose definition of fitness is not beneficial to the performance of the search algorithm. Allowing a wide range of coupling angles to obtain equally high fitness values will result in high amount of local maxima in the fitness landscape and therefore hinder the convergence of the algorithm. For this reason an additional factor in f is introduced, which

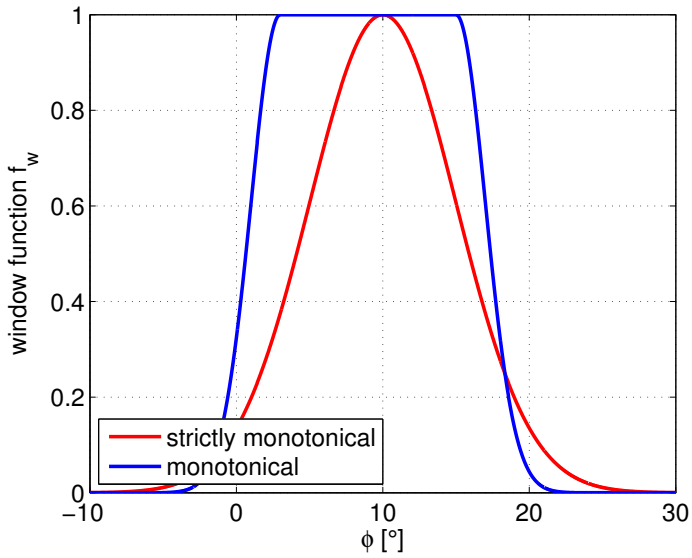

Figure 4.25: Angular window function f_w of the fitness function f. A plateau (blue line) will result in multiple local maxima in the fitness landscape. Better suited for convergence is a well defined maximum (red line).

penalizes the coupling efficiency at angles other than $\varphi = 10°$. Figure 4.25 shows this factor as a window function of acceptable coupling angles. The red line depicts the factor, that is actually used for the optimization algorithms. It is a Gaussian distribution centered at $\varphi = 10°$ and has a σ of 5°. The blue line exhibits a plateau from $\varphi = 3°$ to 15° with a Gaussian in- and decrease of $\sigma = 2°$. By allowing for more than one, discrete value the width of the global maximum in the fitness landscape is increased and thus it is more likely for the algorithm to locate it.

- Selection: The process by which the individuals are selected for breeding. Here, only the fittest individuals are allowed to produce offspring. The remaining individuals are eliminated from the population, so that the number of individuals of each generation is constant. The population size was chosen to be 30, from which the 10 fittest individuals were selected for breeding and living on to the next generation.

- Genetic operator: After selection for breeding a genetic operator is used to produce offspring from the selected individuals. Crossover takes the parents' genetic representation and mixes them up to form the child's genetic representation. Several strategies to decide which trait is selected from which parent are feasible. Although it is the case here, in general it is not even necessary to constrain crossover to two parents. N-point crossover defines N points on the genetic representation between which traits are selected from parent 1 and beyond which traits are selected from parent 2. Table 4.2 shows 2-point crossover. The crossover points may be set at random or so that the number of traits selected from each parent is proportional to its fitness. A simpler approach is to select traits at random (table 4.3). There is one major disadvantage to crossover: If the parents share traits no variation along this dimension is possible and the genetic algorithm is unable to explore the full parameter space. Therefore, mutation - another genetic operator - is employed to add

noise to the crossover process. If parent 1 and 2 are equal in one trait, then this trait has a chance to be randomly changed in the offspring. In contrast to crossover, mutation is a unitary operation, since it only requires one parent.

It is evident, that there are a very large amount of possible implementations of the genetic algorithm. Without prior knowledge of the field it is impossible to predict the performance of an implementation. One could therefore claim, that it is an optimization problem in itself to optimize a genetic algorithm for a specific problem.

The particle swarm algorithm is much simpler in its implementation and uses some of the same concepts as the genetic algorithm, though with a different terminology. Instead of individuals the literature speaks of particles and a population is called a swarm, hence the name particle swarm. Since particles do not reproduce or die off but move around the fitness landscape they have a position rather than a genetic representation. Therefore, it is also more common to speak of a time step than of a generation. The rules by which the movement of a particle I is determined can be simply defined as

$$\vec{x}_{I,t} = \vec{x}_{I,t-1} + \vec{v}_{I,t} \tag{4.13}$$

and

$$\begin{aligned} \vec{v}_{I,t} = \vec{v}_{I,t-1} & \\ & + c_1(\vec{x}_{I,Pbest} - \vec{x}_{I,t-1}) \\ & + c_2(\vec{x}_{I,Gbest} - \vec{x}_{I,t-1}). \end{aligned} \tag{4.14}$$

Equation 4.13 states, that the position $\vec{x}_{I,t}$ of a particle at time step t is determined by its position in the previous time step plus a velocity vector $\vec{v}_{I,t}$. The particles have a certain momentum, since their velocity vector is dependent on the velocity of the previous time step, which is initially zero along all dimensions. $\vec{x}_{I,Pbest}$ is the position, where particle I has found the highest fitness value up until time step t. It is called the personal best and the particle is accelerated toward this position. Similarly, $\vec{x}_{I,Gbest}$ is called the global best and denotes the position of highest fitness found by the neighborhood of particles up until time step t. The neighborhood is defined as the N nearest particles to particle I, but in many cases is just regarded as the complete particle swarm. Since particle I is part of its own neighborhood $\vec{x}_{I,Pbest}$ and $\vec{x}_{I,Gbest}$ may be equal. In contrast to the genetic algorithm individuals (or particles) need therefore memory of the best previous position as it is not necessarily part of the current generation (or time step). Also knowledge of the other particles' performance has to be made available to the swarm. c_1 and c_2 are scalars and need to be tuned for each problem as they weigh the acceleration to a particles personal best position or the neighborhoods best position, respectively. As a rule of thumb

Parent 1:									
$w_{g,1}$	$w_{r,1}$	$h_{e,1}$	$w_{g,2}$	$w_{r,2}$	$h_{e,2}$	$\cdots$	$w_{g,24}$	$w_{r,24}$	$h_{e,24}$
Parent 2:			crossover points						
$w_{g,1}$	$w_{r,1}$	$h_{e,1}$	$w_{g,2}$	$w_{r,2}$	$h_{e,2}$	$\cdots$	$w_{g,24}$	$w_{r,24}$	$h_{e,24}$
Child:									
$w_{g,1}$	$w_{r,1}$	$h_{e,1}$	$w_{g,2}$	$w_{r,2}$	$h_{e,2}$	$\cdots$	$w_{g,24}$	$w_{r,24}$	$h_{e,24}$

Table 4.2: Genetic representation of 2-point crossover.

Parent 1:									
$w_{g,1}$	$w_{r,1}$	$h_{e,1}$	$w_{g,2}$	$w_{r,2}$	$h_{e,2}$	$\cdots$	$w_{g,24}$	$w_{r,24}$	$h_{e,24}$
Parent 2:									
$w_{g,1}$	$w_{r,1}$	$h_{e,1}$	$w_{g,2}$	$w_{r,2}$	$h_{e,2}$	$\cdots$	$w_{g,24}$	$w_{r,24}$	$h_{e,24}$
Child:									
$w_{g,1}$	$w_{r,1}$	$h_{e,1}$	$w_{g,2}$	$w_{r,2}$	$h_{e,2}$	$\cdots$	$w_{g,24}$	$w_{r,24}$	$h_{e,24}$

Table 4.3: Genetic representation of random crossover.

it has been found that $c_1 + c_2 \approx 4$ usually yields good results [83]. Furthermore, in most cases it is unavoidable to define a speed limit for particles. It is easily possible for particles to gain velocity at each time step. After a few time steps it could so high that the particles are confined to the boundaries of the parameter space and therefore are unable to sample the fitness landscape. This effect is known as 'explosion' and can be prevented by a speed limit, for which the following adaptation of $\vec{v}_{I,t}$ is valid:

$$\vec{v}_{I,t} = \frac{\vec{v}_{I,t}}{|\vec{v}_{I,t}|} \min(|\vec{v}_{I,t}|, v_{max}). \tag{4.15}$$

However, it should be noted, that in this optimization 3 different types of features are subject to variation. A change in etch depth is expected to yield a stronger effect than a change by the same magnitude in groove width or ridge width. Therefore, the speed limit for variation in etch depth was set to $10nm$ per time step, while groove width and ridge width can be varied with $15nm$ per time step. Several other means of ensuring convergence of the particle swarm algorithm were subject of investigation [84, 85], but are not necessary for well behaved fitness landscapes. Again, the optimization with respect to convergence of the algorithm is an optimization problem in itself.

4.4.4 Simulation Results

On each time step t 32 individuals (particles) were evaluated in parallel. Their position was updated according to the rules of genetic and particle swarm algorithm, respectively. After each iteration step the best performing device was stored in memory if its fitness was higher than the previously best one's. Figure 4.26 shows the fitness of the up to time step t found best performing device as a function of time steps / iterations. To reduce complexity it was assumed, that three consecutive grating periods are equal, thus reducing the size of the parameter space from 72 to 24 dimensions. Since at each time step 32 simulations were carried out in parallel the total number of simulations for each optimization algorithm seen in figure 4.26 amounts to 4000. Solutions found at later time steps did not offer an improvement and are therefore omitted from the plot. Although both algorithms yield equally well performing devices, it must be noted, that the genetic algorithm found the global maximum only in rare cases. In the majority of attempts it got stuck in local maxima at coupling efficiencies of around 45%, from which it failed to escape. Only if the starting position of an individual was close the global maximum the algorithm was able to reach it. Figure 4.26 illustrates this circumstance at time step $t = 0$, where the fitness value of the genetic algorithm is already at 50%. The particle swarm algorithm on the other hand only failed in a few cases, but with a more

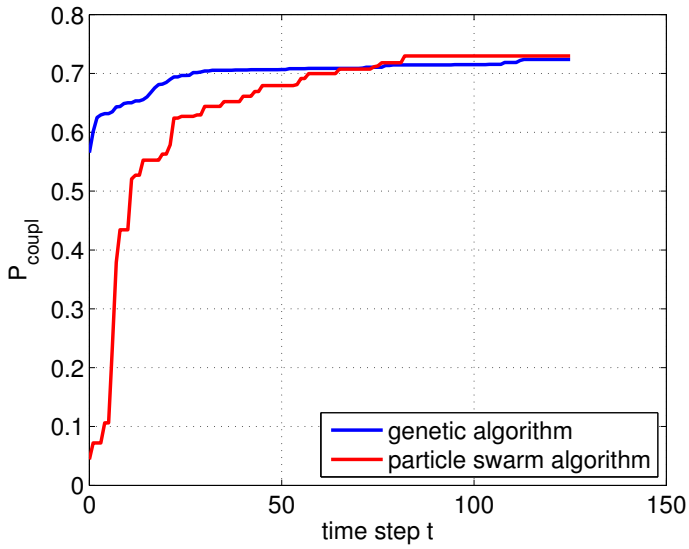

Figure 4.26: Performance of genetic algorithm (blue) and particle swarm algorithm (red) over time.

severe outcome as the coupling efficiencies didn't exceeded 10% in those instances. Most of the time positions near the global maximum were found within very few time steps, giving rise to the rapid increase in coupling efficiency seen in figure 4.26. Coupling efficiencies of gratings optimized with both methods are 73% or -1.37dB. Feature sizes of an optimized grating are shown in figure 4.27.

The etch depths $h_{e,i}$ (green line) show a clear linear growth along the grating, which is true for every simulation run, that resulted in a grating coupler with high efficiency. The grating periods Λ_i show a greater variation, which is mainly due to the spread in groove widths $w_{g,i}$, while the ridge widths $w_{r,i}$ display a nearly linear behavior.

With that result in mind a new parameter space can be constructed by assuming a linear behavior for every type of feature, i.e. each feature is varied linearly along

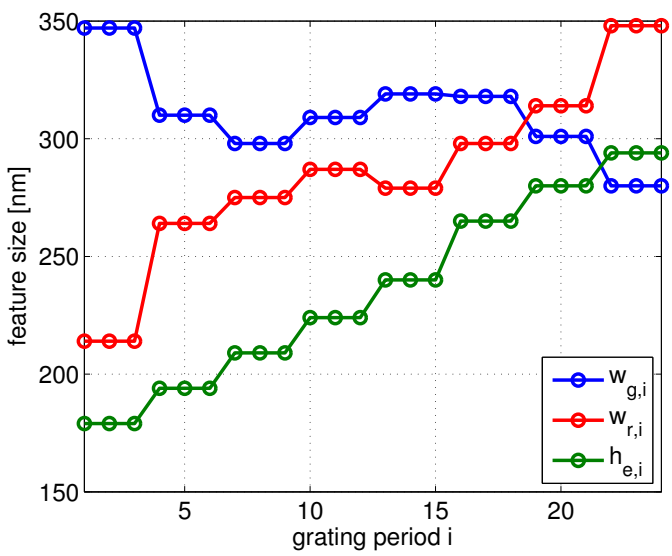

Figure 4.27: Geometrical features of an optimized grating coupler with groove width w_g (blue), ridge width w_r (red) and etch depth h_e (green).

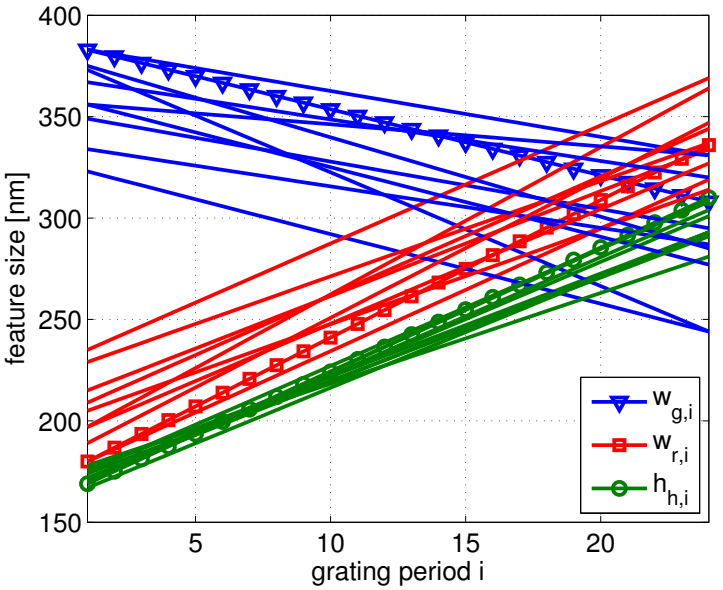

Figure 4.28: Geometrical features of 10 different fiber grating couplers found by particle swarm optimization assuming linearized features along the grating. One related set of parameters is highlighted and analyzed in figure 4.29.

the grating and not stepwise for independent groups of three consecutive periods as before, thereby reducing the number of dimensions from previously 24 to now only 6. The new parameter space requires fewer individuals / particles, thus the population size / swarm size was reduced to 10 to 15 members. Resulting feature sizes of 10 different optimization runs are depicted in figure 4.28. All gratings shown display coupling efficiencies above 76% (-1.2dB). As suspected from the results seen in figure 4.27, there is very little variation in etch depth for high efficiency grating couplers available. The spread of etch depth at the beginning of the grating $\Delta h_{e,1}$ amounts to only $11nm$. Since at the end of the grating exact feature sizes are not as important, due to the low amount of power remaining in later periods, the spread becomes larger and is at the last grating period $\Delta h_{e,24} = 29nm$. Relative to the etch depths at beginning and end of the grating the spread increased by 3%. More variation is allowed for groove widths and ridge widths. The spreads $\Delta w_{g,1} = 60nm$ and $\Delta w_{g,24} = 87nm$ show a relative increase of 10% from beginning to end and the spread of ridge widths stays nearly constant with $\Delta w_{r,i} = 55nm$.

Figure 4.29 shows the coupling spectrum of a grating with linearized feature sizes. The geometry corresponds to the highlighted plots of figure 4.28. The dashed magenta line shows the coupling efficiency to a standard single mode fiber tilted at 10°. It has a clear maximum at $\lambda = 1.55\mu m$, as was aimed for by the optimization algorithm. The coupling efficiency is 77% or 1.1dB. However, it is also recognizable, that a slightly better result can be achieved through $\varphi = 8°$ fiber tilt. Here the maximum coupled power is 79% or 1dB at $\lambda = 1.564\mu m$. This result is due to two reasons: Firstly, the window function 4.25 was not optimally chosen. Better performing devices can be obtained by an adaption of coupling angle φ. Secondly, the out-coupled power P_{out} is higher at longer wavelengths, before it falls off again and a higher order grating is achieved. This mismatch can usually be compensated by an adaption of grating period Λ, however as mentioned before, particle swarm and genetic algorithms are very unlikely to find the global maximum, but rather a solution

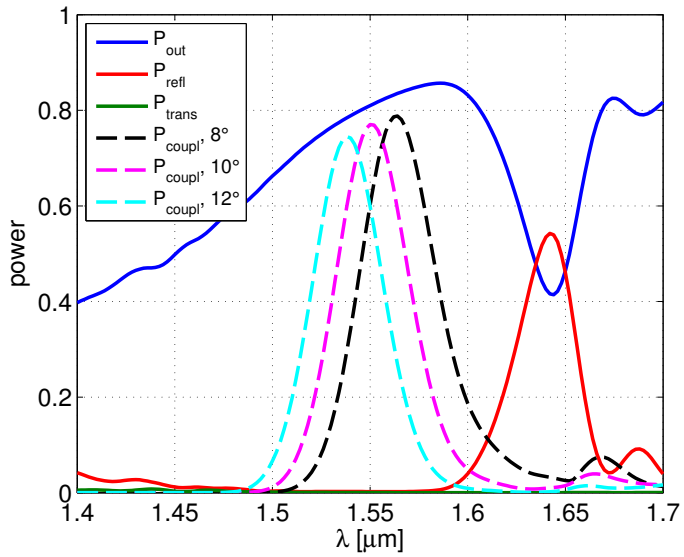

Figure 4.29: Coupling spectrum of a grating optimized with particle swarm algorithm. The dimensions are highlighted in figure 4.28.

that is very close to it. For an improved solution another optimization algorithm needs to be employed after the heuristic search. However, only slight improvements over a 'good enough' solution are to be expected, making the computational effort bear no proportion to the gain.

Reflection and transmission spectra are well below 1% at the center wavelength, indicating a smooth transition from the waveguide to the grating and a high diffraction efficiency, respectively. The distance between maximum coupled power (dashed lines) and out-coupled power P_{out} near $\lambda = 1.55\mu m$ is only 4%, indicating a high overlap between diffracted field and fundamental fiber mode.

4.4.5 Variation of the Epitaxial Layer Height

In the previous section a reduced parameter space was introduced, by linearizing the feature sizes along the grating. In this section a fourth feature - the epitaxial layer height h_{epi} - is included as a parameter into the search space. The optimization process stays the same as before, but the dimensionality of the search was increased to 8. Additionally, the fiber tilt angle φ was increased to 12°. Figure 4.30 shows the resulting feature sizes of an optimization run. Groove width and ridge width display the same characteristics as seen in figure 4.28. The etch depth on the other hand stays nearly constant along the grating with only a slight decrease of 9nm from beginning to end. To compensate, the epitaxial layer height shows a strong variation from 234nm at the first grating period and 9nm at the last one. The coupling spectrum associated with this grating is depicted in figure 4.31. The coupling efficiency is 85% or 0.7dB at $\lambda = 1.55\mu m$. Again a slight improvement, which is due to the minimally higher out-coupling efficiency P_{out}, can be achieved by lowering the fiber tilt angle to $\varphi = 10°$ and a longer center wavelength of $\lambda = 1.566\mu m$, although the gain is very small with 1%. The distances between P_{out} and peak coupling efficiencies is even smaller compared to the one seen in figure 4.29. With only 2.5% loss from mismatch between scattered field and fiber mode, the grating displays a very high mode overlap with the LP_{01} mode of the fiber. The overall out-coupled

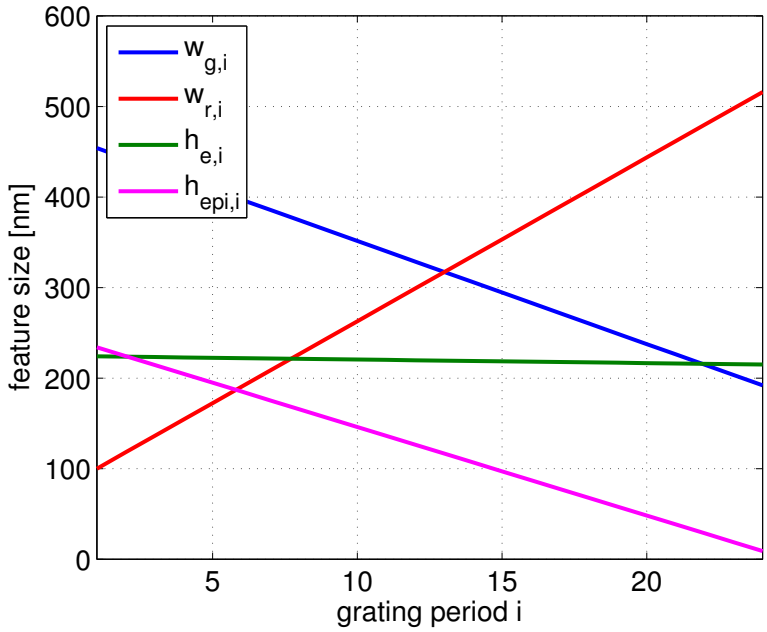

Figure 4.30: Feature sizes of an optimized grating with variable epitaxial layer height h_{epi}.

power P_{out} is also slightly increased to 88%, contributing to the good performance of the device. Reflection and transmission are higher than before, but with 1% and 0.1%, respectively still very good. Figure 4.31 (right) shows a to scale drawing of the device, together with field plots of the electric field and its phase. The high directionality is apparent in the high field amplitude above the grating and the low amount of field in the buried oxide and substrate. The high overlap with the LP_{01} fiber mode stems from the soft increase of field amplitude in the beginning of the grating and the flat phase, tilted at 10° with respect to the horizontal plane.

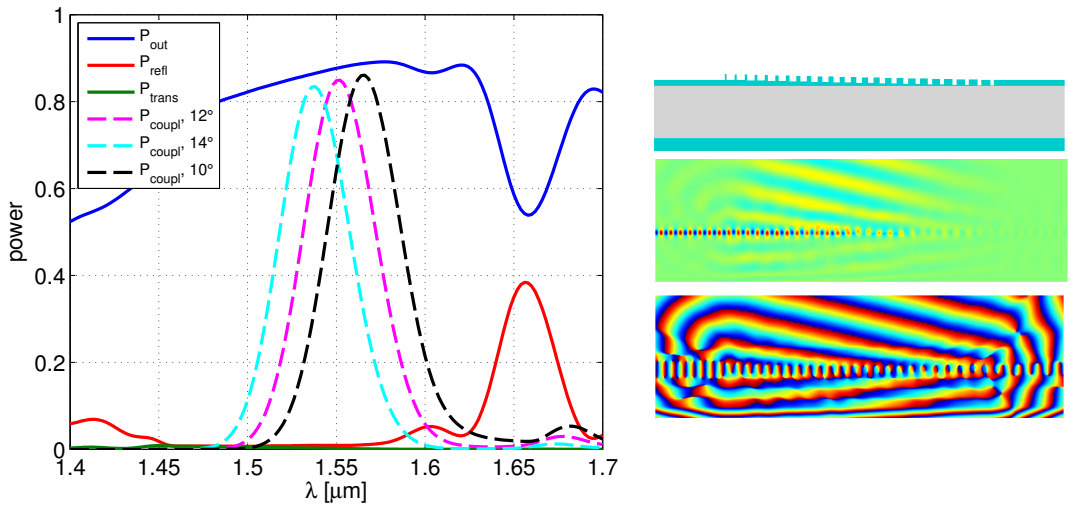

Figure 4.31: Left: Coupling spectrum of a grating with variable epitaxial layer height h_{epi}. Right: To scale cross section representation of a grating with variable epitaxial layer height together with field plot and phase plot.

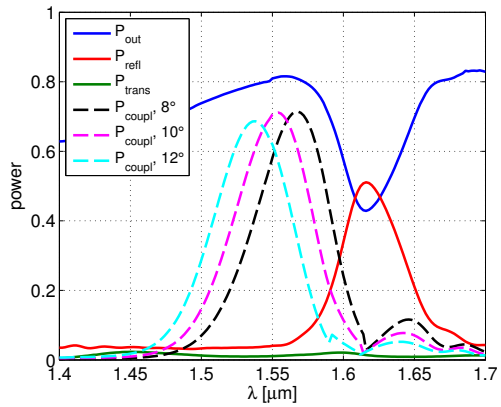

Figure 4.32: Coupling spectrum of a chirped grating with constant etch depth $h_e = 198nm$ and epitaxial layer height $h_{epi} = 150nm$.

4.5 Chirped Gratings

In view of manufacturability, gratings with variable etch depth or epitaxial layer height along the grating are hard to realize. For every grating period a unique mask layer is needed, making the production of a grating as presented in the previous sections extremely difficult. From the production point of view a single etch depth and epitaxial layer height across all grating periods is therefore preferred.

The optimization method used in the previous sections can once again be employed to find such gratings by defining an additional constraint on the etch depths, which requires the slope of the linear function describing the etch depth to be zero. The number of degrees of freedom in this search is therefore reduced to 5. For a better comparison the SOI layer stack is adapted to the standard as used in section 4.2 of this chapter (i.e. $h_{wg} = 220$nm, $h_{epi} = 150$nm and $h_{cl} = 1.3\mu m$).

The parameters found by the optimization process are shown in table 4.4. The intuitive conclusion of having a positive chirp, i.e. having small groove widths w_g at the beginning of the grating and moving to larger groove widths at later stages to give rise to a soft increase in field intensity above the grating [86] was not found to be optimal. Instead the optimization process found a negative chirp to be better suited to obtain a high overlap with the fundamental fiber mode as was partially used in [87]. An additional beneficial property of the large feature size at the beginning of the grating, where accuracy is most important, is the easy manufacturability. As reported in [22] a secondary etch step of lower depth could be utilized to avoid thin groove widths below the limit of fabrication to maintain an optimal chirp. However, with inversely chirped grating couplers this would be unnecessary, since large features are located at the front side of the grating where the amount of power diffracted is high and small feature sizes are pushed to the far end of the grating, where ideally no power is left in the waveguide. The resulting spectrum of such a grating with a peak coupling efficiency of -1.48dB is shown in figure 4.32.

	w_g	w_r	h_e	h_{epi}
$i = 1$	500nm	100nm	198nm	150nm
$i = 25$	283nm	315nm	198nm	150nm

Table 4.4: Design parameters of a chirped grating coupler with constant etch depth.

Chapter 5

2D Gratings

In this chapter the concept of a grating coupler based polarization splitter, first proposed by Taillaert et al. [24] is built upon by improving performance using results obtained in the previous chapter. Additionally, a novel device for the excitation of higher order fiber modes based on a two dimensional grating coupler is presented, together with all photonic integrated devices necessary for its application.

5.1 Gratings with High Directionality

To achieve polarization diversity, a grating capable of coupling both TE and TM polarization between fiber and PIC is required. In contrast to edge coupling approaches, that do not display much of a polarization dependency, grating couplers are usually operative for one polarization only. The reason for that is the large birefringence of the integrated waveguides, that is expressed in the vastly different effective refractive indices of the fundamental TE and TM modes, resulting in very dissimilar grating periods necessary for coupling of light of different polarizations. An additional difficulty connected to the use of nano wire waveguides is the coupling between the fundamental TM_{00} and the TE_{10} mode in an adiabatic taper [88] as used for increasing waveguide widths, causing difficulties when trying to couple the fundamental TM between different waveguide widths, as is done easily for the fundamental TE mode in a taper. An elegant solution to these problems is a

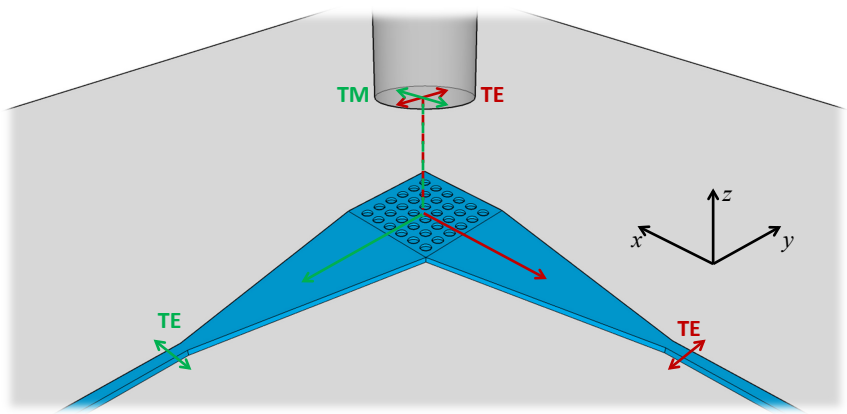

Figure 5.1: Sketch of a two dimensional fiber grating coupler coupling E_x and E_y polarized light from a fiber to TE modes in the integrated waveguides.

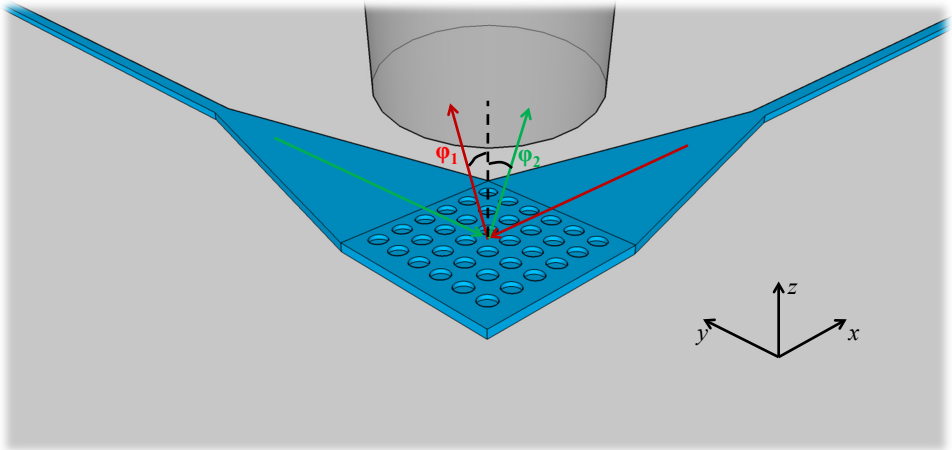

Figure 5.2: Diffraction angles φ_1 in the xz-plane and φ_2 in the yz-plane of a two dimensional fiber grating coupler.

two dimensional grating as shown in figure 5.1. By superposition of one dimensional gratings with a 90° angle between them a two dimensional grating exhibiting a diffraction structure in two orthogonal directions is formed. Although the fiber may carry both TE and TM polarized light, coupling to the TM mode in the PIC is completely avoided, since both fiber modes are translated into TE modes in the integrated waveguides. Therefore only a single grating period adjusted for the effective refractive index of the TE mode is needed in both waveguide directions.

It is clear, however, that for equal coupling to both polarizations, the fiber has to be positioned symmetrical with respect to both waveguides. In contrast to one dimensional gratings shown in previous chapters, where the fiber was simply positioned for optimal coupling efficiency, in the case of two dimensional gratings equal performance is an additional concern. Figure 5.2 shows the positioning of the fiber with respect to the integrated waveguides. Due to the higher dimensionality of the problem, the fiber tilt is now described by two angles φ_1 and φ_2 in the xz-plane and yz-plane, respectively. A symmetrical setup is achieved, when $\varphi_1 = \varphi_2$. However, highest coupling efficiency on either arm is obtained, when $\varphi_1 = \varphi, \varphi_2 = 0°$ or $\varphi_1 = 0°, \varphi_2 = \varphi$, where φ is the optimal coupling angle as defined for the one dimensional case, since the grating adds solely a component in z-direction to the wave vector of the diffracted field and not in the orthogonal y- and x-direction. Both conditions may be satisfied at the same time in the special case of strictly vertical coupling ($\varphi_1 = \varphi_2 = 0°$). However, this constraint adds an additional 3dB loss to the coupling efficiency, as light from the fiber will be equally coupled in positive and negative x- and y-direction and should therefore be avoided. Nonetheless, small coupling angles yield the highest field overlap, when fiber and grating are set up symmetrically as they would be in a realistic setup, since the mismatch between diffracted field and fiber mode scales with the diffraction angle. To give a rough estimation of that effect, figure 5.3 shows the field overlap penalty η between the LP_{01} mode of a sSMF and the diffracted field of a grating as a function of deviation $\Delta\varphi$ from its optimal fiber tilt angle $\varphi = \varphi_1 = \varphi_2$ in a setup as shown in figures 5.1 and 5.2. The field overlap vanishes quite rapidly, when the fiber is tilted away from its optimal angle, confirming the assumption, mentioned here and in the previous chapter, that the optimization towards small diffraction angles will yield better re-

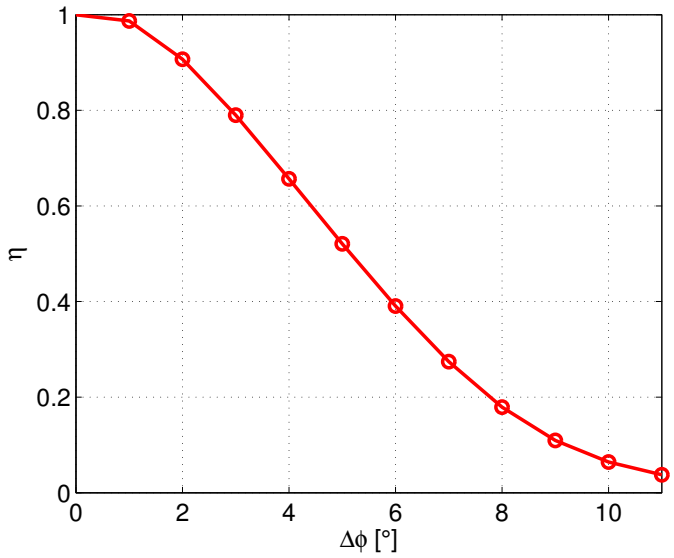

Figure 5.3: Field overlap penalty η as a function of fiber tilt angle deviation $\Delta\varphi$ in a symmetric two dimensional grating setup.

sults in two dimensional grating couplers. Therefore the minimization of coupling angles $\varphi_1 = \varphi_2$ is an additional design goal of the optimization next to out-coupling efficiency.

Since the structure exhibits variation along all spatial dimensions, a reduction to lower dimensions is no longer possible. Thus the device needs to be simulated in three dimensions, which is a numerically expensive endeavor. A refinement of the computational grid to obtain an arbitrary degree of accuracy is no longer possible as this will easily exceed computational resources. Therefore a reduced computational domain is employed to obtain the numerical parameters of the Finite Element Method, that yield results with suitable accuracy. Figure 5.4 shows the full Finite Element model of the device and a reduced model of the same device with only one row of unit cells.

To obtain the achievable degree of accuracy the reduced model is used, since the full model can not be simulated with a finite element degree $p > 3$ with the available computers due to limited memory. The results are shown in figure 5.5, where the relative error in electric field energy is displayed for various finite element degrees as a function of computation time. The error is normalized to the electric field energy

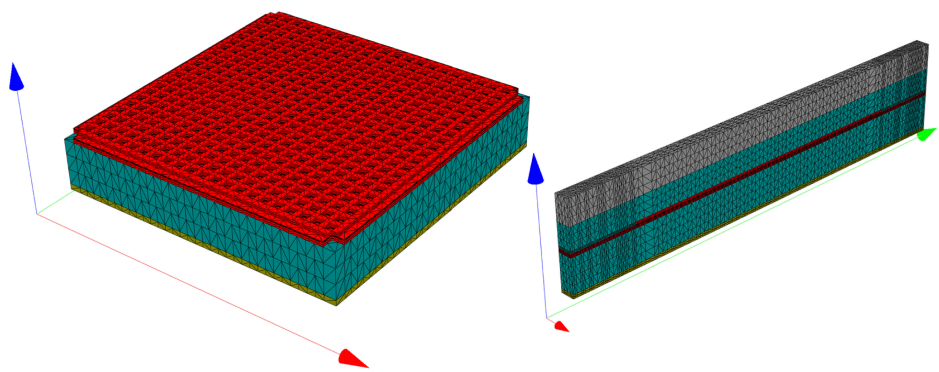

Figure 5.4: Finite Element models of two dimensional grating couplers.

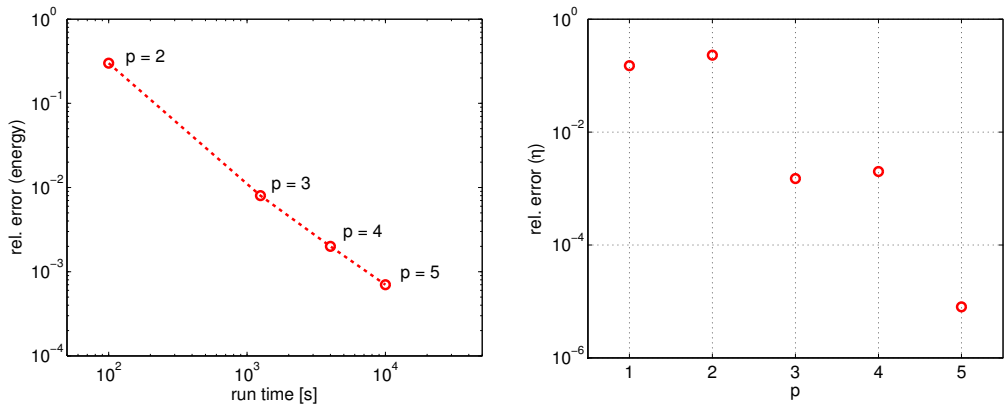

Figure 5.5: Relative error of Finite Element simulations in field energy (left) and overlap η (right).

computed with finite elements of degree $p = 6$, which was the maximum computers could handle and therefore serves as a quasi-exact solution. The time needed to solve a reduced problem increased from minutes to hours, while the relative error decreased from the order of 10^{-1} to 10^{-3}, when p was increased. The relative error in the overlap integral η similarly decreased from 10^{-1} to even 10^{-5} at $p = 5$. It can be seen, that an error below 1% can be reached with a finite element degree of $p \geq 3$, which is sufficient for the optimization of the grating couplers to be shown. The simulation of the full model with $p = 3$ took around 3.5 hours, which is even slightly more than the reduced model with $p = 5$. The number of unknowns to be solved for amounted to over $9 \cdot 10^6$, requiring approximately 500GB of RAM.

As a starting point for the optimization results obtained from one dimensional grating couplers were used. Again, an epitaxial layer of height $h_{epi} = 150nm$ for an increased directionality is employed. The values for out-coupled power P_{out}, field overlap η and coupling angle φ are shown in figure 5.6.

Although other values regarding etch depth and epitaxial layer height were tested as well, the values of $h_{epi} = 150nm$ and $h_e = 210nm$ were found to yield best results. The plots shown contain 441 individual simulations amounting to more than 65 days of simulation time.

The performance of the two dimensional grating is similar to the one dimensional case, albeit with a slightly lower out-coupling efficiency P_{out}, which most likely caused by the non etched parts of the two dimensional grating structure, where the incoming field may simply pass through. At acceptable coupling angles ($\varphi < 6°$)

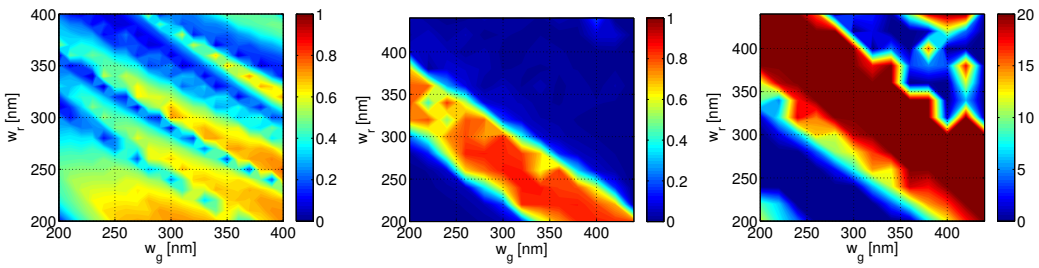

Figure 5.6: P_{out} (left), η (middle) and $\varphi(= \varphi_1 = \varphi_2)$ (right) as a function of w_g and w_r in a two dimensional grating coupler of $h_{epi} = 150nm$ and $h_e = 210nm$ with rectangular etches at $\lambda = 1.55\mu m$.

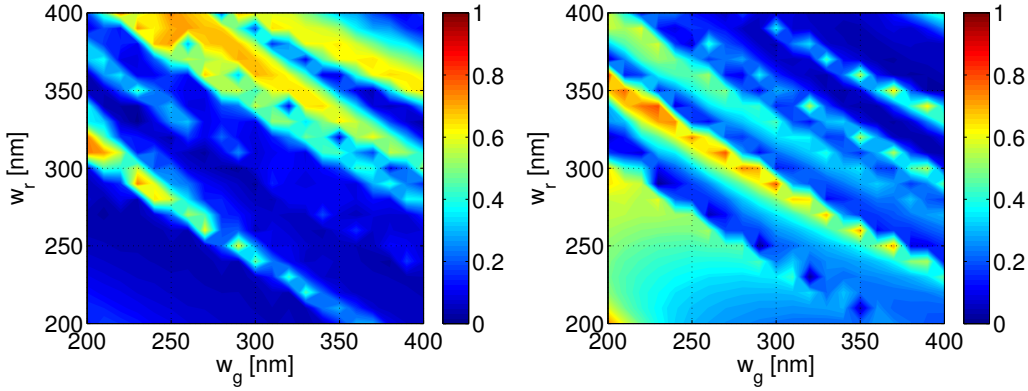

Figure 5.7: P_{refl} (left) and P_{trans} (right) as a function of w_g and w_r in a two dimensional grating coupler of $h_{epi} = 150nm$ and $h_e = 210nm$ with rectangular etches at $\lambda = 1.55\mu m$.

out-coupling efficiencies of 70% are reached at grating periods $\Lambda < 590nm$ and rather large duty cycles. To confirm the origin of the additional loss compared to one dimensional gratings figure 5.7 shows the reflected (P_{refl}) and transmitted (P_{trans}) powers. It is evident, that while for one dimensional gratings reflected and transmitted power were in the order of 5% and below 1%, respectively, the two dimensional gratings display much higher values here. For gratings with reasonable coupling efficiencies (e.g. $P_{coupl} = 56\%$ for gratings of $w_g = 350nm$ and $w_r = 220nm$ and 25 periods) reflected and transmitted power amount to $P_{refl} = 5\%$ and $P_{trans} = 10\%$ at $\lambda = 1.55\mu m$. The high amount of transmitted power is to be expected, since a grating with ridge width $w_r = 220nm$ and 25 periods displays $5.5\mu m$ of unperturbed waveguide, where light may pass through undisturbed. For this reason, a bottom reflector as used for one dimensional gratings will not yield as much benefit in the two dimensional case, as loss to the substrate is less significant.

Figure 5.8 shows the coupling spectrum for a two dimensional grating with rect-

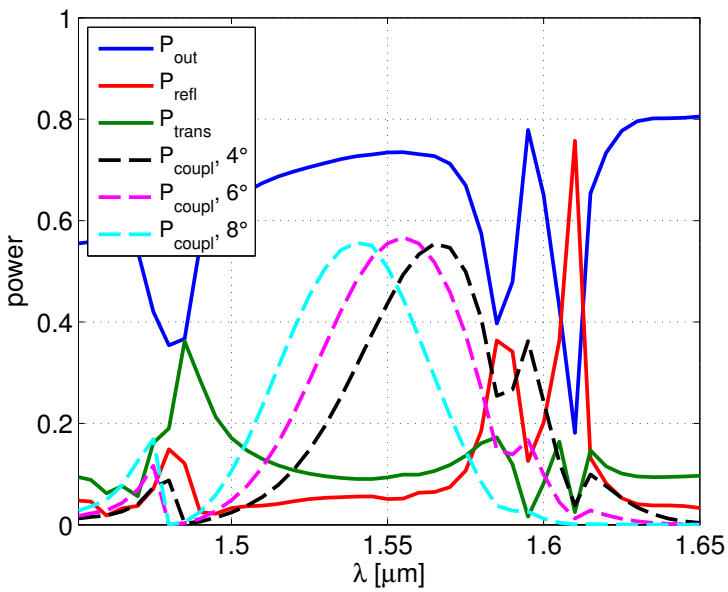

Figure 5.8: Coupling spectrum of a two dimensional grating coupler with rectangular etches of $w_g = 350nm$ and $w_r = 220nm$.

angular etches and the design parameters $w_g = 350nm$, $w_r = 220nm$, $h_e = 210nm$ and $h_{epi} = 150nm$. The coupled power was calculated for optimal coupling efficiency with respect to fiber tilt angles φ_1 and φ_2 (i.e. $\varphi_1 = \varphi$ and $\varphi_2 = 0°$). The coupling efficiency in a symmetric setup (i.e. $\varphi_1 = \varphi_2 = \varphi$) is 30% lower at $\varphi = 6°$ due the additional mismatch in field overlap (c.f. figure 5.3).

Again, a coupling angle of $\varphi = 6°$ yields optimal results near the central wavelength of $\lambda = 1.55\mu m$, with a maximum coupling efficiency of $P_{coupl} = 56\%$ at the slightly longer wavelength of $\lambda = 1.555\mu m$. A $\pm 2°$ shift of fiber tilt angle from the optimal position will result in a 12nm wavelength shift to a lower or higher wavelength region, respectively. The out-coupled power P_{out} is above 70% over the entire C-band and falls off beginning at $\lambda = 1.57\mu m$, where similar to the one dimensional grating the diffraction order changes and the efficiency drops to a minimum.

5.1.1 Measurement

The results of a transmission measurement are shown in figure 5.9 together with an electron microscope image of the device. Although the measurement results do not agree with the values obtained from simulation to a certain extent, the coupling efficiency reaches its maximum with a fiber tilt angle $\varphi(= \varphi_1 = \varphi_2) = 6°$ at $\lambda = 1.56\mu$m and is therefore very close to the predicted value. The coupling efficiency though is with $P_{coupl} = -5.8$dB lower as planned, which is most likely caused by the rounded shape of the grating etches, as can be seen in figure 5.9 (right). Simulations conducted with a grating of circular etches do indeed show a lower coupling efficiency in gratings with otherwise identical design parameters.

Since a comparatively high amount of transmitted power is expected, a taper structure behind the grating was added to reduce reflections back into the waveguide at an abrupt waveguide facet.

To overcome the rounding of rectangular conceptualized structures of small size, an optical proximity correction (OPC) may be employed. By pre-distorting the layout on the mask a reduction of imaging defects may be accomplished, resulting in shapes, that are closer to the desired layout after fabrication. To prevent rounding of corners, as was seen in the grating couplers, serifs of dimensions near or below the resolution limit of the lithography process are added to the mask. Figure 5.10

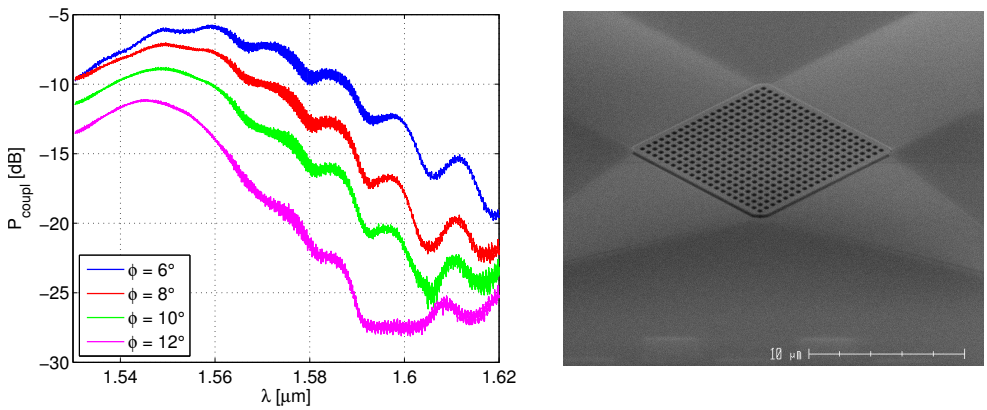

Figure 5.9: Left: Measured coupling spectrum of a two dimensional grating coupler with rectangular etches of $w_g = 350nm$ and $w_r = 220nm$. Right: Electron microscope image of the two dimensional grating coupler.

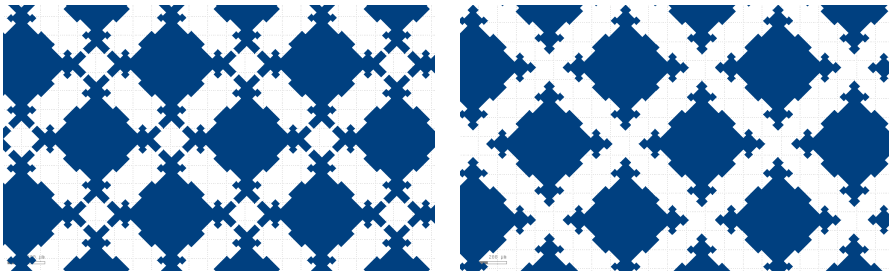

Figure 5.10: Two versions of optical proximity correction for a mask layout for two dimensional gratings with rectangular etch shape.

shows two options of such corrections, that may be used in future layouts of two dimensional fiber grating couplers.

5.2 Sheared Gratings

As mentioned in the previous section, for an optimal alignment of fiber and a two dimensional grating coupler the condition $\varphi_1 = \varphi_2$ (see figure 5.2) has to be met. Although this ensures an equal treatment of both polarizations and integrated waveguide arms, the coupling efficiency was reduced depending on the diffraction angle of the grating. Since the fiber extended equally in both x- and y-direction but the wave vector of the scattered field of either waveguide arm exhibited only components in either one of these dimensions, a high overlap between diffracted field and fiber mode could not be achieved.

To rectify this problem a distortion of the grating may be introduced, that breaks the symmetry in transverse waveguide direction, resulting in a non-zero component of the diffracted field's wave vector in that direction. The distortion of the grating, by which this can be accomplished is a shear mapping, as shown in figure 5.11. The aim of this transformation is to introduce a phase delay to the waveguide mode, that is dependent on the transverse position in the waveguide. In figure 5.11 e.g., the waveguide emerging from the bottom is aligned along the x-direction of the local coordinate system. Therefore, an undistorted grating would result in a diffracted field whose wave vector only holds components in x- and z-direction. A shearing

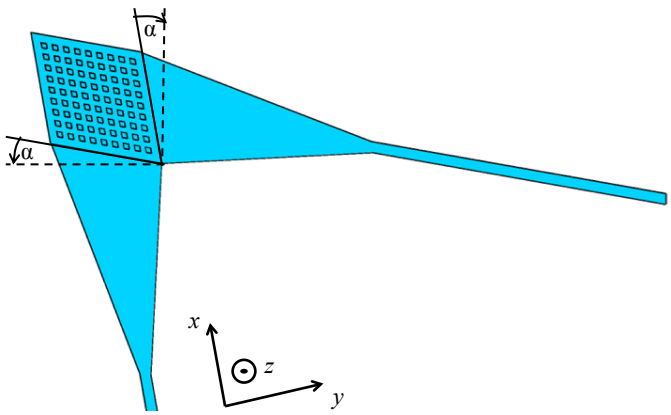

Figure 5.11: Sketch of a two dimensional fiber grating coupler with sheared etches for equal coupling in both waveguide arms.

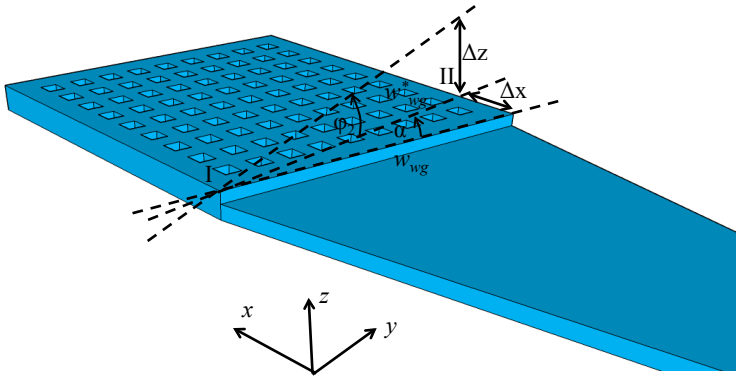

Figure 5.12: Geometry parameters in a sheared grating used to calculate phase differences in transverse direction.

as shown would result in an additional component pointing in negative y-direction, since the incoming waveguide mode is slightly longer contained inside waveguide at low y-positions compared to positions at larger y. The resulting diffraction angle φ_2 in the yz-plane may be estimated through the path difference of the optical field at the extreme ends of the waveguide. Assuming the effective refractive index in the unperturbed waveguide is n_{eff} and the one in the grating region is $n_{eff,g}$ as obtained by equation 2.8 via estimation of the actual phase constant of the waveguide mode in the grating region ($\beta \approx 2.5 \cdot \frac{2\pi}{\lambda}$), the phase difference between points I and II (see figure 5.12) may be expressed as

$$\Delta\phi = \phi_I - \phi_{II} = \frac{2\pi}{\lambda}\Delta x(n_{eff} - n_{eff,g}), \tag{5.1}$$

where $\Delta x = w^*_{wg}\tan(\alpha)$ is the geometric path difference between the points in x-direction. The resulting path difference in vertical z-direction above the grating therefore is

$$\Delta z = \Delta x \frac{n_{eff} - n_{eff,g}}{n_{cl}}, \tag{5.2}$$

with the refractive index of the cladding material n_{cl}. The value for the angle φ_2

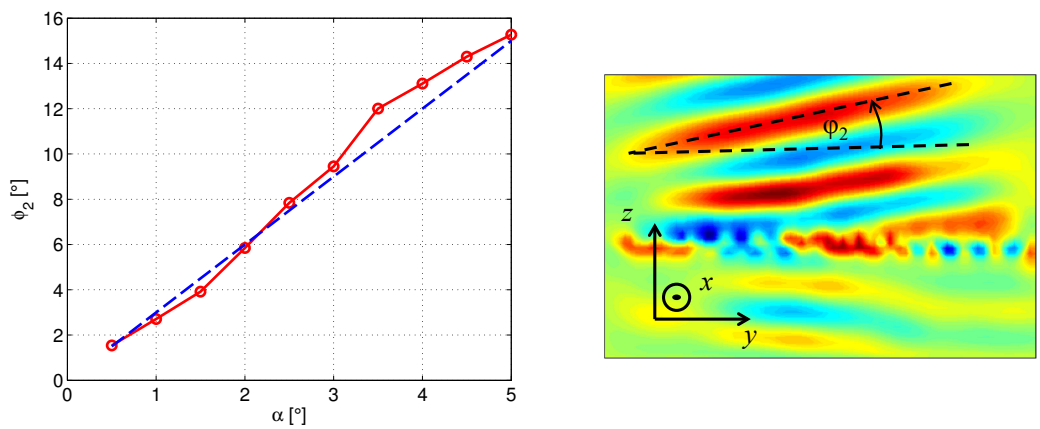

Figure 5.13: Left: Resulting diffraction angle φ_2 in yz-plane as a function of shearing angle alpha for a grating of $w_g = 350nm$ and $w_r = 220nm$. Right: Scattered field in yz-plane.

may now be calculated with the projected waveguide width $w^*_{wg} = w_{wg}\cos(\alpha)$ as

$$\tan(\varphi_2) = \tan(\alpha)\frac{n_{eff} - n_{eff,g}}{n_{cl}}, \tag{5.3}$$

A simulation of gratings with sheared etches confirms the linear correlation 5.3. As can be seen in figure 5.13 the slope of the resulting diffraction angles φ_2 is quite high, indicating, that a small shearing angle α is sufficient to achieve large changes in φ_2. A grating with the diffraction angle $\varphi_1 = 6°$ as presented in the previous section requires a shearing angle $\alpha = 2°$ to achieve optimal coupling in a symmetrical fiber grating setup, as shown in figure 5.1. A cross section view of the scattered field in yz-plane of the grating (figure 5.13, right) illustrates the tilted nature of the phase fronts, which in an unsheared grating would otherwise be purely horizontal.

5.3 Gratings for Multimode Operation

In this section a grating capable of exciting several LP fiber modes of a few mode fiber is presented. The modes in question are the LP_{01}, $LP_{11,a}$, $LP_{11,b}$ and $LP_{21,a}$ mode, which can all be excited in both TE and TM polarization simultaneously and independently from each other. In contrast to integrated optical devices presented in the literature, where multiple gratings are used to emulate the field distribution of a LP fiber mode [28, 29, 30] or where modes in special types of fibers are considered [27], the structure shown here combines the strengths of these devices by relying on a single grating, which excites the conventional LP fiber modes. The advantage of using only a single grating instead of multiple ones is a potentially higher efficiency, since in order to couple from multiple gratings to a single fiber core the gratings either need to be very small, thus reducing the fraction of out-coupled power or the fiber core needs to be very large, having negative impact on the propagation characteristics of the fiber. From a theoretical point of view there is no benefit of using a certain set of modes over another, however the modes used in [27] require a special kind of ring core fiber, increasing the cost of transmission system utilizing those. Using more standardized components would certainly alleviate this problem. Although, in contrast to single mode fibers no standard few mode or multimode fibers are standing out yet, the industry tends to lean towards conventional graded index or step index fibers [89].

5.3.1 Concept

To excite a fiber mode with a grating coupler two conditions have to be met: First the intensity profiles of the diffracted field and the one of the fiber mode have to match. And secondly, the relative phases of adjacent intensity maxima have to be different depending on the mode to be excited. In the case of the gratings examined so far, these two conditions were easy to meet, since only one intensity maximum with a flat phase has to be generated to excite the fundamental fiber mode LP_{01}. To create multiple maxima as e.g. for one of the LP_{11} modes, the devices presented in [28, 29, 30] use two (or more) different gratings for the two intensity maxima. Here, to do so, only a single grating is used to accomplish that.

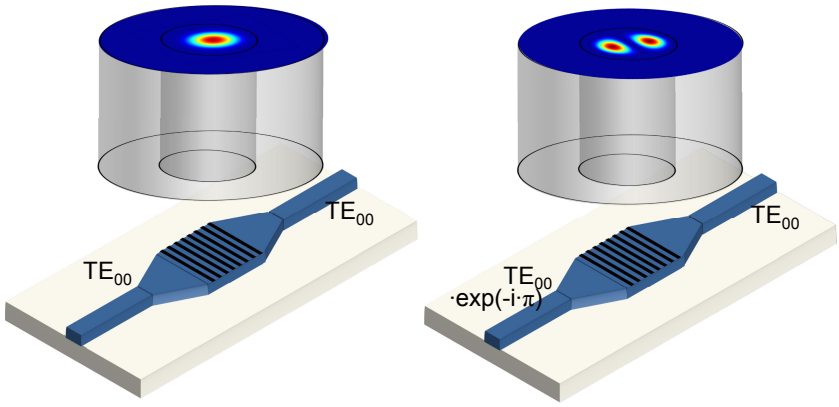

Figure 5.14: Sketch of a fiber grating coupler with two input waveguides located on opposing ends fed with TE_{00} modes with $\Delta\phi = 0$ (left) and $\Delta\phi = \pi$ (right) relative phase difference between them.

The LP_{01} and $LP_{11,a}$ modes are generated by feeding a grating from opposing ends with the fundamental modes (TE_{00}) of the integrated waveguides, as shown in figure 5.14.

If there is no phase difference between the modes of the input waveguide ($\Delta\phi = 0$), the scattered field in any plane above the grating will be equal in phase. It can be seen, that through the symmetric setup of the structure the wave fronts of the diffracted fields are purely horizontal, leading to a coupling angle of exactly $\varphi = 0°$, almost independently of wavelength. This is still the case, if the phase difference between the incoming TE_{00} modes is $\Delta\phi = 180°$, for which the diffracted field does not form a single intensity maximum in the middle of the grating, but two distinct ones with a relative phase difference of 180°, resembling the $LP_{11,a}$ fiber mode.

The correct distribution of intensity is achieved through tuning the length of the grating in combination with its strength. One can imagine, that a very long grating is incapable of exciting the LP_{01} mode since the fields scattered from both ends of the grating will not be in contact, which yields two intensity maxima with equal phase and therefore a low overlap with the LP_{01} mode. The same is true if the grating is too strong for its length. On the other hand, if the grating is too short or not strong enough destructive interference within the grating will yield a reduced out-coupling efficiency and both LP_{01} and $LP_{11,a}$ will couple with lower performance.

As a proof of principle figure 5.15 shows the real part of the transverse electric

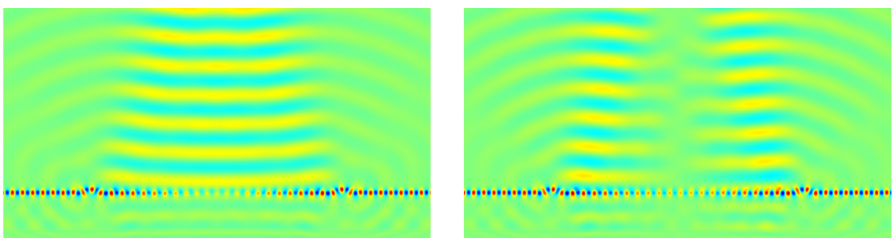

Figure 5.15: Real part of the electric fields of a 1D grating excited from both ends with the fundamental waveguide mode TE_{00} with phase difference $\Delta\phi = 0$ (left) and $\Delta\phi = 180°$ (right) at $\lambda = 1.55\mu m$.

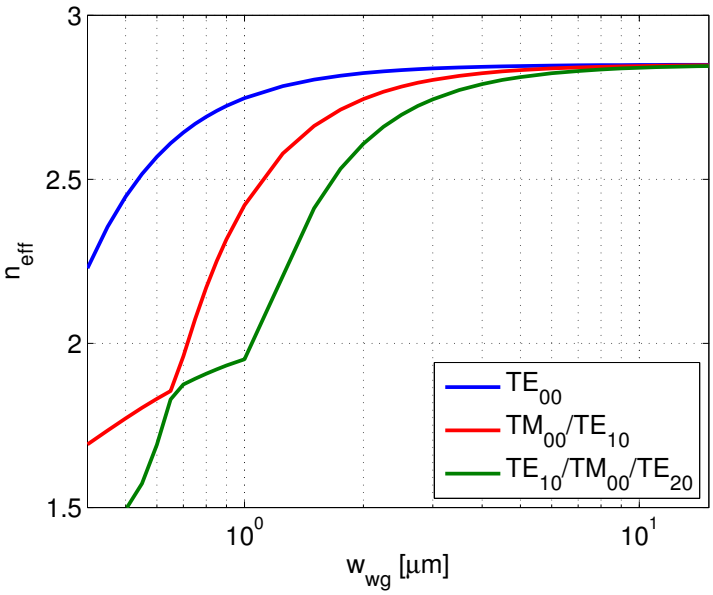

Figure 5.16: Effective refractive indices of the first three guides modes in a nano wire with SiO_2 cladding of height $h_{wg} = 220nm$ as a function of waveguide width w_{wg} at $\lambda = 1.55\mu m$.

fields of a one dimensional grating excited from opposing sides. The incoming fields can be described as E_{TE00} and $E_{TE00} \cdot \exp(-j\Delta\phi)$, respectively, where E_{TE00} is the electric field of the fundamental waveguide mode TE_{00}. In the case of $\Delta\phi = 0$ the setup is symmetric and the scattered field of the grating resembles the LP_{01} fiber mode, whereas for $\Delta\phi = 180°$ the diffracted field is anti-symmetric resulting in the $LP_{11,a}$ fiber mode.

As can be seen, the phase fronts are horizontal as was indicated. The gratings used were not optimized for this operation, but were the same as the presented in chapter 4.2 The only consideration to be made is, that gratings with a low diffraction angle φ in normal operation (excited form only one end) are expected to perform better, as the diffracted field above the grating will show a slower variation of its intensity profile on the way to the fiber.

The excitation of the $LP_{11,b}$ mode follows a different approach. Instead of using a fundamental waveguide mode for each intensity maximum, the first higher order mode TE_{10} of the integrated waveguide can be utilized. Since this mode exhibits two intensity maxima along one transverse dimension and a phase difference of $\Delta\phi = 180°$ between these two, it shares enough properties with the $LP_{11,b}$ fiber mode to couple between them. Analogously to the excitation of the LP_{01} fiber mode through the TE_{00} mode of the integrated waveguide, the TE_{10} mode can be scattered through a grating coupler to excite the $LP_{11,b}$ fiber mode. According to the grating equation 2.8 a grating period Λ_{TE10} can be found, which yields a diffraction angle φ_{TE10} that is equal to the diffraction angle φ_{TE00} of the fundamental waveguide mode in a grating of period Λ_{TE00}. The difference of the two grating periods is ultimately determined by the difference of effective refractive indices of the two modes. Figure 5.16 shows the effective refractive indices of the first three guided modes in nano wires as a function of waveguide width. With the exception of TE_{00} the modes change appearance depending on the waveguide width w_{wg}. The second guided mode (red line) starts as the fundamental TM mode in narrow waveguides,

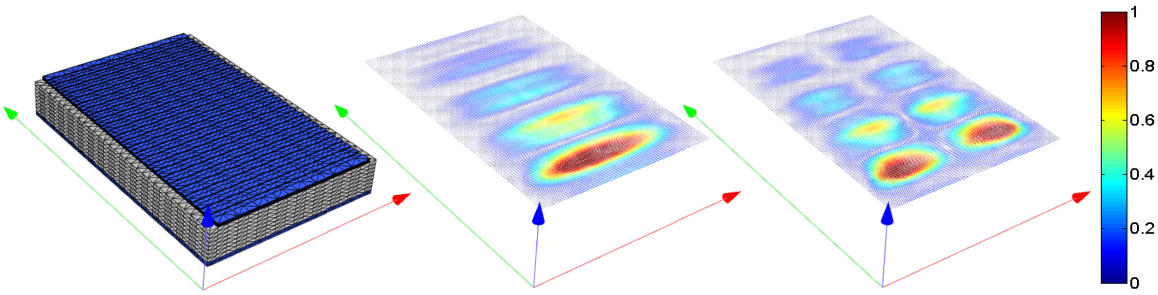

Figure 5.17: Relative field intensity of the scattered field of a standard grating coupler (left) excited by a TE_{00} (center) and a TE_{10} mode (right) at $\lambda = 1.55\mu m$.

but transforms into the TE_{10} mode at $w_{wg} \approx 630nm$. Similarly, the third guided mode (green line) starts as the TE_{10} mode and transforms into the TM_{00} mode and ends up as the TE_{20} mode in large waveguides. It can be seen, that the effective refractive indices all reach saturation in waveguides of $w_{wg} \geq 10\mu m$ at $n_{eff} = 2.85$ for wavelengths of $\lambda = 1.55\mu m$. This circumstance is very fortunate for the application in grating couplers, since here the widths of waveguides usually are in this order of magnitude. The difference in n_{eff} between TE_{00} and TE_{10} at $w_{wg} = 10\mu m$ is only $3 \cdot 10^{-3}$ and therefore negligible. As a consequence, a grating of period Λ has equal scattering characteristics for the TE_{00} and TE_{10} modes, provided w_{wg} is large enough. Therefore a single grating is potentially enough to couple both TE_{00} and TE_{10} modes to a fiber simultaneously. A 3D simulation of a standard grating excited with both modes confirms this expectation. Moreover, not only is the diffraction angle equal in both cases, but the fraction of out-coupled power P_{out} is equal as well, allowing for low differential mode attenuation caused by the device, provided that the field overlaps with the corresponding fiber modes are equal as well. Figure 5.17 shows the electric field scattered by a standard grating coupler, when excited with the TE_{10} mode. As can be seen, the grating excites two very distinct intensity maxima along the transversal direction of the waveguide as it is prescribed by the TE_{10} waveguide mode. In the lateral direction the grating shows an identical behavior to a standard fiber grating coupler for the fundamental waveguide mode.

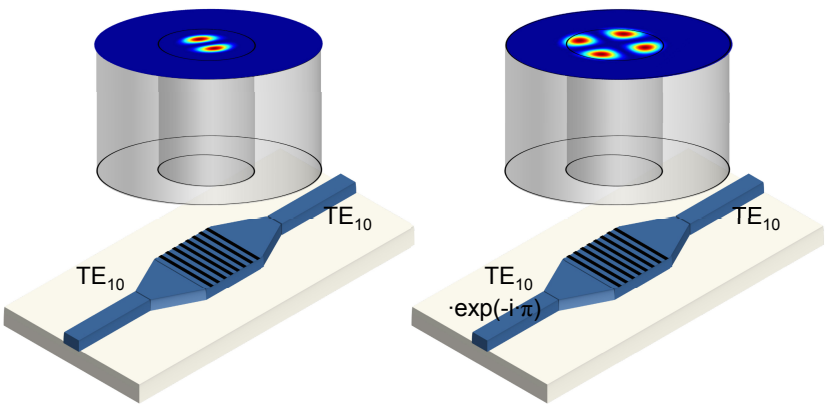

Figure 5.18: Sketch of a fiber grating coupler with two input waveguides located on opposing ends fed with TE_{10} modes with $\Delta\phi = 0$ (left) and $\Delta\phi = \pi$ (right) relative phase difference between them.

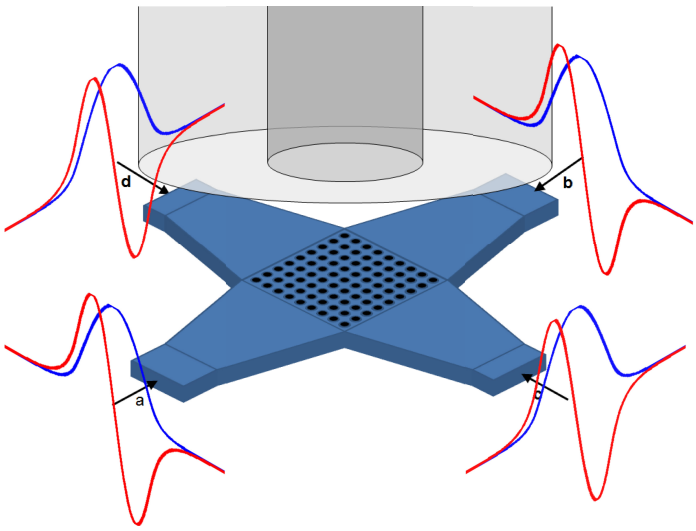

Figure 5.19: Sketch of the complete device capable of exciting the LP_{01}, $LP_{11,a}$, $LP_{11,b}$ and $LP_{21,a}$ modes in both TE and TM polarization.

Since the functionality of exciting the $LP_{11,b}$ mode has to be included in the device for the excitation of the $LP_{11,a}$ and LP_{01} mode shown before, the way of excitation follows the model of feeding the grating from both ends. This way a symmetric scattering of the $LP_{11,b}$ mode to a fiber tilted at $\varphi = 0°$ is ensured here as well.

Of course the phase difference $\Delta\phi$ between the TE_{10} modes in the nano wires has to be zero for the $LP_{11,b}$ mode to be generated. However, the same mechanism, that caused the transformation from LP_{01} to $LP_{11,a}$, can be applied here as well. Again, by assigning a relative phase difference of $\Delta\phi = 180°$ between the incoming modes, the scattered fields from both ends will be prevented from melting together. Therefore four distinct intensity maxima will be generated by the grating in two pairs of equal phase, but a phase difference of 180° between both pairs. The resulting field resembles one of the LP_{21} modes, but has to be neglected in further considerations, since the other member of the LP_{21} mode group, which is obtained through a 45° rotation of the first member of this group, can not be generated in this device. Figure 5.18 depicts the excitation of the $LP_{11,b}$ and $LP_{21,a}$ modes.

A sketch of the complete device is shown in figure 5.19. To allow for coupling in both polarizations, the grating to be used is two dimensional and requires four inputs

In_1	In_2	Input Mode	$\Delta\phi$	Output Mode	Polarization
a	b	TE_{00}	0°	LP_{01}	E_x
a	b	TE_{00}	180°	$LP_{11,a}$	E_x
a	b	TE_{10}	0°	$LP_{11,b}$	E_x
a	b	TE_{10}	180°	$LP_{21,a}$	E_x
c	d	TE_{00}	0°	LP_{01}	E_y
c	d	TE_{00}	180°	$LP_{11,b}$	E_y
c	d	TE_{10}	0°	$LP_{11,a}$	E_y
c	d	TE_{10}	180°	$LP_{21,a}$	E_y

Table 5.1: Table of excitable modes.

labeled from a to d. Each input waveguide guides carries either the fundamental waveguide mode TE_{00} or the first higher order waveguide mode TE_{10} or both at the same time. Opposite input waveguides are always excited equally with the exception of a possible $\Delta\phi = 180°$ phase shift on any of the modes.

A list of all excitable modes together with the necessary input configuration is shown in table 5.1. All fiber modes excited through input waveguides a and b are labeled as E_x modes, while inputs c and d are responsible for the generation of E_y modes. Since the orthogonality of the modes of the integrated waveguides is maintained at all stages in the device, all fiber modes can be excited at the same time and independently of each other. Similar to other gratings presented so far, reciprocity applies here as well, since the device is fully passive. Therefore, the same device can be used to detect the fiber modes of table 5.1.

5.3.2 PIC for TE_{00} and TE_{10} Modes

With the concept of exciting higher order fiber modes by means of feeding a grating coupler with two different modes of the integrated waveguide, the problem of designing a photonic integrated circuit capable of fulfilling that task arises. Since the device relies on the use of the TE_{10} mode of the integrated waveguide, the difficulty in the excitation of higher order fiber modes was partially shifted to the photonic integrated circuit. Not only is the reliable generation of the TE_{10} mode a problem in itself, but almost all devices commonly used in integrated optics (MMIs, gratings, waveguides, etc.) are designed for use with the fundamental waveguide mode only and therefore need adaptation. A schematic of a possible PIC containing all devices necessary for the processing of both TE_{00} and TE_{10} modes, that will yield the required input field configurations shown in table 5.1, is depicted in figure 5.20. To ensure independence of each channel every input field must only excite a single fiber mode. Starting with fundamental waveguide modes, that are coupled from one dimensional grating couplers to the PIC, the fields are transformed into TE_{10} modes for the excitation of the $LP_{11,b}$ and $LP_{21,a}$ modes and passed along to a circuit of MMIs and phase shifting elements, that provide equal fields and correct phases on opposing inputs of the two dimensional few mode grating. For the excitation of

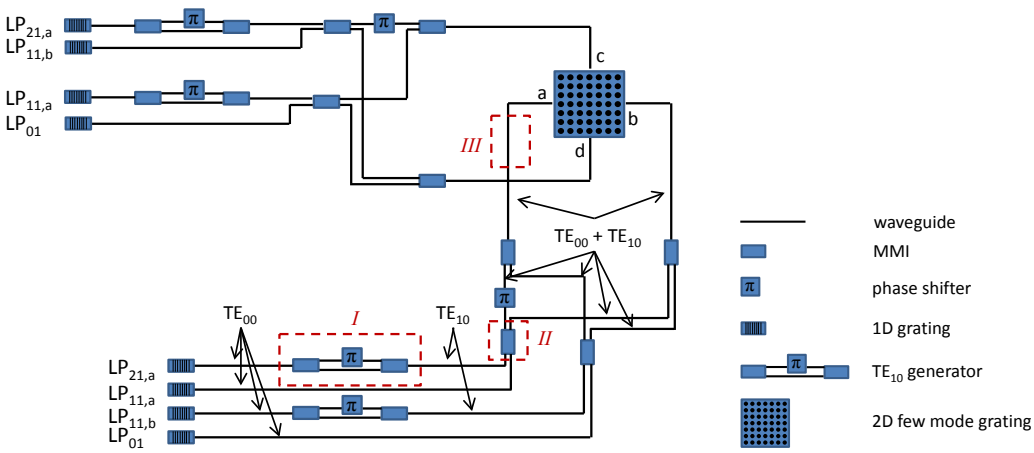

Figure 5.20: Schematic of a photonic integrated circuit for the management of the TE_{00} and TE_{10} modes with respect to the few mode grating coupler shown in figure 5.19.

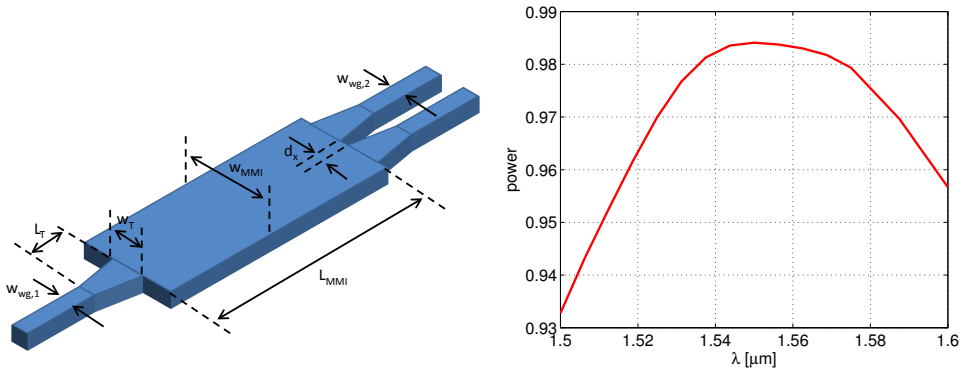

Figure 5.21: Left: Sketch of a 1x2 MMI with all important dimensions. Right: Performance of the MMI ($L_{MMI} = 92.85\mu m$, $w_{MMI} = 10\mu m$, $w_{wg,1} = w_{wg,2} = 500nm$, $w_T = 3\mu m$, $L_T = 20.8\mu m$, $d_x = 2.2\mu m$) as a function of wavelength.

LP_{01} and $LP_{11,a}$ the transformation to TE_{10} is not applied and the input fields are directly passed on. In accordance with table 5.1 those channels, which use ports a and b of the few mode grating, will excite E_x- and those, which are directed to ports c and d are responsible for the generation and reception of E_y polarized fiber modes.

Beside the few mode 2D grating, there are several integrated devices, that need to be redesigned for functionality with the TE_{10} mode or both the TE_{00} and TE_{10} modes. In figure 5.20 these devices are highlighted in red and numbered with *I* to *III*. There are several possibilities, which provide the functionality for structure *I*, that will convert a fundamental waveguide mode into the TE_{10} mode. The device shown here is a MZI based on MMIs, first proposed by Leuthold et al. [90], which includes a degenerated 2x2 MMI, whose output waveguides on one side have a distance $d_x = 0$ and therefore has the appearance of a 2x1 MMI, with an output waveguide of twice the width of the input waveguides, a phase shifting element, that provides a 180° phase shift on one arm of the MZI and a regular 1x2 MMI that acts as a 3dB coupler. The devices can easily be simulated using Eigenmode Expansion. The basic principles of MMIs and approximate estimations of dimensions can be found in [91]. Figure 5.21 shows a sketch of a 1x2 MMI together with its performance as a function of wavelength around the center wavelength of $\lambda = 1.55\mu m$. Due to symmetry both output arms carry the same amount of power, when the input waveguide carries the TE_{00} mode. Figure 5.21 (right) shows the combined power on both arms amounting to approximately 98.6% of the input mode or 0.06dB loss and a 1dB-bandwidth well beyond the C-band. The device is the first part of the TE_{00} - TE_{10} converter as it splits the incoming electric field on both arms of the MZI in equal rations. For further reading on this topic one may refer to [92, 5].

The other MMI, which excites the TE_{10} mode on the output waveguide from two TE_{00} modes with a relative phase difference of $\Delta\phi = 180°$ on the two input waveguides can equally be simulated. Figure 5.22 shows the device and a plot of its performance in dependency of the MMI-length L_{MMI}. The power coupled to the TE_{10} mode, when the MMI is fed with TE_{00} modes with a relative phase difference of $\Delta\phi = 180°$ has its maximum at $L_{MMI} = 183.1\mu m$. The efficiency is 80% ($\approx 0.96dB$ loss). The input waveguides are aligned with the edges of the MMI section and are therefore at maximum distance to each other. Since the distance between output waveguides is $d_x = 0$ its width $w_{wg,2} = 1\mu m$ is twice the width of the input waveguides $w_{wg,1} = 500nm$. The intensity distribution inside the MMI section

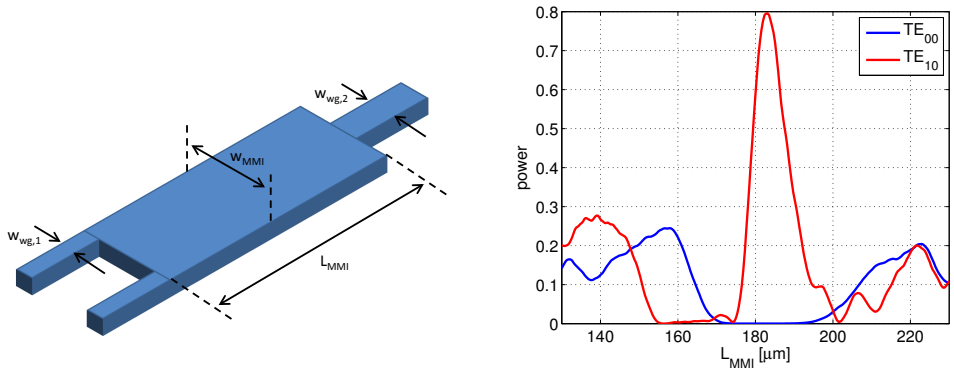

Figure 5.22: Left: Sketch of a degenerated 2x2 MMI with distance $d_x = 0$ between output waveguides. Right: Performance of the MMI as a function of length L_{MMI} at $\lambda = 1.55\mu m$ ($w_{MMI} = 10\mu m$, $w_{wg,1} = \frac{1}{2}w_{wg,2} = 500nm$).

of the degenerated 2x2 MMI of length $L_{MMI} = 450\mu m$ can be seen in figure 5.23. In the case of TE_{10} excitation (top left) the desired field distribution can be recognized at the length specified in plot 5.23 (right) and integral multiples thereof, while in the case of TE_{00} excitation (bottom left) this length is different, as suggested by the difference of the effective refractive indices of the modes in question (c.f. figure 5.16). Therefore, this device cannot be used to either pass on the TE_{00} mode or TE_{10} mode, depending on the relative phase difference between the modes on the input waveguides, but is only functional for one or the other at a fixed length L_{MMI}. For a more detailed analysis of this device see [93].

The phase shift, that is required for the $\Delta\phi = 180°$ phase difference between the fields in the arms of the MZI and in other positions in the PIC (see figure 5.20), can be achieved using different approaches. The simplest way of doing so is to introduce a difference in optical path length. However, this requires very precise knowledge of the effective refractive indices of the guided modes in real waveguides (straight and curved) and is very intolerant towards manufacturing inaccuracies. Moreover, this approach is not adjustable after fabrication and therefore not suitable for the precision required for an exact phase shift. By having free carriers present in one of the waveguides, the refractive index of silicon can also be changed. In [94] the change of the complex refractive index is described in dependency of doping concentration

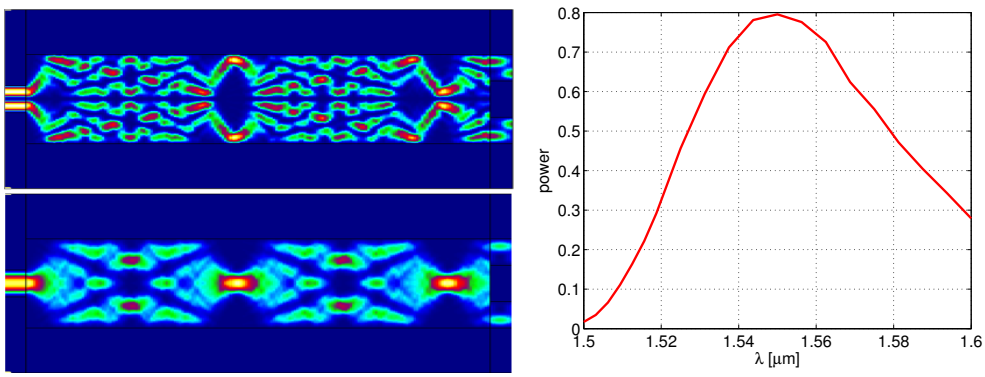

Figure 5.23: Left: Intensity distribution inside the MMI region of a degenerated 2x2 MMI of length $L_{MMI} = 450\mu m$. Right: Performance of the MMI as a function of wavelength ($L_{MMI} = 183.1\mu m$, $w_{MMI} = 10\mu m$, $w_{wg,1} = \frac{1}{2}w_{wg,2} = 500nm$).

and wavelength. It is obvious, that the introduction of free carriers within reach of the mode field in a waveguide will result in additional losses. Although these might be very small, if free carriers are sparse, implementing a diode structure requires additional layers for the mask layout adding to the cost of the device. Additionally, a diode structure presumes rib waveguides, which as will be shown later are not well suited for multimode operation. The means of introducing phase changes used here is through the thermo-optic effect. Although in principle not as fast as electro-optical effects, the thermo-optic effect can be made use of very easily and reliably through ohmic heating. Only one additional layer for metal deposition on top of the waveguide is required, that will form a small metallic wire and two contact pads, between which a voltage will be applied. In silicon the thermo-optic effect is as high as $\frac{dn}{dT} = 1.9 \cdot 10^{-4}\mathrm{K}^{-1}$ at $\lambda = 1.55\mu m$ and room temperature [95, 96]. Assuming a length of the MZI arms of 1mm, the required change in effective refractive index for a 180° phase shift compared to a unchanged waveguide amounts to $\Delta n \approx 8 \cdot 10^{-4}$, which can be achieved with a minor amount of temperature variation (Note, that this approximation is not quite valid, as the effect on the effective refractive index is much smaller than the effect on refractive index of the material itself, when a change in temperature is applied. For a more reliable calculation a mode solver has to be used on a waveguide with the added refractive index variation of the thermo-optic effect. Nonetheless, the approximation shows, that the desired phase shift is easily within reach using the thermo-optic effect). An additional concern using this approach is, as in the case of doped waveguides, the introduction of losses through free carriers within the vicinity of the mode field. However, unlike the waveguide diode structure, where carriers are located directly inside the waveguide, heaters are placed distanced from the waveguide and rely on the thermal conductivity of the surrounding material. Within the standard manufacturing process, PICs are protected by a $1.3\mu m$ thick SiO_2 layer, on which the heaters are placed, which results in negligible additional losses. For those reasons, ohmic heaters were used for the first realization of the device.

Alternative solutions to structure I (c.f. figure 5.20) are feasible as well: A very straight forward conversion from TE_{00} to TE_{10} mode can be achieved using an asymmetric co-directional coupler between two nano wires of different width. Phase matching can be achieved between the two modes, if the TE_{10} mode is guided in a wide waveguide and the TE_{00} mode in a thin one. Exact values can be found using figure 5.16. With a waveguide gap of 150nm, the coupling length of the directional coupler is approximately 40μm ruling the device way more compact than the MZI device used in this work. However, the same problem as described for the polarization converter applies here: Small inaccuracies can severely inhibit the functionality of the device. Another way of generating the TE_{10} mode is by means of adiabatic tapering from the fundamental TM mode of a thin waveguide. As mentioned before at a waveguide width of around $630nm$ the conversion from TM_{00} to TE_{10} takes place, which means a gradually widened waveguide will yield this functionality. This method is very tolerant with respect to fabrication, very efficient and yields a huge bandwidth, depending on the length of the taper. However, the use of TM modes renders this device unfavorable, since TM modes tend to be more lossy than their TE counterpart and coupling to small waveguides as they are used here cannot be done efficiently so far using reasonably complex structures. A third alternative is the use of asymmetric Y-junctions, that takes TE_{00} modes on two of

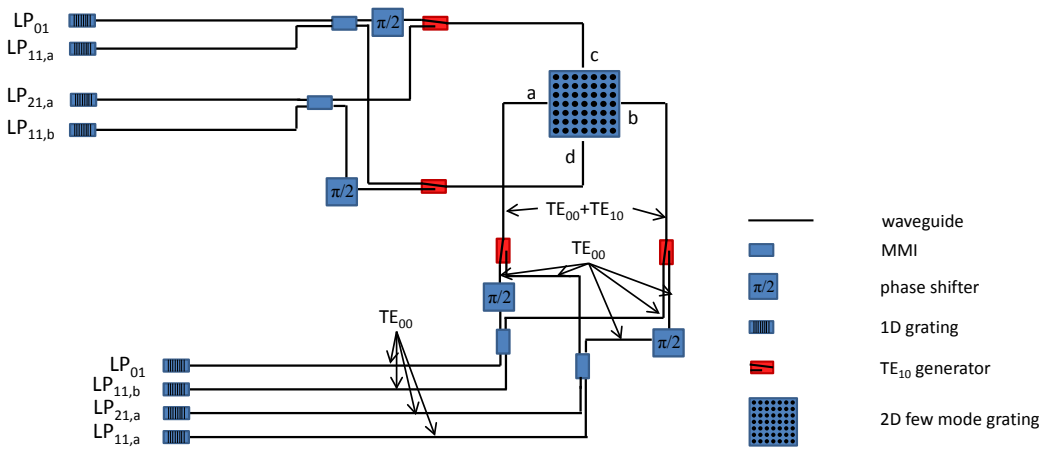

Figure 5.24: Schematic of an alternative photonic integrated circuit for the management of the TE_{00} and TE_{10} modes with respect to the few mode grating coupler shown in figure 5.19.

the three arms and converts one of them into the TE_{10} mode and passes along the other on the third arm. A detailed analysis of Y-junctions [97] and this devices in particular was conducted in [98]. The combined functionality of converting a TE_{00} mode of an input waveguide into a TE_{10} mode on the output waveguide and passing along the TE_{00} mode of another input waveguide to the output waveguide is a shared property of all alternatives presented here. This feature enables an alternative, simplified PIC that is depicted in figure 5.24. Instead of generating the TE_{10} mode right after coupling to the PIC, the higher order mode is excited in the very last stage before the few mode grating and therefore alleviates the task of handling this mode in MMIs of various types. In future work this alternative PIC might be preferential to the one shown in figure 5.20, provided that one of the alternative devices for the TE_{10} generation can be realized within fabrication tolerances in an efficient manner. Considering the drawbacks of most of these devices, the asymmetric Y-junction seems to be the best candidate for this application. As suggested in [98] such a structure can achieve an efficiency of well above 90% while maintaining a crosstalk below -15dB around the wavelength $\lambda = 1.55\mu m$. As an additional benefit, this PIC is in contrast to the one shown before completely lossless, as the last 2x1 MMI stage before the few mode grating is avoided as well.

The 2x2 MMI labeled as structure II in figure 5.20 acts as a 3dB coupler for both TE_{00} and TE_{10} modes. Figure 5.25 shows a sketch of the structure together with its performance as a function of device length L_{MMI}. Since on the input side modes are guided in individual waveguides, one is of lower width and has to be tapered to be equal to the waveguide carrying the higher order mode. It is noteworthy, that this MMI is unusually long ($L_{MMI} = 372\mu m$) for MMIs based on nano wire technology, but figure 5.25 (right) shows optimal performance at this length. In contrast to figures 5.21 and 5.22 the plot does not shows the combined output power on both arms but rather the relative power on each arm in an individual mode. One can clearly recognize the antisymmetric nature of the device, when moving away from the optimum. Due to the differing phase constants of the TE_{00} and TE_{10} modes in the input waveguides, the optimal coupling length of the MMI differs slightly ($L_{MMI} = 374\mu m$ for TE_{00} vs. $L_{MMI} = 372\mu m$ for TE_{10}). Since the overall performance is for the TE_{10} mode is slightly lower for any length L_{MMI} near the

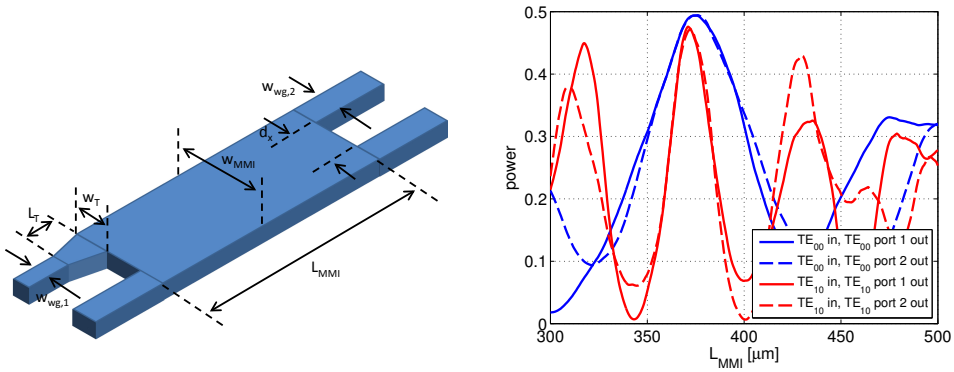

Figure 5.25: Left: Sketch of a 2x2 MMI for simultaneous operation with TE_{00} and TE_{10} mode with all important dimensions. Right: Performance of the MMI ($w_{MMI} = 10\mu m$, $w_{wg,1} = 500nm$, $w_{wg,2} = 1\mu m$, $w_T = 1\mu m$, $L_T = 20.8\mu m$, $d_x = 8\mu m$) as a function of MMI length L_{MMI} at $\lambda = 1.55\mu m$.

global maximum, the optimal length for this mode is chosen as the defining device length. Once again, the transverse position of the waveguides is set at maximum distance by having them aligned with the boundary of the MMI section.

Lastly, components summarized as structure III in figure 5.20 - the waveguides themselves - are subject to a redesign. As indicated in the design of the MMIs a waveguide width of $w_{wg,2} = 1.0\mu m$ is selected for waveguides, which need to guide the TE_{10} mode. Figure 5.16 shows any width above $w_{wg} = 630nm$ to be sufficient to guide this mode at a wavelength of $\lambda = 1.55\mu m$. The third guided TE mode appears at $w_{wg} \approx 1.1\mu m$ and therefore the waveguide should be below this width to avoid unwanted coupling, that may be caused by rough surfaces or other imperfections of the waveguide. Conveniently, the design of the degenerated 2x2 MMI, that excites the TE_{10} mode (c.f. figure 5.22) dictates a waveguide width of the output waveguide that is twice the size of the input waveguides, resulting in a waveguide width of the single mode nano wires of $w_{wg,1} = 500nm$. This value allows low loss transmission and is the standard value used for all waveguides used throughout this work (unless otherwise mentioned).

Although mostly irrelevant for other applications, the choice of waveguide type is crucial in the context of mode multiplexing. There are two reasons, why nano wires were chosen over rib waveguides for this structure. The first one can be seen in the imaginary part of the effective refractive index of the higher order modes in rib waveguides. The TE_{10} mode in rib waveguides does not appear abruptly as it is the case in nano wires, when increasing the waveguide width, but is rather always present, when the slab region extends to infinity. The difference between the *guided* fundamental waveguide mode and the *unguided* TE_{10} mode is, that the losses are several orders of magnitude higher for the TE_{10} mode than for the TE_{00} mode and will not vanish at any waveguide width. Therefore, rib waveguides are not well suited for operation with higher order modes.

The other reason why nano wires are preferable over rib waveguides is connected with the use of MMIs. In principle one could find a waveguide width large enough to yield tolerable losses in multimode operation. However, with the size of waveguides the MMIs grow equally wide and their length is proportional to their width squared, which will result in unnecessary losses and sacrifices compactness.

Further related to waveguides is the behavior of the TE_{10} mode in bends and

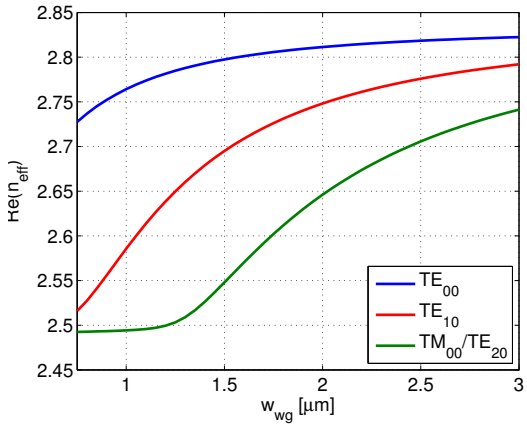

Figure 5.26: Real part of the effective refractive indices of the first three modes of a nano rib waveguide of height $h_{wg} = 220nm$ and etch depth $h_e = 70nm$ as a function of waveguide width.

waveguide tapers. It is to be expected, that higher order modes will experience more losses in bends compared to the fundamental waveguide mode, due to weaker confinement and higher susceptibility to waveguide imperfections. The same is of course also true for straight waveguides and tapers. However, in tapers a different reason for losses occurs in the form of coupling to other modes. Since the difference in effective refractive indices decreases for the higher order modes and coupling between modes is proportional to $\kappa_{12} \propto \frac{1}{n_{eff,1}^2 - n_{eff,2}^2}$, modal crosstalk becomes more of a problem, which may be compensated by a softer variation of waveguide geometry and thus a longer taper. Figure 5.27 (left) shows the imaginary part of the effective refractive index of a circularly bent waveguide for the TE_{00} and TE_{10} modes as a function of bend radius r_B. The results were obtained using a mode solver operating in a cylindrical coordinate system, where the direction of propagation is along the angular axis. It can be seen, that $Im(n_{eff})$ is 5 to 10 times higher for the TE_{10} mode than for the TE_{00} mode and starts to increase rapidly for band radii $r_B < 20\mu m$, while the TE_{00} mode becomes lossy for $r_B < 8\mu m$. To be on the safe side, a bend radius of $r_B = 50\mu m$ is chosen for both waveguide widths ($w_{wg} = 500nm$ and

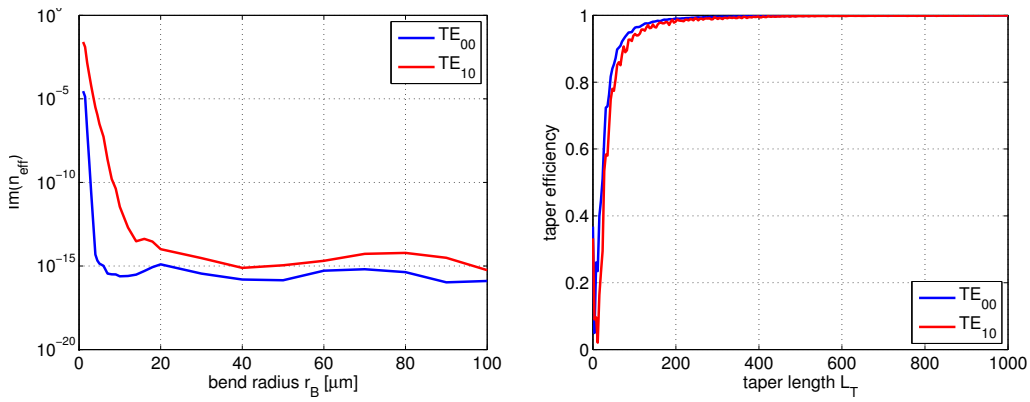

Figure 5.27: Left: Imaginary part of the effective refractive index of the TE_{00} (blue) and TE_{10} (red) modes as a function of bend radius r_B in a nano wire of width $w_{wg} = 1\mu m$ at $\lambda = 1.55\mu m$. Right: Performance of a nano wire waveguide tapered $w_{wg,1} = 1\mu$m to $w_{wg,2} = 10\mu$m as a function of taper length L_T at $\lambda = 1.55\mu m$.

$w_{wg} = 1\mu m$). It should be noted, that values as low as 10^{-15} are prone to numerical noise especially for the calculation of loss. A very high resolution across the entire computational domain is required to obtain accurate fields near the boundary, where losses are originating from, rendering the computation of complex refractive indices in waveguides with low loss numerically very expensive. Figure 5.27 (right) shows the performance of a waveguide taper, that is used for the transformation of the waveguide geometry from $w_{wg,1} = 1\mu m$ as used throughout the photonic integrated circuit to $w_{wg,2} \approx 10\mu m$ required by the few mode grating, as a function of its length L_T. The taper efficiency is defined as the fraction of power, that remains inside the mode it was excited with. It is called adiabatic if no power is transferred to another mode. Although the taper performs slightly worse with TE_{10} excitation, the difference to TE_{00} excitation is negligible and from a taper length $L_T > 400\mu m$ the power inside the respective mode lost is smaller than 0.5% and stays at that level for any length larger than that.

5.3.3 Simulation Results

The grating itself is optimized using a full three dimensional model of the device. Due to the asymmetry of the $LP_{11,b}$ fiber mode with respect to the transversal direction of the grating, a reduction to a smaller representation of the structure is not possible. The aim of the optimization process involves three criteria: First,

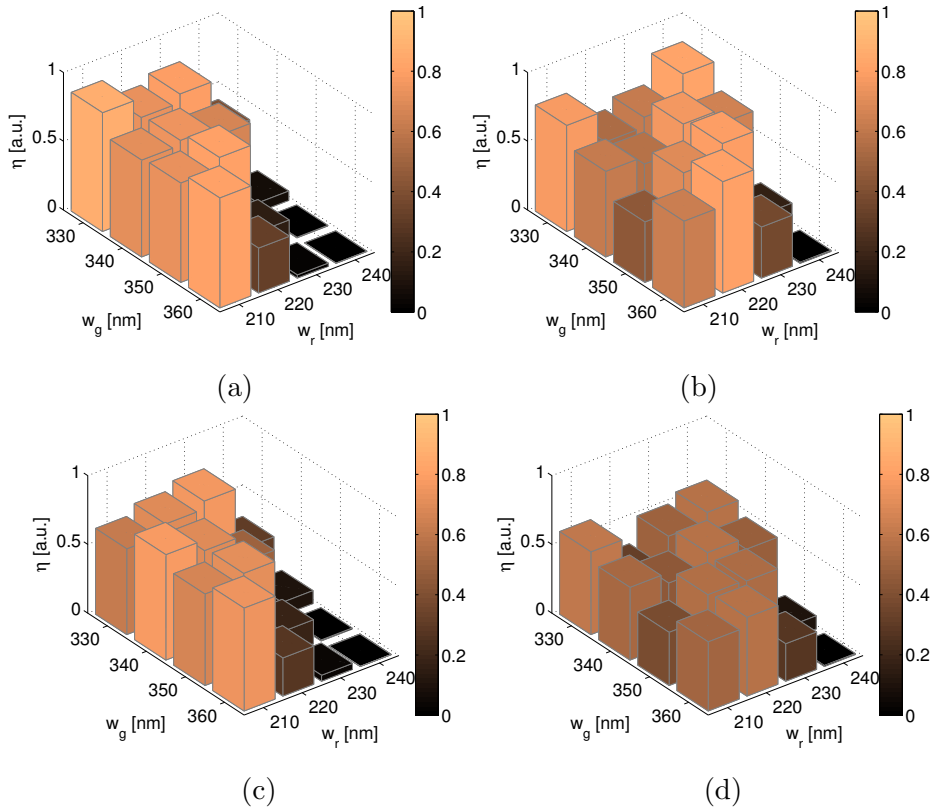

Figure 5.28: Field overlaps η between (a) LP_{01} fiber mode and TE_{00}, $\Delta\phi = 0°$ input field, (b) $LP_{11,a}$ and TE_{00}, $\Delta\phi = 180°$, (c) $LP_{11,b}$ and TE_{10}, $\Delta\phi = 0°$, (d) LP_{21}, $\Delta\phi = 180°$ as a function of w_g and w_r for a grating of 21 periods with $h_e = 210nm$ and $h_{epi} = 150nm$ at $\lambda = 1.55\mu m$.

the out-coupled power (P_{out}) of the grating needs to be high. Therefore, as seen in the previous sections, an epitaxial layer on top of the grating is used to increase directionality. Second, the overlap η between input field combinations and fiber modes as shown in table 5.1 needs to be high, while at the same time crosstalk (i.e. overlap with unintentionally excited modes) remains nearly zero. Third, the differential mode attenuation (i.e. the difference in coupling efficiency for different modes) is minimized.

At first the optimal number of grating periods is obtained, using the grating of chapter 5.1 and a parabolic graded index few mode fiber (profile exponent $g = 2$) with a LP_{01} spot size radius of $5.5\mu m$ [89]. The considerations to be made were mentioned in the beginning of this section. A good balance between excitability of the LP_{01} and $LP_{11,a}$ modes was reached with 21 (resulting in 12μm $\times$ 12μm footprint) grating periods. For the second step of optimization a parameter scan across groove width w_g, ridge width w_r and etch depth h_e was conducted once again, where again an etch depth of $h_e = 210nm$ was found to yield optimal results and additionally ensures integrability with other gratings on the same process.

Figure 5.28 shows the field overlaps between input field configurations according to table 5.1 and their intended fiber modes as a function of groove width and ridge width. The performance of the LP_{21} fiber mode is as mentioned before not regarded for the overall performance of the device but is computed nonetheless and shown in figure 5.28d for reference.

On average, the highest performance is displayed for grating periods of $\Lambda = 570nm$. Shorter grating periods experience only a slightly higher mode mismatch with LP_{01} and $LP_{11,b}$ modes while overlap with the $LP_{11,a}$ drops considerably. For larger grating periods performance drops rapidly across all modes. Overall, a field overlap between 70% and 80% is achievable with slightly higher overlaps for selected modes but lower performance on average. Since, as mentioned earlier, a balanced performance across all modes is aimed for, gratings, which display a minimal differential mode attenuation are preferred over gratings with prominent coupling efficiency on singular modes. The out-coupled power P_{out} can be seen in figure 5.29. Unfor-

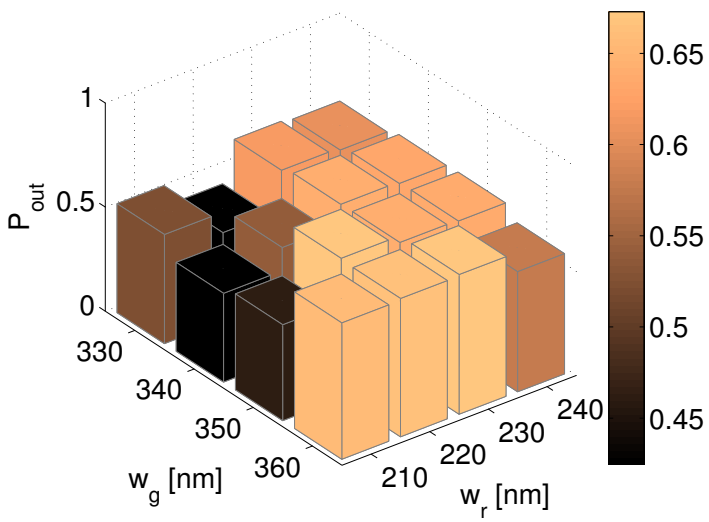

Figure 5.29: P_{out} as a function of w_g and w_r for a grating of 21 periods with $h_e = 210nm$ at $\lambda = 1.55\mu m$.

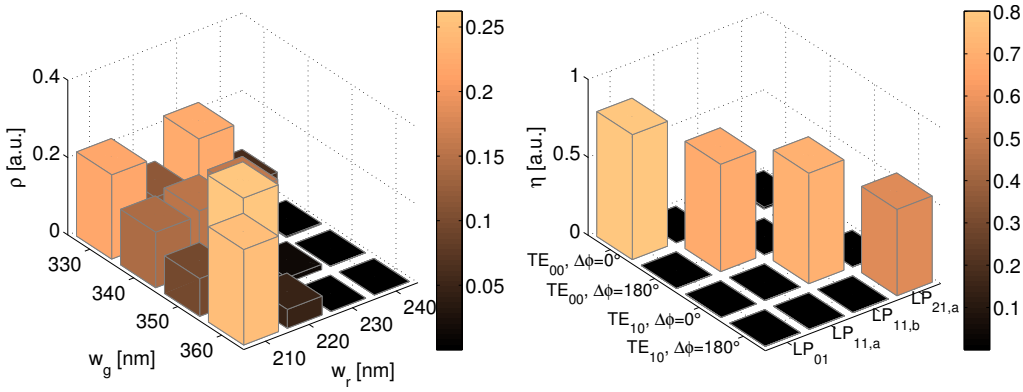

Figure 5.30: Left: Figure of merit ρ as a function of w_g and w_r at an etch depth of $h_e = 210nm$ and $\lambda = 1.55\mu m$. Right: Overlaps of all possible input field combinations of a grating with $w_g = 350nm$, $w_r = 220nm$ and $h_e = 210nm$ and fiber modes LP_{01}, $LP_{11,a}$, $LP_{11,b}$ and $LP_{21,a}$ at $\lambda = 1.55\mu m$.

tunately, its performance curve shows an inverse behavior to the field overlaps as it decreases for smaller grating periods than $\Lambda = 570nm$ and remains nearly constant for larger ones. Therefore, it can be concluded, that the overall coupling efficiency performs best at $\Lambda = 570nm$.

In order to have a single value, that describes all performance parameters, the figure of merit $\rho = P_{out} \cdot \eta_{LP01} \cdot \eta_{LP11,a} \cdot \eta_{LP11,b}$ is introduced as a combined performance of the grating, where η_m describes the field overlap between fiber mode m and the corresponding input field combination in the integrated waveguides (c.f. table 5.1) and P_{out} is the usual out-coupled power obtained from a regular scattering simulation (i.e. the grating is excited from one end with the fundamental waveguide mode). The values of ρ are shown in figure 5.30. Clearly, the maximum of ρ is located at $w_g = 350nm$ and $w_r = 220nm$, indicating a good performance on all modes and a high out-coupling efficiency. Reasonably well does also the combination of $w_g = 360nm$ and $w_r = 210nm$ perform, although on close inspection the decreased performance almost exclusively originates from the reduced coupling efficiency to the $LP_{11,a}$ mode (c.f. figure 5.28 (b)), giving the device a larger mode dependency. The same is true for gratings with $w_g = 330nm$ and $w_r = 210nm$ and a lower performance of the $LP_{11,b}$ mode. In addition, the out-coupled power is more than 10% worse at these values compared to the one found at $w_g = 350nm$, $w_r = 220nm$. Generally, it can be seen, that gratings with large periods are impaired by a reduced field overlap, while shorter periods indicate low out-coupled power. The detailed performance of the grating exhibiting the maximum of ρ is also depicted in figure 5.30 (right), where the field overlaps between the scattered fields of all possible input field combinations and fiber modes is displayed. Not only is the overlap on the main diagonal high, which was aimed for with the considerations made so far, but also the cross talk to other modes is almost zero and can not be distinguished from numerical noise. The overall coupling efficiencies are -2.7dB (LP_{01}), -3.3dB ($LP_{11,a}$), -3.2dB ($LP_{11,b}$) and -4.3dB ($LP_{21,a}$)

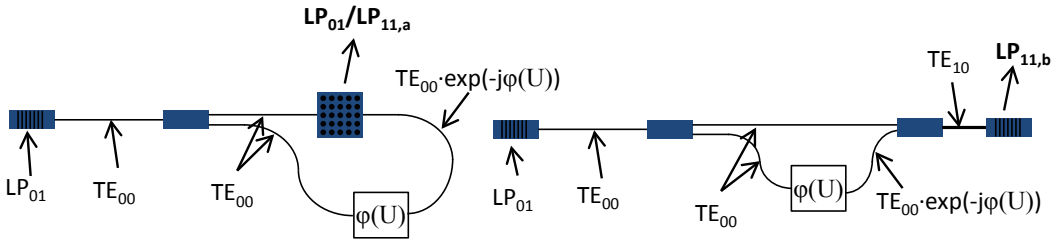

Figure 5.31: Isolated PICs for the sampling of modes in the measurement setup. Left: For the excitation of $LP_{01}/LP_{11,a}$, right: For $LP_{11,b}$.

5.3.4 Measurement

Characterization of the grating was conducted by sampling of the intensity profile of the scattered field in a plane above the grating. In principle the measurement setup is equal to the one described in chapter 3.2, with the exception of the fiber contacting the two dimensional grating coupler, which is replaced by a lensed fiber with the spot size diameter of $w_0 = 3.3\mu m$ at $\lambda = 1.55\mu m$. This allows for a more accurate sampling of the field compared to a standard single mode fiber. The fiber is steered across the grating by Piezo elements in a Cartesian grid of approximately 400nm distance between sampling points. At each point the power coupled to the fiber, which is mounted strictly vertical, is recorded.

For electrical contacting of the phase shifting elements contact pads with an area of $100\mu m$ x $100\mu m$ were placed on the chip and photonic protection layers were locally removed to allow for an external connection. Metallic wires of 500nm x 1mm size are used for ohmic heating of selected waveguides to provide for the necessary phase shift through the thermo-optic effect. To avoid unnecessary losses, the heaters are placed on top of the oxide cladding, i.e. $1.3\mu m$ above the waveguide layer. Contact needles were used to establish a fast and easy connection to an external power supply and a multimeter. The electric resistance of the circuit including needles, contact pads and heater was measured to be approximately 130Ω. Sampling of the field was conducted stepwise for different voltages to obtain the evolution of the scattered fields.

The diffracted fields for the excitation of the LP_{01} and $LP_{11,a}$ modes are shown in figures 5.32 and 5.33. By tuning of the voltage U used to control the heater, which ministers the phase shift $\Delta\phi$ between input arms a and b (c.f. figure 5.31 (left) and table 5.1), the evolution from LP_{01} to $LP_{11,a}$ fiber mode and back again is clearly recognizable. The voltage was varied from 0V to 2.4V in 0.1V steps. The closest resemblance of the LP_{01} field profile is not shown at $U = 0V$, indicating a slight inconsistency in the nature of the input waveguides, in spite of a fully symmetrical setup. The cause for this asymmetry is most likely due to fabrication tolerances. Instead at $U = 2.2V$ the scattered field is closest to the LP_{01} fiber mode and shows a e^{-1} spot size diameter of $w_0 = 10.3\mu m$ in a plane approximately $5\mu m$ above the grating.

At $U = 1.2V$ the $LP_{11,a}$ mode is apparent, which means that a phase shift of $\Delta\phi = 180°$ is approximately the result of that voltage. The e^{-1}-spot size diameter of this mode is with $d_0 = 14\mu m$ slightly larger than the one of the LP_{01} mode.

It must be said, though, that the wavelength used for the generation of these modes was red shifted by 50nm from the design wavelength to $\lambda = 1.6\mu m$. The

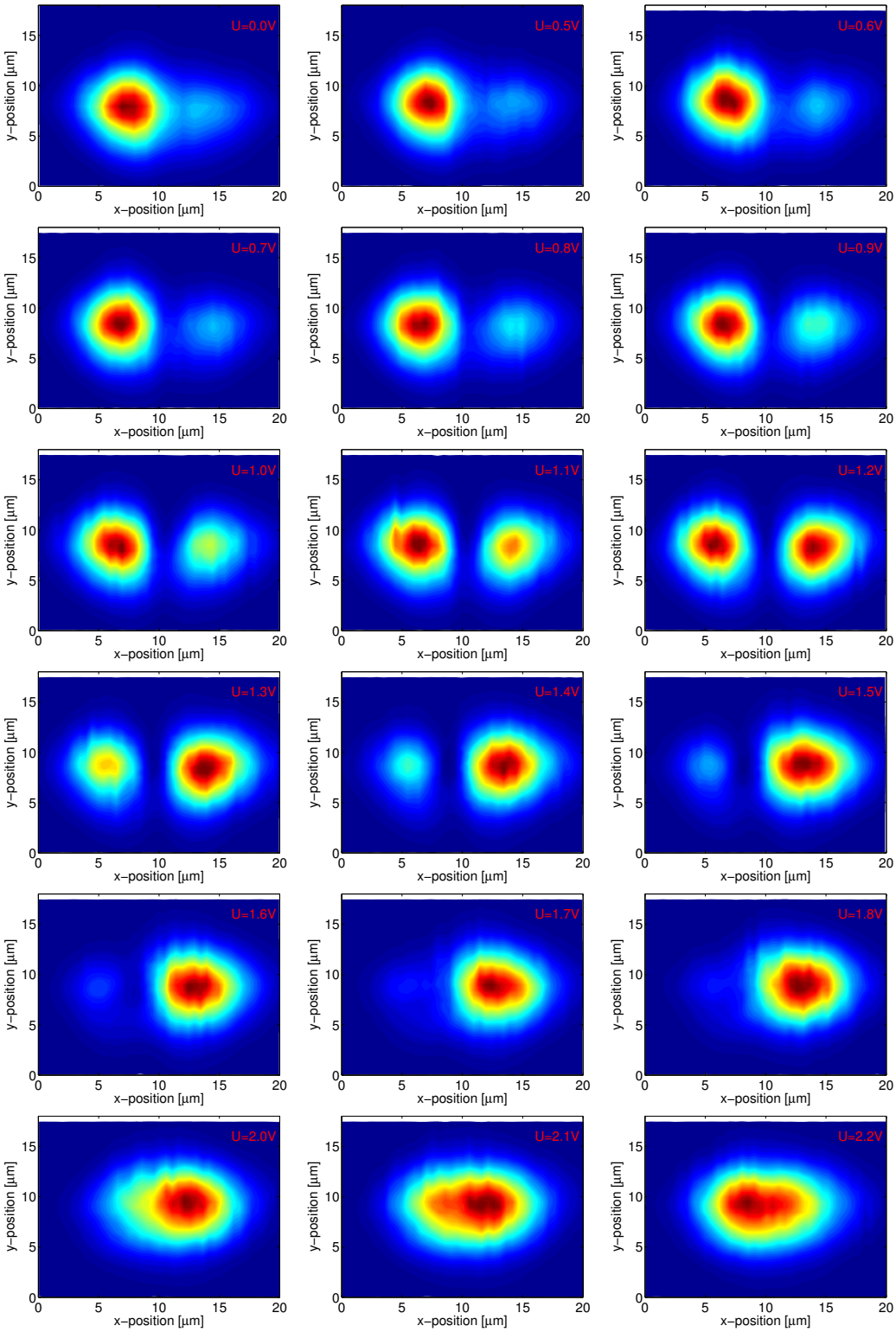

Figure 5.32: Intensity field profiles for heating voltages ranging from 0V to 2.2V, showing the evolution of the diffracted field from LP_{01} to $LP_{11,a}$ in $5\mu m$ height above the grating at $\lambda = 1.6\mu m$.

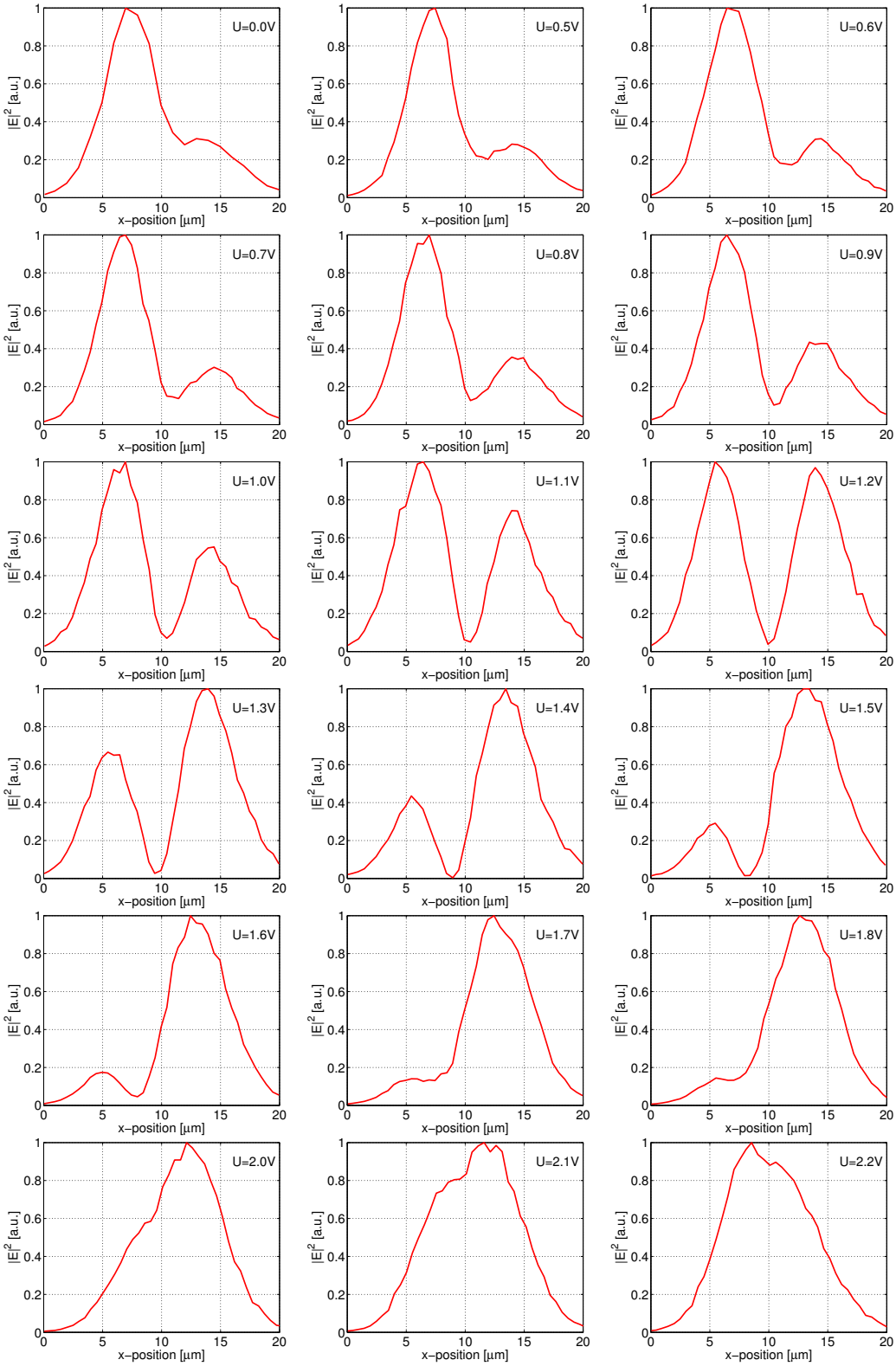

Figure 5.33: Cross sections of the corresponding field profiles shown in figure 5.32.

reason for that can be seen in figure 5.34, where scanning electron microscope images of the grating coupler are shown. First it can be seen, that the etches are not rectangular as designed, but show a very strong rounding of the corners to the point, where the etches are almost circular and second the measured dimensions of the etches vary strongly within the grating and differ partially from the design values. As was mentioned in chapter 5.1 the etch shape has a strong influence on the performance and scattering angle of the grating, giving rise to the large wavelength shift seen here.

The scattered field resembling the $LP_{11,b}$ mode - excited through the PIC depicted in 5.31 (right) - is shown in figure 5.35 together with the other two excitable modes. Coincidentally, no voltage was required in the MZI structure for the generation of the TE_{10} mode of the integrated waveguides, as the path difference in the MZI arms happened to be sufficient by itself. In contrast, when a voltage was applied several side maxima appeared, that could not be attributed to any fiber mode. It is evident though, that one of intensity maxima of the $LP_{11,b}$ mode located at lower y-position carries less power than the other one. In contrast to the upper maximum, which was in the TE_{10} generator only guided through straight waveguides, the field part constituting the lower maximum experienced waveguide bends and the heating structure, causing presumably losses, which resulted in the slight asymmetry of the intensity profile shown in figure 5.35.

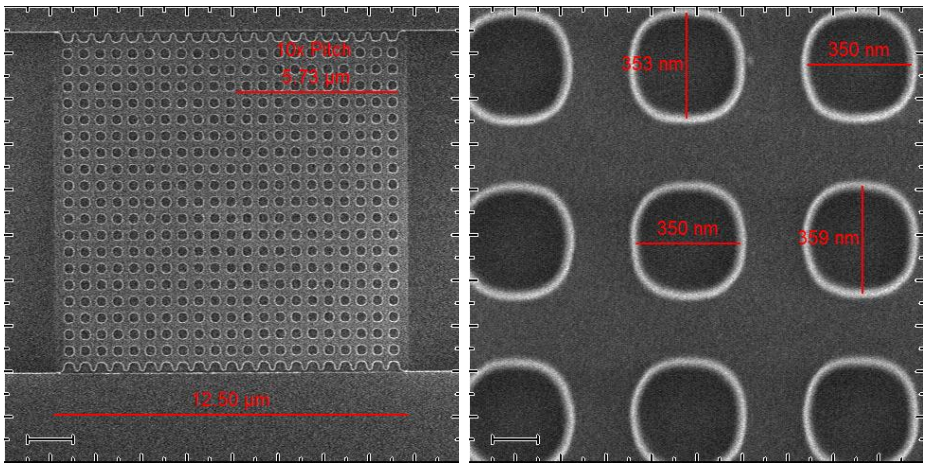

Figure 5.34: Scanning electron microscope images of the grating coupler.

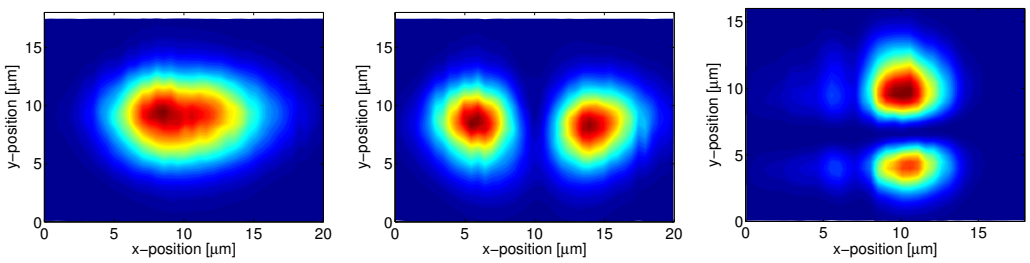

Figure 5.35: Intensity field profiles diffracted by the grating coupler, resembling the LP_{01}, $LP_{11,a}$ and $LP_{11,b}$ fiber modes.

Chapter 6

Summary

Several grating designs for fiber-chip coupling have been analyzed. By means of simulation mostly based on the finite element method grating designs with increasing performance and for different purposes were developed and realized using deep UV lithography. Measurement results show a good agreement with predicted performances and convergence of the numerical method attest a high accuracy to the simulation.

In chapter 4 one dimensional grating couplers were presented with increasing performance and complexity. Starting with the simplest design possible, a grating coupler for the operation around the wavelength of $\lambda = 1.31\mu m$ was shown, which exhibits nearly -3dB coupling efficiency and a -1dB bandwidth of 23nm. Despite operating at such a small wavelength, the dimensions of the grating are still easily within range of manufacturability. With an etch depth of 70nm co-integration of the grating with nano-rib waveguides on a single etch step is possible, resulting in a very low cost device. The grating period of Λ =480nm yields an optimal coupling angle $\varphi = 6°$ for the design wavelength.

The following grating design recognizes the main source of loss in fiber-chip coupling and improves on the previous design by introducing an additional epitaxial mono-crystalline silicon layer on top of the grating, which increases directionality and therefore the overall performance of the grating. Coupling efficiencies of -1.7dB were simulated and measured at the center wavelength of $\lambda = 1.55\mu m$. In view of the numerically expensive task of designing two dimensional gratings, the coupling angle was subject to minimization and was with $\varphi = 4°$ (without oxide cladding) and $\varphi = 6°$ (with oxide cladding) very low. The -1dB bandwidth was in good agreement with the simulation measured to be approximately 25nm.

Subsequently, a more complex grating structure based on 400nm waveguides was shown, that besides having an increased directionality as the previous grating, features a secondary etch step of several periods to yield a higher field overlap between diffracted field and fiber mode. The overall performance of the grating was thus improved to -1.3dB coupling efficiency at the cost of a more taxing fabrication process.

Pursuing the previous approach, the limit of achievable coupling efficiency was investigated by analyzing gratings with arbitrary non-uniform dimensions. Advanced search algorithms were used to optimize grating structures with a large number of degrees of freedom. It was found, that chirp has only a minor influence on the grating performance, but a variation of etch depth yields large benefits to the grat-

ing's coupling efficiency. -1.1dB were simulated for a grating with linear variation of etch depth, groove width and ridge width from first to last grating period. By allowing a variable epitaxial layer height coupling efficiencies of as high as -0.7dB are achievable, without resorting to bottom reflectors.

In chapter 5 two dimensional grating couplers were investigated. Starting with results obtained from the optimization of one dimensional gratings in chapter 4.2, a two dimensional design with a simulated coupling efficiency of -3dB was presented. The measured performance amounted to -5.8dB. It was shown, that the form of the grating etches has a large influence on the performance of the device and although harder to fabricate rectangular etches are preferable to rounded etches.

The following section aimed to solve the symmetry problem of the alignment of the two dimensional grating with the fiber coupled to. Through shear of the grating etches the diffracted field was furnished with an angle in transverse direction, allowing the fiber to be placed slightly out of plane with the propagation direction of the grating and thus allowing for an optimal coupling from both grating arms. It was found, that a shearing angle of 2° is sufficient for a fully symmetrical alignment of fiber and grating coupler.

Chapter 5.3 shows a grating for the excitation of several higher order fiber modes in both TE and TM polarization. By using higher order modes already in integrated waveguides and by exciting the grating from both ends the LP_{01}, $LP_{11,a}$, $LP_{11,b}$ and $LP_{21,a}$ modes of a few mode fiber in both TE and TM polarization are excitable with only a single two dimensional grating. A high coupling efficiency and low differential mode attenuation were design goals of the optimization, where again results from previous sections were used to alleviate the demanding simulations in three dimensions. The field profiles scattered by the grating were sampled and showed great similarity with the corresponding fiber modes. Integrated components such as MMIs, tapers, waveguides, etc. were investigated and adapted for operation with TE_{00} and TE_{10} modes and alternative devices for the generation of the TE_{10} mode from the fundamental waveguide were sketched.

Bibliography

[1] R. Baets, P. Dumon, W. Bogaerts, G. Roelkens, D. Taillaert, B. Luyssaert, G. Priem, G. Morthier, P. Bienstman, and D. Van Thourhout. Silicon-on-insulator based nano-photonics: Why, how, what for? In *Group IV Photonics, 2005. 2nd IEEE International Conference on*, pages 168–170, Sept 2005.

[2] H. H. Li. Refractive index of silicon and germanium and its wavelength and temperature derivatives. *Journal of Physical and Chemical Reference Data*, 9(3):561–658, 1980.

[3] Calvin D. Salzberg and John J. Villa. Infrared refractive indexes of silicon germanium and modified selenium glass. *J. Opt. Soc. Am.*, 47(3):244–246, Mar 1957.

[4] I. H. Malitson. Interspecimen comparison of the refractive index of fused silica. *J. Opt. Soc. Am.*, 55(10):1205–1208, Oct 1965.

[5] Karsten Voigt. *Interferometric devices based on 4mum SOI material for application in optical telecommunications*. PhD thesis, Technische Universität Berlin, 2012.

[6] M. Fritze, J. Knecht, C. Bozler, C. Keast, J. Fijol, S. Jacobson, P. Keating, J. LeBlanc, E. Fike, B. Kessler, M. Frish, and C. Manolatou. 3d mode converters for soi integrated optics. In *SOI Conference, IEEE International 2002*, pages 165–166, Oct 2002.

[7] Anita Sure, Thomas Dillon, Janusz Murakowski, Chunchen Lin, David Pustai, and Dennis Prather. Fabrication and characterization of three-dimensional silicon tapers. *Opt. Express*, 11(26):3555–3561, Dec 2003.

[8] Y. Shani, C. H. Henry, R. C. Kistler, K. J. Orlowsky, and D. A. Ackerman. Efficient coupling of a semiconductor laser to an optical fiber by means of a tapered waveguide on silicon. *Applied Physics Letters*, 55(23):2389–2391, 1989.

[9] Vilson R. Almeida, Roberto R. Panepucci, and Michal Lipson. Nanotaper for compact mode conversion. *Opt. Lett.*, 28(15):1302–1304, Aug 2003.

[10] T. Shoji, T. Tsuchizawa, T. Watanabe, K. Yamada, and H. Morita. Low loss mode size converter from 0.3 mu;m square si wire waveguides to singlemode fibres. *Electronics Letters*, 38(25):1669–1670, Dec 2002.

[11] Sharee McNab, Nikolaj Moll, and Yurii Vlasov. Ultra-low loss photonic integrated circuit with membrane-type photonic crystal waveguides. *Opt. Express*, 11(22):2927–2939, Nov 2003.

[12] T. Tsuchizawa, K. Yamada, Toshifumi Watanabe, H. Fukuda, H. Nishi, H. Shinojima, and Seiichi Itabashi. Spot-size converters for rib-type silicon photonic wire waveguides. In *Group IV Photonics, 2008 5th IEEE International Conference on*, pages 200–202, Sept 2008.

[13] G.Z. Masanovic, V. M N Passaro, and G.T. Reed. Dual grating-assisted directional coupling between fibers and thin semiconductor waveguides. *Photonics Technology Letters, IEEE*, 15(10):1395–1397, Oct 2003.

[14] Goran Masanovic, Graham Reed, William Headley, Branislav Timotijevic, Vittorio Passaro, Raghied Atta, Graham Ensell, and Alan Evans. A high efficiency input/output coupler for small silicon photonic devices. *Opt. Express*, 13(19):7374–7379, Sep 2005.

[15] T. Tamir and S.T. Peng. Analysis and design of grating couplers. *Applied physics*, 14(3):235–254, 1977.

[16] R.M. Emmons and Dennis G. Hall. Buried-oxide silicon-on-insulator structures. ii. waveguide grating couplers. *Quantum Electronics, IEEE Journal of*, 28(1):164–175, Jan 1992.

[17] D. Taillaert, W. Bogaerts, P. Bienstman, T.F. Krauss, P. van Daele, I. Moerman, S. Verstuyft, K. De Mesel, and R. Baets. An out-of-plane grating coupler for efficient butt-coupling between compact planar waveguides and single-mode fibers. *Quantum Electronics, IEEE Journal of*, 38(7):949–955, 7 2002.

[18] Zhe Xiao, Tsung-Yang Liow, Jing Zhang, Ping Shum, and Feng Luan. Bandwidth analysis of waveguide grating coupler. *Opt. Express*, 21(5):5688–5700, Mar 2013.

[19] Frederik Van Laere, Günther Roelkens, Melanie Ayre, Jonathan Schrauwen, Dirk Taillaert, Dries Van Thourhout, Thomas F. Krauss, and Roel Baets. Compact and highly efficient grating couplers between optical fiber and nanophotonic waveguides. *J. Lightwave Technol.*, 25(1):151–156, Jan 2007.

[20] Wissem Sfar Zaoui, Andreas Kunze, Wolfgang Vogel, Manfred Berroth, Jörg Butschke, Florian Letzkus, and Joachim Burghartz. Bridging the gap between optical fibers and silicon photonic integrated circuits. *Opt. Express*, 22(2):1277–1286, Jan 2014.

[21] Günther Roelkens, Dries Van Thourhout, and Roel Baets. High efficiency silicon-on-insulator grating coupler based on a poly-silicon overlay. *Opt. Express*, 14(24):11622–11630, 11 2006.

[22] Chao Li, Huijuan Zhang, Mingbin Yu, and G. Q. Lo. Cmos-compatible high efficiency double-etched apodized waveguide grating coupler. *Opt. Express*, 21(7):7868–7874, Apr 2013.

[23] Dirk Taillaert. *Roosterkoppelaars voor koppeling tussen optische vezels en nanofotische golfgeleiders.* PhD thesis, Ghent University, 2005.

[24] D. Taillaert, Harold Chong, P.I. Borel, L.H. Frandsen, R.M. De La Rue, and R. Baets. A compact two-dimensional grating coupler used as a polarization splitter. *Photonics Technology Letters, IEEE*, 15(9):1249–1251, 9 2003.

[25] Lee Carroll, Dario Gerace, Ilaria Cristiani, and Lucio C. Andreani. Optimizing polarization-diversity couplers for si-photonics: reaching the -1db coupling efficiency threshold. *Opt. Express*, 22(12):14769–14781, Jun 2014.

[26] F. Van Laere, T. Claes, Jonathan Schrauwen, S. Scheerlinck, W. Bogaerts, D. Taillaert, L. O'Faolain, D. Van Thourhout, and R. Baets. Compact focusing grating couplers for silicon-on-insulator integrated circuits. *Photonics Technology Letters, IEEE*, 19(23):1919–1921, Dec 2007.

[27] Christopher R. Doerr, Nicolas Fontaine, Masaaki Hirano, Takashi Sasaki, Larry Buhl, and Peter Winzer. Silicon photonic integrated circuit for coupling to a ring-core multimode fiber for space-division multiplexing. In *37th European Conference and Exposition on Optical Communications*, page Th.13.A.3. Optical Society of America, 2011.

[28] Nicolas K. Fontaine, Christopher R. Doerr, Miguel A. Mestre, Roland Ryf, Peter Winzer, Larry Buhl, Yi Sun, Xinli Jiang, and Robert Lingle. Space-division multiplexing and all-optical mimo demultiplexing using a photonic integrated circuit. In *Optical Fiber Communication Conference*, page PDP5B.1. Optical Society of America, 2012.

[29] A.M.J. Koonen, Haoshuo Chen, H. P A Van den Boom, and O. Raz. Silicon photonic integrated mode multiplexer and demultiplexer. *Photonics Technology Letters, IEEE*, 24(21):1961–1964, 11 2012.

[30] Yunhong Ding, Haiyan Ou, Jing Xu, and C. Peucheret. Silicon photonic integrated circuit mode multiplexer. *Photonics Technology Letters, IEEE*, 25(7):648–651, 4 2013.

[31] W.S. Zaoui, A Kunze, W. Vogel, and M. Berroth. Cmos-compatible polarization splitting grating couplers with a backside metal mirror. *Photonics Technology Letters, IEEE*, 25(14):1395–1397, July 2013.

[32] Max Born and Emil Wolf. *Principles of Optics: Electromagnetic Theory of Propagation, Interference and Diffraction of Light*. Cambridge University Press, 1999.

[33] Günter Schmahl and Dietbert Rudolph. Holographic diffraction gratings. *Sterne und Weltraum*, 15:86–91, 1976.

[34] Christopher R Doerr, Long Chen, Young-Kai Chen, and Larry L Buhl. Wide bandwidth silicon nitride grating coupler. *IEEE Photonics Technology Letters*, 22(19):1461–1463, 2010.

[35] Allen Taflove and Susan C Hagness. *Computational Electrodynamics, the Finite-Difference Time-Domain Method*, volume 160. Artech house Boston, 2000.

[36] Joseph B. Keller. Geometrical theory of diffraction. *J. Opt. Soc. Am.*, 52(2):116–130, 1962.

[37] R.G. Kouyoumjian and P.H. Pathak. A uniform geometrical theory of diffraction for an edge in a perfectly conducting surface. *Proceedings of the IEEE*, 62(11):1448–1461, 11 1974.

[38] Roger F Harrington and Jan L Harrington. *Field computation by moment methods*. Oxford University Press, 1996.

[39] Korada R. Umashankar. Numerical analysis of electromagnetic wave scattering and interaction based on frequency-domain integral equation and method of moments techniques. *Wave Motion*, 10(6):493 – 525, 1988. Special Issue on Numerical Methods for Electromagnetic Wave Interactions.

[40] Kane Yee. Numerical solution of initial boundary value problems involving maxwell's equations in isotropic media. *Antennas and Propagation, IEEE Transactions on*, 14(3):302–307, 5 1966.

[41] Allen Taflove and M.E. Brodwin. Numerical solution of steady-state electromagnetic scattering problems using the time-dependent maxwell's equations. *Microwave Theory and Techniques, IEEE Transactions on*, 23(8):623–630, 8 1975.

[42] Ardavan F. Oskooi, David Roundy, Mihai Ibanescu, Peter Bermel, J. D. Joannopoulos, and Steven G. Johnson. MEEP: A flexible free-software package for electromagnetic simulations by the FDTD method. *Computer Physics Communications*, 181:687–702, 1 2010.

[43] J.J. Simpson and Allen Taflove. Three-dimensional fdtd modeling of impulsive elf propagation about the earth-sphere. *Antennas and Propagation, IEEE Transactions on*, 52(2):443–451, 2 2004.

[44] A. Taflove. *Computational Electrodynamics: The Finite - Difference Time - Domain Method*. Antennas and Propagation Library. Artech House, Incorporated, 1995.

[45] J.D. Joannopoulos, S.G. Johnson, J.N. Winn, and R.D. Meade. *Photonic Crystals: Molding the Flow of Light (Second Edition)*. Princeton University Press, 2011.

[46] K.A. Zaki, S.-W. Chen, and C. Chen. Modeling discontinuities in dielectric-loaded waveguides. *Microwave Theory and Techniques, IEEE Transactions on*, 36(12):1804–1810, 12 1988.

[47] G.V. Eleftheriades, A.S. Omar, L.P.B. Katehi, and G.M. Rebeiz. Some important properties of waveguide junction generalized scattering matrices in the context of the mode matching technique. *Microwave Theory and Techniques, IEEE Transactions on*, 42(10):1896–1903, 10 1994.

[48] Dominic Gallagher. Photonic cad matures. *IEEE LEOS Newletter*, pages 1–14, 2 2008.

[49] Dominic F. G. Gallagher and Thomas P. Felici. Eigenmode expansion methods for simulation of optical propagation in photonics: pros and cons. In *Proceedings SPIE*, volume 4987, pages 69–82, 2003.

[50] R. W. Clough. Early history of the finite element method from the view point of a pioneer. *International Journal for Numerical Methods in Engineering*, 60(1):283–287, 2004.

[51] P Silvester. Finite element solution of homogeneous waveguide problems. *Alta Frequenza*, 38:313–317, 1969.

[52] S. Ahmed and P. Daly. Waveguide solutions by the finite-element method. *Radio and Electronic Engineer*, 38:217–223(6), 10 1969.

[53] Fajie Li and Reinhard Klette. *Euclidean Shortest Paths*. Springer, 2011.

[54] Jim Ruppert. A delaunay refinement algorithm for quality 2-dimensional mesh generation. *Journal of Algorithms*, 18(3):548 – 585, 1995.

[55] L. Paul Chew. Guaranteed-quality mesh generation for curved surfaces. In *Proceedings of the Ninth Annual Symposium on Computational Geometry*, SCG '93, pages 274–280. ACM, 1993.

[56] James Hardy Wilkinson, James Hardy Wilkinson, and James Hardy Wilkinson. *The algebraic eigenvalue problem*, volume 87. Oxford Univ Press, 1965.

[57] Lloyd N Trefethen and David Bau III. *Numerical linear algebra*, volume 50. Siam, 1997.

[58] Edward Anderson, Zhaojun Bai, Christian Bischof, Susan Blackford, James Demmel, Jack Dongarra, Jeremy Du Croz, Anne Greenbaum, S Hammerling, Alan McKenney, et al. *LAPACK Users' guide*, volume 9. Siam, 1999.

[59] Jiamming Jin. *The finite element method in electromagnetics*. Wiley New York, 2002.

[60] Jan Pomplun, Sven Burger, Lin Zschiedrich, and Frank Schmidt. Adaptive finite element method for simulation of optical nano structures. *physica status solidi (b)*, 244(10):3419–3434, 2007.

[61] Jean-Pierre Berenger. A perfectly matched layer for the absorption of electromagnetic waves. *Journal of Computational Physics*, 114(2):185 – 200, 1994.

[62] Z.S. Sacks, D.M. Kingsland, R. Lee, and Jin-Fa Lee. A perfectly matched anisotropic absorber for use as an absorbing boundary condition. *Antennas and Propagation, IEEE Transactions on*, 43(12):1460–1463, 12 1995.

[63] Weng Cho Chew and William H. Weedon. A 3d perfectly matched medium from modified maxwell's equations with stretched coordinates. *Microwave and Optical Technology Letters*, 7(13):599–604, 1994.

[64] Ardavan F. Oskooi, Lei Zhang, Yehuda Avniel, and Steven G. Johnson. The failure of perfectly matched layers, and towards their redemptionby adiabatic absorbers. *Opt. Express*, 16(15):11376–11392, 7 2008.

[65] Steven G. Johnson. Notes on the UPML implementation in meep. `http://ab-initio.mit.edu/meep/pml-meep.pdf`. Accessed: 1. October 2014.

[66] M. D. Feit and J. A. Fleck. Light propagation in graded-index optical fibers. *Appl. Opt.*, 17(24):3990–3998, 12 1978.

[67] M. G. Moharam, T. K. Gaylord, Eric B. Grann, and Drew A. Pommet. Formulation for stable and efficient implementation of the rigorous coupled-wave analysis of binary gratings. *J. Opt. Soc. Am. A*, 12(5):1068–1076, 5 1995.

[68] M. G. Moharam, T. K. Gaylord, Drew A. Pommet, and Eric B. Grann. Stable implementation of the rigorous coupled-wave analysis for surface-relief gratings: enhanced transmittance matrix approach. *J. Opt. Soc. Am. A*, 12(5):1077–1086, 5 1995.

[69] J Willard Gibbs. Fourier's series. *Nature*, 59:200, 1898.

[70] John David Jackson and John D Jackson. *Classical electrodynamics*, volume 3. Wiley New York etc., 1962.

[71] Constantine A Balanis. *Advanced Engineering Electromagnetics*, volume 20. Wiley New York, 1989.

[72] Corning SMF-28e+ optical fiber data sheet. `http://www.corning.com/WorkArea/showcontent.aspx?id=63939`. Accessed: 1. October 2014.

[73] Dieter Knoll, Stefan Lischke, Lars Zimmermann, Bernd Heinemann, Daniel Micusik, Pylyp Ostrovskyy, Georg Winzer, Marcel Kroh, Rainer Barth, Thomas Grabolla, Katrin Schulz, Mirko Fraschke, Marco Lisker, Jürgen Drews, Andreas Trusch, Andreas Krüger, Steffen Marschmeyer, Harald Richter, Oksana Fursenko, Yuji Yamamoto, Benjamin Wohlfeil, Klaus Petermann, Andreas Beling, and Bernd Tillack. Monolithically integrated 25gbit/sec receiver for 1.55μm in photonic bicmos technology. In *Optical Fiber Communication Conference*, page Th4C.4. Optical Society of America, 2014.

[74] D. Arsenijević, M. Kleinert, and D. Bimberg. Phase noise and jitter reduction by optical feedback on passively mode-locked quantum-dot lasers. *Applied Physics Letters*, 103(23), 2013.

[75] G. Roelkens, D. Vermeulen, S. Selvaraja, R. Halir, W. Bogaerts, and D. Van Thourhout. Grating-based optical fiber interfaces for silicon-on-insulator photonic integrated circuits. *Selected Topics in Quantum Electronics, IEEE Journal of*, 17(3):571–580, 5 2011.

[76] Christian Blum and Andrea Roli. Metaheuristics in combinatorial optimization: Overview and conceptual comparison. *ACM Computing Surveys (CSUR)*, 35(3):268–308, 2003.

[77] Leonora Bianchi, Marco Dorigo, Luca Maria Gambardella, and Walter J Gutjahr. A survey on metaheuristics for stochastic combinatorial optimization. *Natural Computing: an international journal*, 8(2):239–287, 2009.

[78] David H Wolpert and William G Macready. No free lunch theorems for optimization. *Evolutionary Computation, IEEE Transactions on*, 1(1):67–82, 1997.

[79] David H Wolpert and William G Macready. No free lunch theorems for search. Technical report, Technical Report SFI-TR-95-02-010, Santa Fe Institute, 1995.

[80] Alex Fraser, Donald Burnell, et al. *Computer models in genetics*. New York and London: McGraw-Hill Book Company, 1970.

[81] Jack L Crosby et al. *Computer simulation in genetics*. John Wiley & Sons Ltd, 1973.

[82] James Kennedy, Russell Eberhart, et al. Particle swarm optimization. In *Proceedings of IEEE international conference on neural networks*, volume 4, pages 1942–1948. Perth, Australia, 1995.

[83] Ender Ozcan and Chilukuri K Mohan. Particle swarm optimization: surfing the waves. In *Evolutionary Computation, 1999. CEC 99. Proceedings of the 1999 Congress on*, volume 3. IEEE, 1999.

[84] M. Clerc and J. Kennedy. The particle swarm - explosion, stability, and convergence in a multidimensional complex space. *Evolutionary Computation, IEEE Transactions on*, 6(1):58–73, 2 2002.

[85] R.C. Eberhart and Y. Shi. Comparing inertia weights and constriction factors in particle swarm optimization. In *Evolutionary Computation, 2000. Proceedings of the 2000 Congress on*, volume 1, pages 84–88 vol.1, 2000.

[86] Xia Chen, Chao Li, C.K.Y. Fung, S.M.G. Lo, and H.K. Tsang. Apodized waveguide grating couplers for efficient coupling to optical fibers. *Photonics Technology Letters, IEEE*, 22(15):1156–1158, 8 2010.

[87] Xia Chen, Chao Li, and Hon-Ki Tsang. Fabrication-tolerant waveguide chirped grating coupler for coupling to a perfectly vertical optical fiber. *Photonics Technology Letters, IEEE*, 20(23):1914–1916, 12 2008.

[88] Daoxin Dai and John E. Bowers. Novel concept for ultracompact polarization splitter-rotator based on silicon nanowires. *Opt. Express*, 19(11):10940–10949, 5 2011.

[89] Furukawa Electric Co. Ltd. Few mode fibers. `http://fiber-optic-catalog.ofsoptics.com/item/few-mode-optical-fiber-series/few-mode-optical-fiber-series1/two-mode-graded-index`. Accessed: 1. October 2014.

[90] Juerg Leuthold, Juerg Eckner, Emil Gamper, Pierre A. Besse, and Hans Melchior. Multimode interference couplers for the conversion and combining of zero- and first-order modes. *J. Lightwave Technol.*, 16(7):1228, 7 1998.

[91] L.B. Soldano and E. C M Pennings. Optical multi-mode interference devices based on self-imaging: principles and applications. *Lightwave Technology, Journal of*, 13(4):615–627, 4 1995.

[92] K. Voigt, L. Zimmermann, G. Winzer, and K. Petermann. Soi based 2x2 and 4x4 waveguide couplers - evolution from dpsk to dqpsk. In *Group IV Photonics, 2008 5th IEEE International Conference on*, pages 209–211, 9 2008.

[93] Ang Li. Photonic integrated coupler for multimode operation. Master's thesis, Technische Universität Berlin, 2013.

[94] Richard A. Soref and B.R. Bennett. Electrooptical effects in silicon. *Quantum Electronics, IEEE Journal of*, 23(1):123–129, 1 1987.

[95] Bradley J. Frey, Douglas B. Leviton, and Timothy J. Madison. Temperature-dependent refractive index of silicon and germanium. In *Proc. SPIE*, volume 6273, pages 62732J–62732J–10, 2006.

[96] J. Komma, C. Schwarz, G. Hofmann, D. Heinert, and R. Nawrodt. Thermo-optic coefficient of silicon at 1550nm and cryogenic temperatures. *Applied Physics Letters*, 101(4), 2012.

[97] S. Martínez-Garaot, Shuo-Yen Tseng, and J. G. Muga. Compact and high conversion efficiency mode-sorting asymmetric y junction using shortcuts to adiabaticity. *Opt. Lett.*, 39(8):2306–2309, 4 2014.

[98] Raoul Fofe. Integriert optische strukturen in silizium zur wandlung von modenfeldern. Master's thesis, Technische Universität Berlin, 2013.

List of Publications

- S. Warm, A. Juarez, B. Wohlfeil and K. Petermann. Cross-talk in modedivision-multiplex optical fiber transmission systems. 13th International Conference on Transparent Optical Networks (ICTON), June 2011

- B. Wohlfeil, L. Zimmermann and K. Petermann. Asymmetric codirectional coupler between regular nanowaveguide and slot-waveguide for polarization conversion. In Advanced Photonics Congress, page ITu2B.5. Optical Society of America, 2012.

- B. Wohlfeil, C. Stamatiadis, L. Zimmermann and K. Petermann. Compact Fiber Grating Coupler on SOI for Coupling of Higher Order Fiber Modes. Optical Fiber Communication Conference, page OTh1B.2. Optical Society of America, 2013.

- D. Knoll, S. Lischke, L. Zimmermann, B. Heinemann, D. Micusik, P. Ostrovskyy, G. Winzer, M. Kroh, R. Barth, T. Grabolla, K. Schulz, M. Fraschke, M. Lisker, J. Drews, A. Trusch, A. Krüger, S. Marschmeyer, H. Richter, O. Fursenko, Y. Yamamoto, B. Wohlfeil, K. Petermann, A. Beling and B. Tillack. Monolithically Integrated 25GBit/sec Receiver for 1.55μm in Photonic BiCMOS Technology. Optical Fiber Communication Conference, page Th4C.4. Optical Society of America, 2014.

- S. Lischke, B. Wohlfeil, D. Knoll, L. Zimmermann, C. Mai, Y. Yamamoto, S. Marschmeyer, K. Voigt and B. Tillack. High-efficiency Grating Couplers for Integration into a High-performance Photonic BiCMOS Process. Asia Communications and Photonics Conference, pages AW4A-1. Optical Society of America, 2013.

- B. Wohlfeil, S. Burger, C. Stamatiadis, J. Pomplun, F. Schmidt, L. Zimmermann and K. Petermann. Numerical Simulation of Grating Couplers for Mode Multiplexed Systems. SPIE OPTO, pp. 89880K-89880K. International Society for Optics and Photonics, 2014.

- B. Wohlfeil, L. Zimmermann and K. Petermann. Optimization of Fiber Grating Couplers on SOI using Advanced Search Algorithms. Opt. Lett. 39, pages 3201-3203, 2014.

- B. Wohlfeil, C. Stamatiadis, M. Jäger, L. Zimmermann S. Burger and K. Petermann. Integrated Optical Fiber Grating Coupler on SOI for the Excitation of Several Higher Order Fiber Modes. Accepted at 40th European Conference and Exposition on Optical Communications (ECOC), page We.1.1.2, 2014

- B. Wohlfeil, S. Burger, F. Schmidt, L. Zimmermann and K. Petermann. Fiber Grating Coupler on SOI for the Excitation of LP_{01}, $LP_{11,a}$, $LP_{11,b}$ and $LP_{21,a}$ Fiber Modes. Accepted at EOSAM 2014

List of Figures

List of Acronyms

BiCMOS	Bipolar CMOS
BOX	Buried Oxide
BPM	Beam Propagation Method
CMOS	Complementary Metal-Oxide-Semiconductor
DGADC	Dual Grating Assisted Directional Coupler
DUV	Deep Ultraviolet
EME	Eigenmode Expansion
FDTD	Finite-Difference Time-Domain
FEM	Finite Element Method
FM	Few Mode
GA	Genetic Algorithm
GaAs	Gallium Arsenide
InP	Indium Phosphide
LP	Linearly Polarized
MMI	Multimode Interference (coupler)
MZI	Mach–Zehnder Interferometer
OPC	Optical Proximity Correction
PIC	Photonic Integrated Circuit
PML	Perfectly Matched Layer
PSA	Particle Swarm Algorithm
RCWA	Rigorous Coupled-Wave Analysis
RIE	Reactive-Ion Etching
Si_3N_4	Silicon Nitride
SiO_2	Silicon Dioxide
SiON	Silicon Oxynitride
(s)SMF	(standard) Single Mode Fiber
SOI	Silicon on Insulator
TE	Transverse Electric
TM	Transverse Magnetic

List of Symbols

α	Shearing angle
β	Phase constant
η	Overlap integral
λ	Vacuum wavelength
Λ	Grating period
ρ	Figure of merit in few mode gratings
ϕ	Scalar field potential
φ	Fiber tilt angle
φ_1	Fiber tilt angle in xz-plane
φ_2	Fiber tilt angle in yz-plane
$\Delta\phi$	Relative phase shift
d	Vertical distance fiber-chip
d_c	Duty cycle
d_x	Waveguide distance in MMIs
$\vec{E}$	Electric field strength
$f(\varphi)$	Angular window function for PSA optimization
$\vec{H}$	Magnetic field strength
h_{box}	Buried oxide layer height
h_{cl}	Cladding layer height
h_e	Grating etch depth
h_{epi}	Epitaxial layer height
h_{pre}	Preliminary etch depth
h_{sub}	Substrate thickness
h_{wg}	Waveguide height
$\vec{k}$	Wave vector
L_{epi}	Extension length of epitaxial layer
L_{MMI}	MMI length
L_T	Taper length
L_{wg}	Waveguide length
$\vec{n}$	Surface normal vector
n	Refractive index
n_{eff}	Effective refractive index
P_{coupl}	Overall coupled power
P_{out}	Out-coupled power
P_{refl}	Reflected power
P_{trans}	Transmitted power
P_{wg}	Power contained in guided waveguide mode

P_{loss}	Power radiated from guided waveguide mode
U	Heater voltage
$\vec{V}$	Particle velocity
w_0	e^{-1} spot size radius
w_1	Base width of inverted taper
w_2	Tip width of inverted taper
w_{MMI}	MMI width
w_g	Grating groove width
w_r	Grating ridge width
$w_{p,g}$	Preliminary grating groove width
$w_{p,r}$	Preliminary grating ridge width
w_{wg}	Waveguide width

Danksagung

An dieser Stelle möchte ich mich bei all denjenigen bedanken, die mich beim Erstellen dieser Arbeit unterstützt haben.

Zuerst gilt mein Dank Prof. Dr.-Ing. Klaus Petermann, der mir ermöglicht hat, am Institut für Hochfrequenz- und Halbleiter-Systemtechnologien zu promovieren und immer zur Diskussion von Fragen zur Verfügung stand.

Des Weiteren bedanke ich mich bei den Professoren Berroth und Schuhmann, die sich als Gutachter für diese Arbeit zur Verfügung gestellt haben.

Dr. Lars Zimmermann sei gedankt für seine hilfreiche Unterstützung und die Organisation des Joint Labs zwischen der TU Berlin und der IHP Microelectronics GmbH, das die Realisierung der gezeigten Strukturen erst möglich gemacht hat. Ebenso bedanke ich mich bei den Herren Andrzej Gajda und Georg Winzer, die als Kontaktpersonen am IHP immer zur Verfügung standen und bei der Klärung von Detailfragen sehr hilfreich gewesen sind. Auch möchte ich Dr. Karsten Voigt für seine Unterstützung und die Betreuung des Messlabors danken. Auch den anderen Kollegen gilt meine Anerkennung, da sie immer für Ideen offen waren und eine hervorragende Arbeitsatmosphäre geschaffen haben.

Außerdem möchte ich mich bei Dr. Sven Burger und Prof. Dr. Frank Schmidt vom Zuse Institut Berlin für das zur Verfügung Stellen der genutzen Simulationssoftware bedanken.

Nicht zuletzt sei auch Shulin Li recht herzlich für ihre tatkräftige Unterstützung vorallem im Bereich des Korrekturlesens gedankt.